

Winter 2010

Hyperpolarized Xenon-129 Magnetic Resonance Imaging of Functional Lung Microstructure

Isabel Dregely

University of New Hampshire, Durham

Follow this and additional works at: <https://scholars.unh.edu/dissertation>

Recommended Citation

Dregely, Isabel, "Hyperpolarized Xenon-129 Magnetic Resonance Imaging of Functional Lung Microstructure" (2010). *Doctoral Dissertations*. 549.

<https://scholars.unh.edu/dissertation/549>

This Dissertation is brought to you for free and open access by the Student Scholarship at University of New Hampshire Scholars' Repository. It has been accepted for inclusion in Doctoral Dissertations by an authorized administrator of University of New Hampshire Scholars' Repository. For more information, please contact nicole.hentz@unh.edu.

HYPERPOLARIZED ^{129}Xe MAGNETIC RESONANCE IMAGING OF
FUNCTIONAL LUNG MICROSTRUCTURE

BY

Isabel Dregely

M.S., University of New Hampshire, Durham, USA, 2010

DISSERTATION

Submitted to the University of New Hampshire
in partial fulfillment of
the requirements for the degree of

Doctor of Philosophy

in

Physics

December 2010

UMI Number: 3442544

All rights reserved

INFORMATION TO ALL USERS

The quality of this reproduction is dependent upon the quality of the copy submitted.

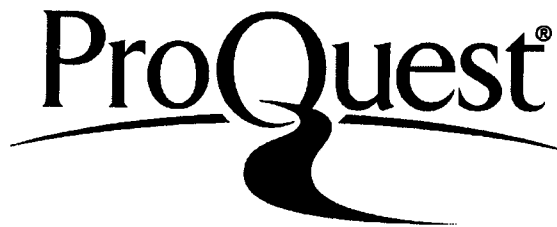
In the unlikely event that the author did not send a complete manuscript and there are missing pages, these will be noted. Also, if material had to be removed, a note will indicate the deletion.



UMI 3442544

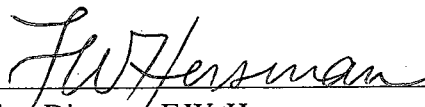
Copyright 2011 by ProQuest LLC.

All rights reserved. This edition of the work is protected against unauthorized copying under Title 17, United States Code.

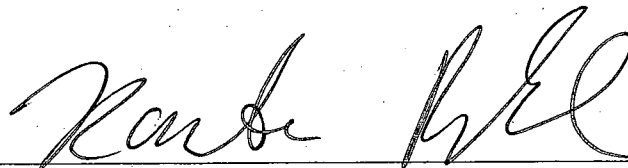


ProQuest LLC
789 East Eisenhower Parkway
P.O. Box 1346
Ann Arbor, MI 48106-1346

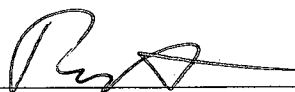
This dissertation has been examined and approved.



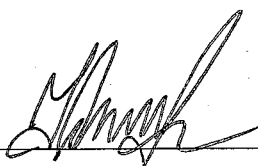
Dissertation Director, F.W. Hersman
Professor of Physics
University of New Hampshire, Durham, NH, USA,



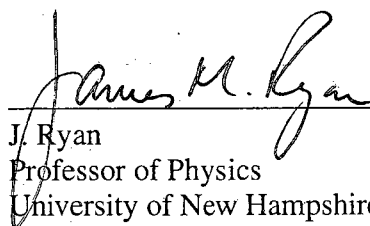
K. Pohl
Associate Professor of Physics
University of New Hampshire, Durham, NH, USA



K. Ruppert
Assistant Professor of Radiology
University of Virginia, Charlottesville, VA, USA



I.C. Ruset
Affiliate Assistant Professor of Physics
University of New Hampshire, Durham, NH, USA



J. Ryan
Professor of Physics
University of New Hampshire, Durham, NH, USA

Nov 19 2010
Date

DEDICATION

To my parents.

ACKNOWLEDGMENTS

This work would not have been possible without the contribution from numerous inspiring people, who were colleagues and friends. First and foremost, I would like to thank my advisor Dr. Bill Hersman for his excellent guidance and support throughout this project. The uncomplicated but inspiring environment he was able to create for me to conduct my research was greatly appreciated.

I especially thank Dr. Iulian Ruset, who was my mentor from the very beginning at UNH and provided invaluable help throughout the whole project. Iulian always surprised me by his creativity through which he found a solution to simply everything. At Xemed headquarters, John Brackett designed and manufactured the mechanical frame of the chest coil. Dr. Iulian Ruset, Steve Ketel, Jeff Ketel, Dr. Jan Distelbrink and Dr. Dave Watt built and ran the polarizer.

At Massachusetts General Hospital (MGH) in Boston, I would like to thank Dr. Larry Wald for his tremendous support by providing infrastructure, scientific advice and fun group dinners. In the coil lab, Dr. Graham Wiggins with great patience taught me all the basics about the "black magic" of RF coil making. A special thanks to Azma Mareyam for teaching me all about coils, being a great friend and for making sure there always was some action in the lab. Thanks also to Dr. Vijay Alagappan for his patience teaching me about coils. I thank Dr. Jonathan Polimeni for sharing code and his impressive knowledge about image reconstructions. Kyoko Fujimoto, Dr. Khaldoun Makhoul and Dr. Boris Keil also were great friends at MGH.

At the University of Virginia (UVA) I especially thank Dr. Kai Ruppert for his excellent support and scientific guidance throughout the imaging experiments. I would like to thank the whole UVA team, Dr. Kai Ruppert, Dr. Tally Altes, Dr. John Mugler III, Dr. Jamie Mata and Dr. Wilson Miller for the support, scientific discussions and good times I had at UVA.

Dr. Sam Patz provided valuable guidance while acquiring initial results at the Brigham and Women's Hospital, Boston and also later at MGH. I especially thank Dr. Mirko Hrovat, who generously shared his extensive experience in MR physics and engineering principles of RF coils. Dr. Iga Muradian guided my first steps in hyperpolarized MRI with inspiring enthusiasm and also together with Dr. Mike Dabaghyan were the best roommates ever.

Last but not least, I would like to thank my wonderful parents and brother Daniel for their unconditional love and monumental support. Mama, Papa, Daniel, without you I would not be here. E Fernando, você é meu melhor amigo, meu parceiro de discussão, viagens, dança e esportes, meu favorito cozinheiro, o homen que eu sonhei. Seu amor me faz feliz.

This work was financially supported by the National Institutes of Health under grants R42 HL082013, R01 HL079077 and by the New Hampshire Innovation Research Center. My first year at UNH was supported by a Fulbright Fellowship.

CONTENTS

DEDICATION	iii
ACKNOWLEDGMENTS	iv
LIST OF TABLES	x
LIST OF FIGURES	xi
ABSTRACT	xiv
1 INTRODUCTION	1
1.1 Motivation	1
1.2 Problem Definition	3
1.3 Objectives	4
1.4 Organization	5
2 BACKGROUND	8
2.1 The Lung	8
2.1.1 Structure	8
2.1.2 Gas Exchange	11
2.1.3 Pulmonary Function Tests	11
2.1.4 Obstructive and Restrictive Lung Disease	12
2.1.5 Lung Imaging	14
2.2 Concepts in Magnetic Resonance Imaging	16
2.2.1 Spins and Magnetization	16
2.2.2 Signal and Noise	18
2.2.3 Relaxation	20

2.2.4	Bloch Equations	22
2.2.5	Image Formation	23
2.3	Hyperpolarized Gas MRI	27
2.3.1	Characteristics of Hyperpolarized Noble Gases ^3He and ^{129}Xe	29
2.3.2	Imaging Protocols	31
2.4	Parallel Imaging	36
2.4.1	Phased-Array Coils	37
2.4.2	Parallel Image Reconstruction Algorithms	38
2.4.3	SNR in Parallel Imaging	42
2.4.4	Parallel Imaging for Hyperpolarized Gas MRI	42
3	PHASED-ARRAY XENON CHEST COIL	44
3.1	Introduction	44
3.2	Background	45
3.2.1	Why Tuning?	45
3.2.2	Why Matching?	47
3.2.3	Array Design	48
3.2.4	Transmit Coil	50
3.3	Methods	57
3.3.1	32-Channel Phased-Array Receive Coil	57
3.3.2	Integrated Asymmetric Birdcage Transmit Coil	61
3.4	Results	65
3.4.1	Receive Array	65
3.4.2	Transmit Asymmetric Birdcage	68
3.4.3	Spin Density Imaging in Healthy Subjects and Subjects with Lung Disease	72
3.5	Discussion and Conclusions	72

4	HYPERPOLARIZED ^{129}Xe GAS-EXCHANGE IMAGING OF LUNG MICROSTRUCTURE	79
4.1	Introduction	79
4.2	Background	82
4.3	Materials and Methods	85
4.3.1	General Study Protocol	85
4.3.2	Hyperpolarized-Gas Production	87
4.3.3	Imaging Protocols	87
4.3.4	Data Analysis	90
4.3.5	Statistical Analysis	91
4.4	Results	92
4.4.1	Estimation of Absolute Lung Volume	92
4.4.2	Curve Fitting Quality	93
4.4.3	Microstructure Parameter Maps in Healthy Lung Physiology	94
4.4.4	Parameter Dependence on Lung Height and Ventilation Volume in Healthy Lung Physiology	95
4.4.5	Results in Subjects with Lung Disease Compared to Healthy Subjects	100
4.5	Discussion	105
4.5.1	Absolute Lung Volumes	108
4.5.2	Parameter Uncertainty	109
4.5.3	Functional Microstructure in Healthy Subjects and Rabbits	109
4.5.4	Functional Microstructure in Subjects with Obstructive Lung Disease	114
4.5.5	Conclusions	118
5	CONCLUSIONS	120
	APPENDICES	123

APPENDIX A	DIFFUSION EQUATION OF HEAT CONDUCTION TYPE WITH DIRICHLET BOUND- ARY CONDITIONS	124
APPENDIX B	FREQUENTLY USED ABBREVIATIONS	126
APPENDIX C	IRB HUMAN PROTOCOL APPROVAL	127
BIBLIOGRAPHY		129

LIST OF TABLES

2.1	Morphometric data for healthy adult lung.	10
2.2	COPD GOLD stage classification.	14
2.3	Representative relaxation times T_1 and T_2 for hydrogen components of different human body tissues.	22
2.4	Properties of hyperpolarized gases ^3He and ^{129}Xe	31
3.1	Comparison of Q-factors for different surface coil designs.	58
4.1	MXTC - human subject information.	87
4.2	Absolute lung volume estimation for MXTC studies.	92
4.3	MXTC results for healthy subjects and rabbits at two different ventilation volumes.	98
4.4	MXTC, ADC, DP and CT results for healthy subjects and subjects with lung disease.	104

LIST OF FIGURES

2-1	Resin cast of human lung and fractal tree of Mandelbrot.	9
2-2	Scanning electron micrograph of human lung parenchyma and septa.	10
2-3	Spirometry.	12
2-4	Relaxation mechanisms.	21
2-5	Pulse sequence schematic.	23
2-6	Pulse sequence examples.	26
2-7	HXe spin density 3D volume acquisition.	32
2-8	ADC diffusion imaging in a healthy subject and a subject with COPD.	33
2-9	Dynamic spectroscopy of HXe spectra in the lung.	35
2-10	Direct dissolved phase imaging of a pulmonary nodule.	35
2-11	Localized sensitivity profiles of receiver channels in an array coil.	39
3-1	RF coil as a noise filter.	46
3-2	Surface coil equivalent circuit.	47
3-3	Impedance frequency dependence of a parallel resonant circuit, near resonance.	48
3-4	Frequency split caused by two resonant circuits.	49
3-5	Resolved frequency split by critical overlap of neighboring coils.	50
3-6	High- and Low-Pass birdcage design.	52
3-7	Schematic of the asymmetric birdcage coil.	53
3-8	Transmit field simulation for the asymmetric birdcage.	54

3-9	Schematic of the asymmetric birdcage coil connected to the quadrature hybrid.	56
3-10	32-channel phased-array.	57
3-11	Comparison of surface coil designs.	58
3-12	A schematic showing the preamplifier board design.	62
3-13	Cable trap schematic.	62
3-14	Drawings of the asymmetric birdcage.	63
3-15	Tuning setup for coil tuning	64
3-16	Quadrature hybrid.	65
3-17	The finished chest coil with volunteer at the MRI scanner.	66
3-18	Example of preamplifier decoupling measured using the decoupled probe and an S21 measurement.	66
3-19	Noise correlation coefficient matrix.	68
3-20	Images reconstructed in uncombined receiver channels.	69
3-21	Root-sum-of-squares compared to adaptive-combine image reconstruction.	70
3-22	B_1 map for the birdcage transmit coil and for comparison two other T/R coils.	71
3-23	Ventilation scan from healthy volunteer.	73
3-24	Ventilation scan from asthmatic patient.	73
3-25	Ventilation scan from COPD patient.	74
3-26	TrueFISP 3D spin density acquisition fully sampled and accelerated.	74
3-27	Spiral acquisition of asthmatic subject with simulated parallel reconstruction.	75
4-1	^{129}Xe dissolved in tissue.	81
4-2	Schematic of MXTC data analysis workflow.	82
4-3	Absolute lung volume estimation for MXTC studies.	93
4-4	Representative MXTC voxel fits.	94

4-5	Maps of fitting quality of MXTC data.	94
4-6	MXTC parameter maps for a healthy human subject at two different lung volumes.	96
4-7	MXTC parameter maps for a rabbit ventilated to two different lung volumes.	96
4-8	XTC depolarization map for healthy subject in the supine and prone position.	97
4-9	AP parameter dependence for healthy subjects at two different lung volumes.	99
4-10	AP parameter dependence for rabbits at two different lung volumes.	99
4-11	HXe spin density images showing regional ventilation in subjects C1 and C2.	100
4-12	MXTC parameter maps for subjects with lung disease compared to a healthy subject.	102
4-13	Dependence of MXTC parameters on lung height for subjects with lung disease.	103
4-14	Dependence of dissolved-phase ratio parameter on lung height.	105
4-15	CT data analysis for COPD subject C2	105
4-16	Results from CT and HXe imaging methods for COPD subject C2.	106
4-17	Regional correlation between HXe imaging techniques and CT.	107
4-18	Comparison of parameter distributions in emphysematous and healthy ROIs for the imaging methods.	108
4-19	Schematic of gravity induced tissue compression.	109
4-20	Micrograph of rabbit lung at TLC and 40% TLC lung inflation.	111
4-21	Classification of stereology levels.	112
4-22	Increased interstitial wall thickness with degree of emphysema.	115
A-1	Boundary conditions for HXe diffusion equation.	124

ABSTRACT

HYPERPOLARIZED ^{129}Xe MAGNETIC RESONANCE IMAGING OF FUNCTIONAL LUNG MICROSTRUCTURE

by

Isabel Dregely

University of New Hampshire, December, 2010

Hyperpolarized ^{129}Xe (HXe) is a non-invasive contrast agent for lung magnetic resonance imaging (MRI), which upon inhalation follows the functional pathway of oxygen in the lung by dissolving into lung tissue structures and entering the blood stream. HXe MRI therefore provides unique opportunities for functional lung imaging of gas exchange which occurs from alveolar air spaces across the air-blood boundary into parenchymal tissue. However challenges in acquisition speed and signal-to-noise ratio have limited the development of a HXe imaging biomarker to diagnose lung disease.

This thesis addresses these challenges by introducing parallel imaging to HXe MRI. Parallel imaging requires dedicated hardware. This work describes design, implementation, and characterization of a 32-channel phased-array chest receive coil with an integrated asymmetric birdcage transmit coil tuned to the HXe resonance on a 3 Tesla MRI system.

Using the newly developed human chest coil, a functional HXe imaging method, multiple exchange time xenon magnetization transfer contrast (MXTC) is implemented. MXTC dynamically encodes HXe gas exchange into the image contrast. This permits two parameters to be derived regionally which are related to gas-exchange functionality by characterizing tissue-to-alveolar-volume ratio and alveolar wall thickness in the lung parenchyma. Initial results in healthy subjects demonstrate the sensitivity of MXTC by quantifying the subtle changes in lung microstructure in response

to orientation and lung inflation. Our results in subjects with lung disease show that the MXTC-derived functional tissue density parameter exhibits excellent agreement with established imaging techniques. The newly developed dynamic parameter, which characterizes the alveolar wall, was elevated in subjects with lung disease, most likely indicating parenchymal inflammation. In light of these observations we believe that MXTC has potential as a biomarker for the regional quantification of 1) emphysematous tissue destruction in chronic obstructive pulmonary disease (using the tissue density parameter) and 2) parenchymal inflammation or thickening (using the wall thickness parameter). By simultaneously quantifying two lung function parameters, MXTC provides a more comprehensive picture of lung microstructure than existing lung imaging techniques and could become an important non-invasive and quantitative tool to characterize pulmonary disease.

CHAPTER 1

INTRODUCTION

1.1 Motivation

Pulmonary disease is a leading cause of morbidity and mortality worldwide. For example, the National Institutes of Health report that chronic obstructive pulmonary disease (COPD) is the fourth leading cause of death in the US [1]. It is well established that smoking is the major cause of COPD. However, the exact biological pathway that leads to COPD pathogenesis is uncertain. No single theory seems to encompass all features of COPD and no approach yet has led to a reduction in COPD prevalence or morbidity. Inflammation of airways and parenchyma are consistent findings in COPD. However, the connection between COPD and inflammation is complex [2]. Treatment options for COPD are relatively limited, the most effective being smoking cessation. New experimental tools and techniques are critically needed to diagnose lung diseases early, to study the disease pathogenesis in order to develop new treatments and to monitor effectiveness of these treatments.

Lung imaging can provide regional information about lung structure and function. An excellent representation of lung structure is obtained using computed tomography (CT). New technical developments continue to improve the resolution of CT with the goal to increase sensitivity to detect pathological remodeling of structure. Lung scintigraphy is the only clinically available method to image lung function. However, resolution in scintigraphy is low.

For the diagnosis of lung disease information of lung function is essential. Even though high resolution structural CT scans are available, in clinical practice physicians tend to rely on clinical

history and pulmonary function tests (PFTs) to assess lung function impairment. However, PFTs provide only global information, a single lung function value represents the whole lung. Adding spatial information can improve sensitivity and specificity of lung function measures. Lung function parameters derived from imaging can be more sensitive biomarkers for the early diagnosis of disease, for disease progression monitoring, and to reduce the time to market for newly developed drugs.

Since the early 90s, hyperpolarized noble gases ^3He (HHe) and ^{129}Xe (HXe) have been investigated as non-invasive contrast agents for lung magnetic resonance imaging (MRI) [3] [4] [5]. A variety of acquisition protocols were developed to study several aspects of lung structure and function in lung disease patients. Spin density imaging was shown to depict ventilation defects in asthma [6], COPD [4] and cystic fibrosis [7]. Diffusion methods showed regional septal wall destruction in COPD patients with emphysema¹ [8] [9] and early changes in asymptomatic smokers [10]. Through modelling quantitative estimates of alveolar size were obtained [11]. Mapping of partial oxygen pressure is related to gas exchange impairment [12] [13].

A fundamental difference between HXe and HHe is that HXe dissolves in lung tissues with a partition coefficient of ~ 0.1 [14]. Upon inhalation HXe follows the functional pathway of oxygen exchange in the lung by diffusing from the alveolar air space across the air-blood barrier into parenchymal tissues and entering pulmonary blood flow. In the dissolved phase HXe experiences a shift in its nuclear magnetic resonance (NMR) frequency [15] [16], which allows to distinguish gas phase and dissolved phase xenon magnetization in MRI. In animal studies spectroscopy² [17] and imaging [18] of the dissolved phase was shown. The HXe gas exchange process was studied dynamically in spectroscopy [19]. Modelling of HXe diffusion across the alveolar-blood barrier

¹Emphysema is a pathological condition of the lung microstructure characterized by the destruction of septal walls which provide the surface area for gas exchange.

²NMR spectroscopy obtains whole lung information without spatial encoding. Spatial encoding in MRI requires sufficient signal-to-noise ratio (SNR) to obtain information from smaller samples.

enabled the quantification of gas-exchange parameters such as surface to volume ratio [20], alveolar wall thickness, pulmonary perfusion [21] and diffusion capacity [22]. Also in human studies dynamic spectroscopy [23] and very recently direct imaging of HXe in the dissolved phase [24] [25] were demonstrated. However, the signal-to-noise ratio (SNR) is low in imaging methods directly interrogating the dissolved phase HXe magnetization (since the dissolved phase magnetization is only $\sim 2\%$ of gas phase magnetization). This drove development of an indirect acquisition method called xenon polarization transfer contrast (XTC) [23] [26] [27] [28]. In XTC, HXe is imaged in the gas phase while image contrast stems from HXe exchange with the dissolved phase.

To summarize, pulmonary function tests of the future will be derived from imaging techniques and hyperpolarized ^{129}Xe MRI has the potential to significantly contribute to achieving this goal.

1.2 Problem Definition

Ample technical challenges in HXe production and imaging have until recently prevented the technique from providing high quality lung images. But recent advances in ^{129}Xe hyperpolarization methods [29] opened the door for new developments. Higher polarization levels increase the amount of available magnetization to be used for image encoding. Thus higher resolution images can be obtained and new contrast mechanisms can be explored. However, encoding additional information presents new challenges in particular requiring longer acquisition times. HXe lung imaging is typically performed during a fixed time frame while the patient holds his breath (10 - 15 s). This presents an upper limit to the total acquisition time. Moreover the magnetization of hyperpolarized contrast agents is in a non-equilibrium state which decays irrevocably during the course of image acquisition. Therefore speeding up the time required for image encoding is inevitably linked to advancements in functional HXe imaging.

Parallel imaging refers to image reconstruction methods developed during the late 90s for conventional proton MRI to speed up the image acquisition by recording the image signal in parallel,

using multiple receivers. Today parallel imaging is a clinical standard to accelerate or improve image resolution in most MRI acquisition protocols. However, for the implementation of parallel imaging dedicated hardware is required, specifically multi-channel receive array coils³.

Having the ability of faster acquisition, new contrast mechanisms to encode lung function parameters can be explored. In particular the ability of HXe to dissolve in lung tissue offers opportunities to obtain functional image contrast related to gas exchange in the lung. However, low SNR has limited techniques directly interrogating HXe in the dissolved phase to either spectroscopical or low resolution implementations. For the indirect method XTC, several gas phase acquisitions are required (before and after contrast encoding and for normalization), which proportionally lengthens the total acquisition time. Thus only single exchange time encoding was demonstrated in XTC imaging, while encoding of multiple exchange times was limited to spectroscopy.

1.3 Objectives

In this thesis I describe my work addressing the need to accelerate image acquisitions by developing a human chest coil to support parallel imaging for HXe. I further describe the development and initial evaluation of a new functional imaging biomarker to characterize septal wall destruction and septal wall thickness in the lung parenchyma. This constitutes the two objectives of this thesis as follows:

1. *Development of a multi-channel receive array coil for parallel imaging with HXe to address the need to accelerate image acquisitions.*

A 32-channel phased-array receiver coil enables acceleration factors up to four for 2D image acquisitions and up to eight for 3D image acquisitions. Due to the unique properties of the non-equilibrium state of the hyperpolarized magnetization, image accelerations do not result

³A radio frequency (RF) coil is a resonant device used to transmit and receive the MRI signal.

in SNR penalties as is the case for conventional proton parallel imaging. In contrast, due to the superior sensitivity of the surface coil receive elements, SNR is expected to be increased compared to previously available volume coils. An integrated asymmetric birdcage transmit coil provides superior signal excitation homogeneity. This is important to make efficient use of the available hyperpolarized magnetization as well as to prevent systematic errors in image contrast caused by a non-uniform signal excitation. With the use of a multi-channel array coil with integrated transmit coil, image acquisition speed as well as image quality can be significantly improved.

2. *Development and initial evaluation of a new functional imaging biomarker to characterize septal wall destruction and septal wall thickening.*

In the lung, HXe is in dynamic exchange between alveolar air spaces and parenchymal tissue structures. A novel acquisition scheme called multiple exchange time xenon polarization transfer contrast (MXTC) is developed. Encoding the time course of the HXe diffusion process allows extraction of two physiologically relevant parameters: 1) the tissue-to-alveolar-volume ratio and 2) the average septal wall thickness. The regional dependence of these two parameters is explored in healthy human subjects and subjects with lung disease. The two parameters have potential as a functional biomarker for emphysematous tissue destruction and regional parenchymal inflammation, respectively.

1.4 Organization

In the following the outline of the remaining chapters in this thesis is summarized:

- **Chapter 2:** This chapter provides background information. First, an introduction to the physiology of the lung describes concepts in structure and function. Gas exchange is introduced as the main function of the lung. Further, lung function tests, obstructive and restrictive lung

diseases, and clinically available imaging modalities are discussed. In the second part of this chapter key concepts in MRI are explained. After some background on spin physics, image encoding is presented. Hyperpolarized gas imaging is introduced as a specialization in MRI and characteristics and image protocols unique to hyperpolarized gas imaging are discussed. Finally an overview of parallel imaging methods is given.

- **Chapter 3:** The design and manufacturing process of a 32-channel phased-array receive coil with integrated asymmetric birdcage transmit coil tuned to the NMR resonance frequency of ^{129}Xe at a 3T MRI system is described. First some background on RF coils is given focusing on surface coil receivers, array design and birdcage transmit coils. In the method section coil design manufacturing processes are described. In the results section, bench testing results of coil electronics are given and parallel imaging performance is evaluated. High resolution images of HXe spin density in healthy subjects and subjects with lung disease acquired with the new HXe chest coil are shown.
- **Chapter 4:** Theory and implementation of a novel HXe imaging technique, Multiple exchange time Xenon polarization Transfer Contrast (MXTC) is described. In the theory section a 1D diffusion model is introduced which yields a fitting equation for HXe gas exchange imaging data. The methods section describes study setup, imaging protocols and methods for data analysis and statistical evaluation. Results demonstrate the sensitivity of the technique by quantifying the well known effects of gravity induced lung microstructure deformation in rabbits and healthy human volunteers while in the supine imaging position. Further, studies in subjects with lung disease show that MXTC is able to depict tissue destruction in emphysema as well as increased septal wall thickness potentially related to inflammation in subjects with obstructive lung disease.

- **Chapter 5:** This chapter summarizes the results of this work, names potential applications and limitations and discusses opportunities for future work.

CHAPTER 2

BACKGROUND

2.1 The Lung

The main function of the lung is the exchange of oxygen from inspired air to the pulmonary blood flow and vice versa for carbon dioxide. The performance of the lung as a gas exchanger is determined by its structural design. In the following the structural design of the lung, key concepts of gas exchange, pulmonary function testing, obstructive and restrictive diseases and imaging methods to diagnose lung disease are described.

2.1.1 Structure

In order to support efficient gas exchange, the surface area where blood and air are in contact is enormous ($\sim 100 \text{ m}^2$, Table 2.1). Providing this surface area within a lung volume of only a few liters requires a sophisticated structure. Three tree structures, the bronchial tree for air flow, the arterial and the venous trees for blood flow, spatially coincide throughout most of the lung. The bronchial tree is a progressively branching structure which consists of 23 generations, where the first 14 generations are conducting airways while gas exchange takes place in the last 8 generations, called the acinar airways [30]. Having a closer look at the branching pattern of the bronchial tree, it is observed that the ratio of length scales from one generation to the next is constant:

$$\frac{l_{n+1}}{l_n} = \text{const} = \lambda \quad (2.1)$$

This property is called self-similarity and is a key concept for fractal trees¹ (Fig. 2-1).

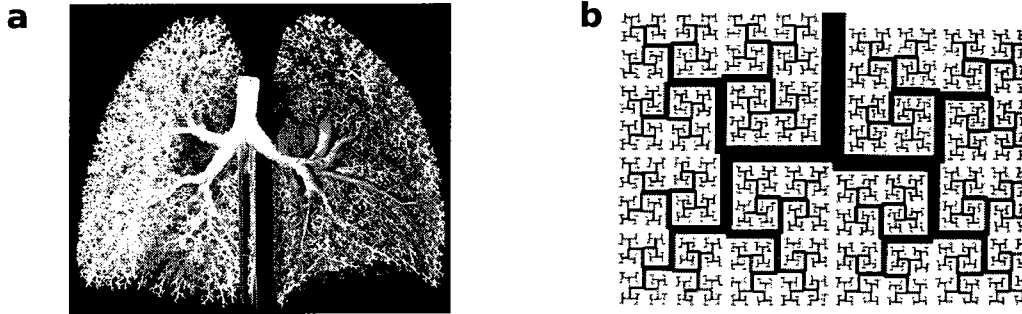


Figure 2-1: Resin cast of human lung and fractal tree of Mandelbrot. The bronchial tree (a, in yellow) exhibits a branching structure characteristic for fractal trees (b). The structure is space filling in order to maximize the surface area available for gas exchange. For the left lung arterial and venous tree are colored in red and blue (a). (a) adapted from <http://www.european-lung-foundation.org> and (b) from [31].

It can be shown that in order to create a 3D space filling tree, the following condition has to be fulfilled:

$$\lambda^3 = 1/2, \quad \Rightarrow \lambda = 0.79 \quad (2.2)$$

Not only for the branching pattern, also for the airway diameter Eq. 2.2 was found to be realized in the lung [32]. According to the Hess-Murray law [33] [34] a tube system designed according to Eq. 2.2 minimizes work to overcome flow resistance by keeping the dead space volume at a minimum. In the human lung it was shown experimentally that $\lambda = \text{const} \approx 0.85$ [35]. The fact that λ in the lung is very close but slightly larger than the optimum condition means that the airway volume is larger than necessary and flow resistance drops gradually with generation - a safety factor in the design.

Beginning at generation 15, alveoli which provide the gas exchanging surface, are bulging out from the airway 2-2a). In total ~ 300 million alveoli are found in the human lung. The diameter

¹A fractal is "a rough or fragmented geometric shape that can be split into parts, each of which is (at least approximately) a reduced-size copy of the whole" [31]

of an alveolus is $\sim 100 - 300 \mu\text{m}$ with an average alveolar wall thickness of $5-8 \mu\text{m}$. The septa² contain capillaries ($\sim 10 \mu\text{m}$ thick) which are separated from the alveolar air space by the air-blood barrier ($\sim 1 \mu\text{m}$, Table 2.1) which contains layers of epithilium, interstitium and endothilium (Fig. 2-2b). In order to support the delicate parenchymal structure a stress bearing fiber system consisting mainly of collagen and elastin is woven into the septa.

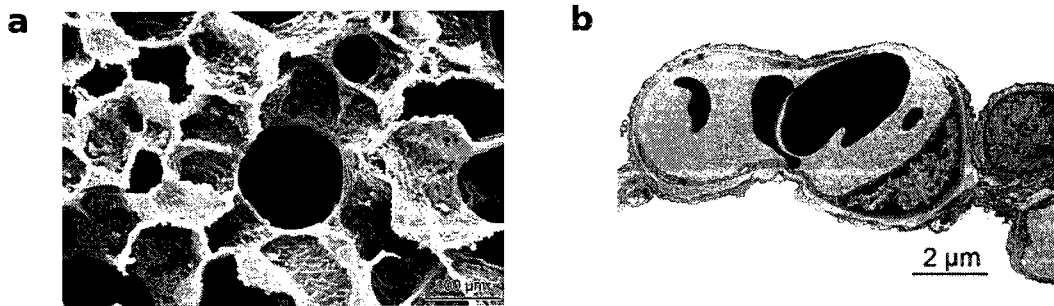


Figure 2-2: Scanning electron micrograph of human lung parenchyma septa. Alveolar duct surrounded by alveoli, which are separated by thin septa (a). Alveolar capillary bounded by endothelial cell sits in alveolar septum lined by type 1 epithelial cells on both sides. Note thin tissue barrier on top and slightly thicker barrier with some connective fibers and fibroblasts at bottom (b). Adapted from [36]

Lung morphometric data mean \pm SE	
Total lung volume (60% TLC)	$4340 \pm 285 \text{ ml}$
Alveolar surface area	$130 \pm 12 \text{ m}^2$
Capillary surface area	$115 \pm 12 \text{ m}^2$
Capillary volume	$194 \pm 30 \text{ ml}$
Tissue barrier harmonic mean thickness	$0.62 \pm 0.04 \mu\text{m}$
Total barrier harmonic mean thickness	$1.11 \pm 0.1 \mu\text{m}$
Diffusing capacity DL_{O_2}	158 ml/min/mm Hg

Table 2.1: Morphometric data for healthy adult lung. Adapted from [36], data from [37] and [38].

²septum/a, a wall dividing a structure into smaller ones

2.1.2 Gas Exchange

Gas exchange is driven by diffusion. Fick's law of diffusion states that the rate of gas transfer is proportional to the surface area S , the gas partial pressure difference between the two compartments ($P_1 - P_2$), and inversely proportional to the air-blood barrier thickness h [39]:

$$\dot{V}_{gas} \propto \frac{S}{h} \cdot D \cdot (P_1 - P_2), \quad \text{with} \quad D = \frac{Sol}{\sqrt{MW}} \quad (2.3)$$

The diffusion constant D depends on gas solubility Sol and molecular weight MW .

At rest, gas transfer rates are $\dot{V}_{CO_2} = 200$ ml/min for carbon-dioxide and $\dot{V}_{O_2} = 250$ ml/min for oxygen. The metabolic scope ($\dot{V}_{O_2,max}/\dot{V}_{O_2,rest}$) for human is about 10 - 12, whereas e.g. for a horse it is 25. The highly optimized structural design of the lung discussed in the previous section supports such high demands on gas exchange capability.

The time required for the RBC (red blood cell) to pass through the capillaries before leaving the gas exchange region is 750 ms. In less than 1 ms oxygen traverses the air-blood barrier and in about 250 ms the partial pressure of oxygen in the blood virtually reaches that of alveolar gas. As a result, gas exchange in the lung is perfusion limited and not diffusion limited. Only during heavy exercise, where due to increased perfusion the capillary transit time might be only 250 ms, or in lung disease patients, where a thickening of the air-blood barrier occurs, gas exchange becomes diffusion limited.

2.1.3 Pulmonary Function Tests

The clinical diagnosis for most lung diseases relies primarily on clinical history and global assessment of lung function provided by pulmonary function tests (PFTs). Spirometry is the most common PFT used to determine relative lung volumes (Fig. 2-3a) by recording a flow volume curve (Fig. 2-3b).

The patient breathes into a spirometer performing a maneuver of maximum inspiration followed

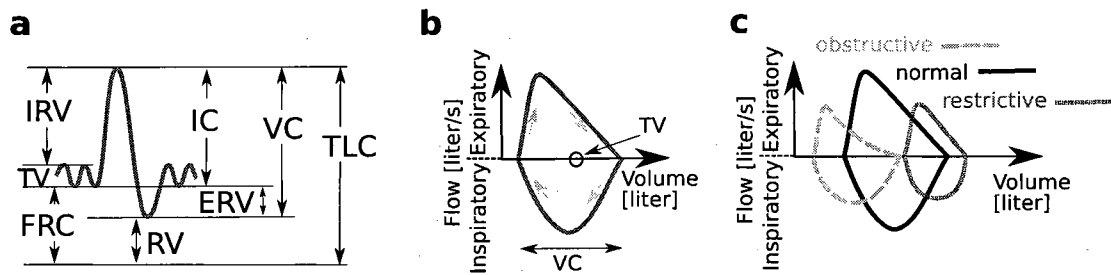


Figure 2-3: Spirometry. Lung volumes and capacities: IRV = inspiratory reserve volume, TV = tidal volume, FRC = functional residual capacity, ERV = expiratory reserve volume, RV = residual volume, IC = inspiratory capacity, VC = vital capacity, TLC = total lung capacity (a). Flow-volume curve, which measures FVC (forced volume vital capacity) and FEV1 (forced expiratory volume within one second) (b). Shape of the flow-volume curves in obstructive and restrictive disease, note the typical scoop-shape in obstructive disease (c).

by maximum flow expiration. The clinically most used parameters derived from spirometry are FEV1 which is the forced expiratory volume within the first second and the ratio of FEV1/FVC (FEV1 divided by the Forced volume Vital Capacity).

Spirometry only provides relative lung volumes. In order to measure absolute lung volumes either a method based on He dilution or a body plethysmograph is used. Other PFTs assess the inequality of ventilation (using single breath nitrogen), alveolar-arterial pO₂ difference, diffusing capacity for CO, airway resistance, lung compliance (using an esophageal balloon), the ventilatory response to CO₂ and hypoxia, or the patient's response to exercise.

However even though PFTs are able to characterize essential lung functionality, results are averaged over the whole lung. This potentially limits their sensitivity to detect lung disease early, monitor disease progression and response to therapy.

2.1.4 Obstructive and Restrictive Lung Disease

Non cancer, non infectious pneumonia lung diseases can be grouped in two classes: obstructive and restrictive disease. Obstructive diseases are characterized by increased resistance to airflow secondary to airway obstruction. The class of obstructive diseases includes asthma and COPD.

Asthma is characterized by the contraction of airways during an attack in response to various stimuli. A thickening of conducting airway walls between 50 and 300 % of normal is observed [40]. Research suggests that airway hyperresponsiveness is a consequence of airway inflammation [41]. Both, asthma and COPD are characterized by inflammation. However whereas in asthma conducting airways are affected, in COPD the destruction of lung parenchymal tissue can lead to emphysema. In COPD one distinguishes two types: Type A with emphysema and Type B with chronic bronchitis. Emphysema is defined as a pathological condition of lung microstructure which is characterized by an “[...] abnormal and permanent enlargement of air spaces distal to the terminal bronchiole, accompanied by the destruction of their walls [...]” [42]. As a result, the surface area available for gas exchange is reduced. Further, the parenchymal structure loses elasticity. A patient with COPD type A typically has problems with expiration due to collapsing airways. Because of accompanying symptoms, Type A is sometimes called “pink puffer”. The second type, type B has chronic bronchitis, which is characterized as excessive mucus production in the bronchial tree [41]. Type B typically is chronically hypoxic and often coughing and is sometimes called “blue bloater”.

Smoking is the main cause of COPD however not all smokers develop clinically significant COPD. This suggests that genetic risk factors play a role for the individual’s risk to develop COPD. No medication yet exists to modify long-term decline of lung function in COPD [1].

In spirometry, obstructive diseases are characterized by a reduced FEV1. The decreased FEV1 primarily results from inflammation and narrowing of peripheral airways. In severe emphysema dynamic airway collapse can further contribute to a decrease in FEV1. The global initiative for chronic obstructive pulmonary disease (GOLD) distinguishes four stages of COPD severity based on spirometric indices (Table 2.2) [1].

In restrictive disease lung expansion is restricted because of pathological alterations in the lung parenchyma or because of disease of the chest wall [41]. For example the principal feature in diffuse interstitial pulmonary fibrosis (also termed idiopathic pulmonary fibrosis or IPF) is the thickening

of the interstitium of the alveolar wall. Restrictive diseases exhibit reduced lung compliance which is characterized in spirometry by a reduced VC and reduced FEV1 while FEV1/FVC is normal.

Stage	FEV1/FVC	FEV1 [% predicted]
I	< 0.7	> 80
II	< 0.7	50 > 80
III	< 0.7	30 > 50
IV	< 0.7	< 30

Table 2.2: COPD GOLD stage classification. Adapted from [1].

2.1.5 Lung Imaging

Diagnostic radiology uses imaging techniques such as chest radiography and computed tomography (CT) to depict lung structure. However even though CT provides excellent representation of structure, clinicians tend to rely on clinical symptoms and measures of lung function. Thus the investigation of structure-function relationships, i.e. how structural pathology detected using imaging correlates with global PFT indices, is an active area of research. Imaging data is analyzed to quantify structural pathology and to define thresholds between disease and normal physiological variation. This is important because subject age, inflation lung volume and subject posture during imaging have an effect on lung microstructure and thus have to be taken into account.

CT is the gold standard for imaging pulmonary structure. CT scans are obtained to depict a variety of lung diseases including pulmonary embolism, fibrosis, bronchial wall thickening in asthma and COPD. The contrast in CT is based on X-ray attenuation which corresponds to tissue density. Attenuation values are converted to Hounsfield units (HU), a scale ranging from -1000 (attenuation of air) to 3000, where the value 0 corresponds to water attenuation. Emphysematous tissue destruction is characterized by pixels with low HU. Gevenois et al found that a relative area occupied by pixels with values less than -950 HU correlated statistically significant with the macroscopic extent of emphysema on *ex vivo* whole lung sections [43]. Coxson et al compared CT measurements

with stereological³ estimates of surface area to obtain a formal relationship which allowed them to predict lung surface area from CT attenuation values [44]. Even though CT is widely used, the radiation dose accompanying each acquisition can be significant. This limits application in young patients or frequent use for treatment monitoring.

Functional lung imaging is obtained using nuclear medicine. Image contrast is derived from photon detection after the radioactive decay of an injected or inhaled tracer (e.g. single photon emission, SPECT). Lung scintigraphy uses radionuclides such as the noble gases ¹³³Xenon and ^{81m}Krypton or the tracer ^{99m}Technetium to depict ventilation, perfusion and ventilation/perfusion ratio (V/Q-ratio). However spatial resolution in lung scintigraphy is very low.

Magnetic resonance imaging (MRI) can also provide functional information and has higher resolution compared to lung scintigraphy. But conventional proton MRI of the lung is challenging due to the low proton density in the lung. Moreover susceptibility gradients caused by numerous air-tissue interfaces cause rapid signal decoherence (see chapter 2.2.3). However using ultra-short-time-to-echo (UTE) acquisition methods, the imaging of parenchymal tissue density is possible [45]. Perfusion can be depicted using fast acquisition sequences [46] or arterial spin labeling (ASL, a spin tagging method). The clinical standard for MRI perfusion scanning uses intravenous injection of a contrast agent (gadolinium chelate). The paramagnetic contrast agent decreases T_1 relaxation⁴ of tissues to which the gadolinium has access. In oxygen enhanced MRI, paramagnetic oxygen is used as a non-invasive contrast agent to depict T_1 shortening in ventilated regions [47]. Furthermore, the T_1 contrast of lung parenchyma reflects oxygen uptake and gas transfer into lung tissue and capillaries. A very recently presented MRI technique uses Fourier decomposition to obtain frequency components corresponding to respiratory and cardiac motion in the MRI data which were acquired

³Stereology is an interdisciplinary field that is largely concerned with the three-dimensional interpretation of planar sections of materials or tissues.

⁴The T_1 relaxation time constant can serve as image contrast in appropriately designed MRI acquisitions (T_1 -weighted acquisitions), see chapter 2.2.3

over several minutes [48]. The data in the respiratory frequency component correspond to ventilation, whereas the cardiac motion frequency component data correspond to perfusion. Thus during a free breathing MRI scan without any contrast agent a ventilation-perfusion map can be obtained.

2.2 Concepts in Magnetic Resonance Imaging

MRI is a non-invasive imaging modality which is widely used to obtain a variety of diagnostic information in hospitals around the world. Images exhibit excellent and versatile soft tissue contrast. Image acquisition does not involve ionizing radiation as is the case in CT or nuclear medicine. MRI is also a very active area for basic and translational research focussing around the development of new contrast mechanisms and faster imaging methods to improve diagnostic capability as well as to tackle fundamental questions in physiology. MRI offers possibilities beyond the depiction of structure. Examples of functional MR include maps of perfusion in MR angiography (MRA), measurements of brain activity in functional MRI (fMRI) or characterization of tissue chemical composition in spectroscopy. In the following section spin physics and image encoding in MRI is described.

2.2.1 Spins and Magnetization

Nuclear magnetic resonance (NMR) is a phenomenon exhibited by certain atomic nuclei which exhibit nuclear spin $1/2$. Proton is a spin $1/2$ nucleus, which due to its high abundance in the human body is the most commonly imaged nucleus in MRI. Other nuclei used in specialized MRI applications include ^{13}C , ^{15}N , ^{19}F , ^{31}P and the noble gases ^3He and ^{129}Xe .

A non-zero nuclear spin is associated with a magnetic moment μ :

$$\vec{\mu} = \gamma \vec{S} \tag{2.4}$$

where γ is the gyromagnetic ratio, which is characteristic for the nucleus and plays an important role in its relative NMR sensitivity. Both, direction and magnitude of the magnetic moment are quantized:

$$\mu_z = \gamma S_z = \gamma m \hbar \quad \text{with} \quad -S \leq m \leq S \quad (2.5)$$

where m is the spin quantum number for the z-component, \hbar is Planck's constant divided by 2π . For a spin 1/2 nucleus there are two possible spin states corresponding to $m = -1/2$ and $m = +1/2$. These states are degenerate hence they will be equally populated at thermal equilibrium. However if an external magnetic field B_0 is applied, the interaction between the nuclear magnetic moment and the external field will cause the energy levels of the magnetic moment to split:

$$E = \mu \cdot B_0 = -\mu_z B_0 = -\gamma m \hbar B_0 \quad (2.6)$$

Here the alignment of B_0 is chosen to be along the z-direction. This phenomenon of energy level splitting is called the Zeeman effect. The energy difference between the two states is proportional to the applied field B_0 and the intrinsic magnetic properties of the nucleus γ :

$$\Delta E = \gamma \hbar B_0 = \hbar \omega_0. \quad (2.7)$$

According to the Boltzmann distribution, there is a small excess of spins in the lower energy state which yields the polarization at thermal equilibrium:

$$P = \frac{1 - e^{-\hbar\omega_0/kT}}{1 + e^{-\hbar\omega_0/kT}} \approx \frac{\hbar\omega_0}{2kT} \quad (2.8)$$

Multiplying the spin excess in the lower energy state with the proton magnetic moment $\gamma\hbar/2$ and the spin density ρ_0 yields the magnetization of an NMR sample:

$$M_0 = P \cdot \rho_0 \cdot \frac{\gamma \hbar}{2} = \frac{\rho_0 \gamma^2 \hbar^2}{4kT} \cdot B_0 \quad (2.9)$$

2.2.2 Signal and Noise

Even at the high field strengths used in NMR and MRI (few Tesla) the thermal polarization is very small (on the order of 10^{-5} at 1T and room temperature). In 1946 Bloch and Purcell independently developed a resonance approach for the detection of the NMR signal [49] [50]. Applying electromagnetic radiation corresponding to the frequency of the energy level splitting will cause transitions (absorption and emission) between the energy levels. In the classical picture this corresponds to a tilt of the magnetization vector away from its longitudinal alignment and subsequent precession around the external field direction:

$$\frac{d\vec{M}}{dt} = \gamma \vec{M} \times \vec{B}_0 \quad (2.10)$$

The solution of Eq. 2.10 for the precessing transverse components is given by:

$$M_{\perp}(t) = M_x(t) + iM_y(t) = M_0 e^{-i\omega_0 t + i\Phi_0} \quad (2.11)$$

The spin precession frequency ω_0 is given by Eq. 2.7. The ‘‘Larmor equation’’ relates the applied external field strength to the spin precession frequency:

$$\omega_0 = \gamma \cdot B_0 \quad (2.12)$$

At typical experimental field strengths used in NMR and MRI (few Tesla) the frequency of nuclear precession ω_0 is in the radio-frequency (RF) range (MHz).

In an NMR experiment an RF coil is used to excite the sample by applying resonant RF radiation as well as to receive the signal from the precessing magnetization. A changing magnetic field

within the sensitive area of a coil will cause a signal (electromotive force emf) to be induced. This phenomenon is called Faraday induction:

$$emf = -\frac{d}{dt}\Phi, \quad \text{with} \quad \Phi = \int \vec{B}d\vec{S} \quad (2.13)$$

For the magnetic flux Φ , the integral is applied to the sensitive area S of the RF coil. Using vector identities and partial integration yields the following form for the emf :

$$emf = -\frac{d}{dt} \int_{sample} d^3r \vec{M} \cdot \vec{B}_r \propto \frac{B_r}{I_r} V_s \omega_0 M_0 \quad (2.14)$$

where B_r/I_r is the receive coil magnetic field generated per unit current, V_s is the sample volume. On a conceptual level this equation is referred to as the ‘‘principle of reciprocity’’ [51] [52], which states that the flux through the detection coil due to the magnetization of the NMR sample equals the flux that would be generated by the RF coil per unit current through the magnetization.

For a given RF coil sensitivity, inserting Eq. 2.9 into Eq. 2.14 yields the signal dependence

$$S \propto \rho_0 \cdot P \cdot \gamma^2 \cdot B_0 \quad (2.15)$$

In MRI two sources of noise are relevant: electronic noise in the coil and noise from the biological sample. At low fields noise is dominated by Johnson noise, which is electronic noise generated by the thermal agitation of charge carriers and due to the RF skin depth effect depends weakly on frequency (resistance $R \propto \omega^{1/2}$):

$$N_{electronic} = \sqrt{4k_B T \cdot R \cdot BW} \propto \omega^{1/4} \propto (\gamma B_0)^{1/4} \quad (2.16)$$

where k_B is the Boltzmann constant, T is the coil temperature and BW is the bandwidth. On the other hand, at high fields and/or large samples, the main source of noise is the sample. Coupling

between RF coil and the weakly conducting sample is inductive which has linear field dependence:

$$N_{sample} \propto \omega \propto \gamma B_0 \quad (2.17)$$

For the two cases, SNR exhibits the following dependence on the external field B_0 :

$$\text{low field:} \quad \text{SNR} \propto \gamma^{7/4} B_0^{3/4} \cdot P \quad (2.18a)$$

$$\text{high field:} \quad \text{SNR} \propto \gamma \cdot P \quad (2.18b)$$

The thermal equilibrium polarization P is proportional to γB_0 (Eq. 2.8). Therefore SNR in the sample dominated regime (Eq. 2.18b) is proportional to the applied external field. This is the reason for the continuous quest for higher field strengths in MRI scanners despite the technical challenges at high fields⁵.

2.2.3 Relaxation

The precessing spins experience two mechanisms of relaxation: 1) “spin-lattice” relaxation characterized by time constant T_1 and 2) “spin-spin” relaxation characterized by time constant T_2 (Fig. 2-4).

T_1 -relaxation

The interaction of the spin with its surrounding will cause the spin to return to its equilibrium state, i.e. to align with the external field (Fig. 2-4b). This is called “spin-lattice” or T_1 -relaxation:

⁵In hospitals 1.5T systems are more and more replaced by 3T systems. At several research sites whole body 7T MRI scanners are being tested. Challenges at high fields due to the high NMR precession frequency (~ 300 MHz at 7T) are faced in RF coil design as well as transmit field homogeneity as wavelength effects become important. Further the increased specific absorption rate (SAR) at high RF frequencies can cause heating of biological tissue - a safety concern which needs to be addressed.

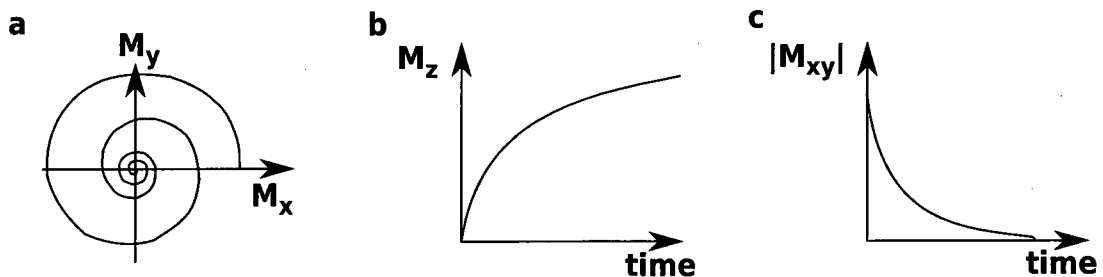


Figure 2-4: Relaxation mechanisms. Following a RF pulse which tips the magnetization vector away from the longitudinal alignment into the transverse plane, spins start precessing around the M_z -direction (a). Two mechanisms of relaxation occur. The longitudinal magnetization recovers with a characteristic time constant T_1 (b). The transverse magnetization decays with a characteristic time constant T_2 (c).

$$M_z(t) = M_z(0)e^{-t/T_1} + M_0 \left(1 - e^{-t/T_1}\right) \quad (2.19)$$

At long times the spin will return to its equilibrium state $M_z(t \rightarrow \infty) = M_0$ given by Eq. 2.9. The length of T_1 is important for imaging applications since once the sample is excited and the signal is acquired, T_1 is the time constant with which spins will align again with B_0 in order to be available for the next acquisition. Therefore T_1 is crucial to determine the total imaging time.

T_2 -relaxation

The loss of transverse magnetization due to the dephasing of spins occurs with a time constant T_2 (Fig. 2-4c):

$$M_{\perp}(t) = M_{\perp}(0)e^{-t/T_2} \quad (2.20)$$

Additional decoherence is caused by the distribution of frequencies secondary to local field inhomogeneities ΔB yielding the effective decay rate T_2^* :

$$\frac{1}{T_2^*} = \frac{1}{T_2} + \frac{1}{2\gamma\Delta B} \quad (2.21)$$

The T_2^* effect is caused either by field inhomogeneities in the external field and/or by susceptibility effects⁶ inside the sample (e.g. air-tissue interfaces in the lung). The external field contribution can be corrected by rephasing the magnetization by creating a “spin-echo” during signal acquisition.

Relaxation times T_1 and T_2 for different biological tissues are given in Table 2.3. Because these two relaxation times are characteristic for different tissues they form the basis for contrast generation in most MRI applications. T_2 is always shorter than T_1 for a given tissue. Depending on image contrast, one distinguishes between T_1 -weighted, T_2 -weighted and proton density weighted images. Other contrast mechanisms include *in vivo* disturbances in the field homogeneity, e.g. caused by the paramagnetic blood (T_2^* -weighted or susceptibility weighted imaging), flow or diffusion.

Tissue	T_1 [ms]	T_2 [ms]	T_2^* [ms]
gray matter	950	100	
white matter	600	80	
muscle	900	50	
cerebrospinal fluid	4500	2200	
fat	250	60	
blood	1200	100-200	
lung parenchyma	1200-1300 ^a	790 ^b	1-5 ^c

Table 2.3: Representative relaxation times T_1 and T_2 for hydrogen components of different human body tissues at $B_0 = 1.5$ T and 37 °C. If not indicated otherwise, adapted from [53]; ^a[54]; ^b[55]; ^c[56]

2.2.4 Bloch Equations

Combining spin precession (Eq. 2.10) and relaxation mechanisms yields the equations of motions for spins in an NMR sample located in an external field. These empirical vector equations are called

⁶Inhomogeneity in the biological sample gives rise to susceptibility gradients $\Delta\chi$ which cause field inhomogeneities $\Delta B = \Delta\chi \cdot B_0$

“Bloch equations” and are the basis to understand contrast mechanisms and image encoding in MRI:

$$\frac{d\vec{M}}{dt} = \gamma\vec{M} \times \vec{B}_o + \frac{1}{T_1}(M_0 - M)\hat{z} - \frac{1}{T_2}\vec{M}_\perp \quad (2.22)$$

2.2.5 Image Formation

Image acquisition in MRI can be understood as a three step process consisting of excitation, image encoding and signal reception. In terms of hardware components, the MRI scanner provides the longitudinal B_0 field and an RF coil applies RF radiation to the sample during excitation and later receives the signal from the precessing spins. Linear field gradients applied by a gradient coil are responsible for image encoding. The interplay of RF radiation pulses and gradient pulses over the time course of image acquisition is called a “pulse sequence” (Fig. 2-5).

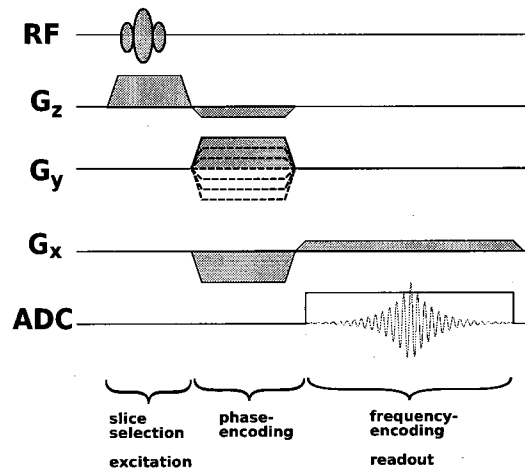


Figure 2-5: Pulse sequence schematic. This example shows a 2D-gradient echo sequence. Shown are image excitation with an RF pulse and slice selection by gradient G_z , phase encoding (2D encoding) by gradient G_y and readout by gradient G_x . Since gradients are balanced, a signal echo occurs during readout. The characteristic time to the echo is called “echo time” (TE). The sequence shown encodes one row in k-space. In order to fill the 2nd dimension of the k-space matrix, the sequence has to be repeated with varying phase-encoding gradients. The time between sequential excitation pulses is called “repetition time” (TR). In order to cover the 3rd dimension, various slices have to be encoded. Therefore the total imaging time is the product of slice number, phase encoding number (resolution in the second dimension) and TR.

Excitation

Excitation refers to the process of applying a resonant RF field (B_1 field) to the sample (“RF pulse”). In the classical picture this results in a rotation of the magnetization vector away from its longitudinal alignment. The tip angle α is given by the time integral over the field amplitude B_1 :

$$\alpha = \gamma \int_0^{\tau} |B_1(t)| dt \quad (2.23)$$

The resulting transverse components of the magnetization vector will start precessing around the B_0 direction with the NMR frequency given by Eq. 2.7.

Imaging

In order to encode spatial information into the signal, linear gradients are applied across the sample region of interest in superposition to the holding field B_0 . Thus the precession frequency of spins in the sample will depend on their relative position within the field gradient:

$$\omega(x_i) = \gamma(B_0 + G_{x_i} \cdot x_i), \quad \text{with} \quad G_{x_i} = \frac{\partial B_z}{\partial x_i} ; \quad x_i = x, y, z \quad (2.24)$$

Note that the field gradients refer to a variation of the B_z -component along the x, y or z -direction. By definition, one distinguishes slice selection gradients along the z -direction, phase encoding gradients along the y -direction and readout gradients along the x -direction. First, the slice selection gradient is applied during spin excitation. The bandwidth of the RF pulse (determined by the Fourier transform of the B_1 field amplitude) will select a sample slice of spins, which have resonant frequencies within the bandwidth of the RF pulse. Subsequently the phase encoding gradient pulse is applied in order to encode additional phase into the spin precession. The magnitude of the additional phase depends on the spin location in the y -direction. Finally, the readout gradient is applied along the x -direction while the signal is sampled. Since the field gradients will cause the spins to dephase,

in a gradient echo pulse sequence gradients are “balanced”. A gradient in the reversed direction with equal time amplitude-area is applied in order to compensate for the spin dephasing caused by the imaging gradient. As a result a signal-echo will occur during read-out (see Fig. 2-5)⁷.

During the application of an arbitrary gradient, the signal originating in spins at a time t can be written as:

$$S(t) \propto \int \rho(\vec{x}) \cdot e^{-i \int_0^t \gamma \vec{G}(t') \cdot \vec{x} dt'} d\vec{x} \quad (2.25)$$

Here $\rho(\vec{x})$ is the spin density at location \vec{x} and $\vec{G}(t)$ is the applied gradient. Using the following simplification

$$\vec{k}(t) = \int_0^t \gamma \cdot \vec{G}(t') dt' \quad (2.26)$$

Eq. 2.25 can be written as:

$$S(\vec{k}) = \int \rho(\vec{x}) \cdot e^{-i\vec{k}\vec{x}} d\vec{x} \quad (2.27)$$

which is the Fourier transform of the spin density:

$$\rho(\vec{x}) = \frac{1}{2\pi} \int S(\vec{k}) \cdot e^{i\vec{k}\vec{x}} d\vec{k} \quad (2.28)$$

Thus, an image can be calculated given that the spin density in each location can be determined after Fourier transform of the frequency sampled signal $S(\vec{k})$. The two (or three-) dimensional spectrum ($S(\vec{k})$ for all \vec{k}) of the object being imaged is called “k-space” and corresponds to a matrix of individual spatial frequencies, which are encoded using field gradients as discussed above. In an

⁷Note that the described “gradient echo” in so called “gradient echo” pulse sequences does not refocus the dephasing due to static-field inhomogeneities (see chapter 2.2.3). For that purpose a so called “spin echo” pulse sequence (not discussed here) is used.

experiment only a finite number of k-space samples $S(\vec{k})$ can be encoded. Two concepts determine the arrangement of k-space samples. First, the Nyquist criterion relates the field of view (FOV), i.e. the spatial extent of the image, to the relative distance of k-space points:

$$FOV \propto \frac{1}{\Delta k} \quad (2.29)$$

Spins outside the FOV, as defined in Eq. 2.29, will lead to fold-over artifacts (“aliasing”) in the image.

Second, considering the corresponding Fourier pair, the image resolution is related to the extent of k-space:

$$\Delta x \propto \frac{1}{2k_{max}} \quad (2.30)$$

There are numerous ways to fill k-space (Fig. 2-6). An encoding trajectory can be chosen for speed, SNR or artifact tolerance. Fast trajectories encode more k-space samples with each excitation, however the tradeoff is that this causes image blurring.

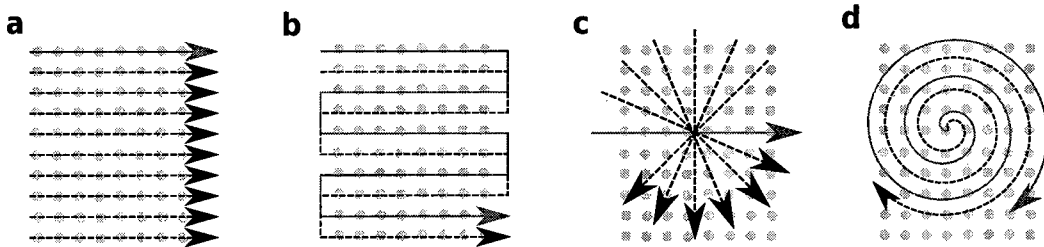


Figure 2-6: Pulse sequence examples. There are various possibilities for k-space trajectories, e.g. cartesian (a), echo-planar imaging (EPI) (b), radial (c), spiral (d).

The SNR for a 2D image acquisition is proportional to the image voxel size, to the square root of the number of excitations (noise averaging) and inversely proportional to the square root of receiver bandwidth BW (noise filtering):

$$SNR \propto \Delta x \cdot \Delta y \cdot \Delta z \cdot \sqrt{N_x \cdot N_y \cdot N_{repetitions}} / \sqrt{BW} \quad (2.31)$$

2.3 Hyperpolarized Gas MRI

MRI is a clinically well established imaging modality to provide structural and functional information for most parts of the human body. However, the lung is a challenging organ to be imaged using MRI. The reason for this is, that the MRI contrast stems from the proton spin magnetization and the tissue fraction in the lung is only between $\sim 10\%$ at TLC [30] and $\sim 40\%$ at RV [57]. Moreover, due to the numerous air-tissue interfaces in the lung, susceptibility gradients cause the signal to dephase rapidly ($T_2^* \approx 1-5$ ms [56]).

In 1994 a paper by Albert et.al. published in Science introduced a new contrast agent to image the lung using MRI: hyperpolarized ^{129}Xe [3]. In the following years, structural and functional imaging of the lung using the hyperpolarized noble gases ^{129}Xe and ^3He became an active area of research. Using hyperpolarization methods the magnetization available for imaging is up to five orders of magnitude higher than in the thermal equilibrium state. Hyperpolarization is obtained using either spin exchange optical pumping (SEOP, used for ^3He and ^{129}Xe) or metastability exchange (used for ^3He). In SEOP, circularly polarized laser light creates electron spin polarization in an alkali-metal vapor (typically Rubidium). This process is called “optical pumping”. The electron spin polarization of the alkali atom is transferred to the noble gas nucleus via collisional spin exchange. In metastability exchange, metastable atoms in a low pressure system are created using radio frequency (RF) discharge. Subsequent optical pumping and collisional spin exchange polarize ^3He nuclei.

Because the polarization in hyperpolarized gas application is generated externally, polarization is independent of field strength. Thus, considering Eq. 2.18b, SNR in the sample dominated regime is independent of field strength. This lead several groups to develop low field ($< 1\text{T}$) hyperpolar-

ized gas imaging. However most of these low field MRI scanners have inferior field homogeneity compared to clinically used high field scanners. Moreover at low fields the coupling to the sample is weak and noise from the coil dominates. As a result low field imaging has not reached the quality of hyperpolarized gas imaging at clinical field strengths (1.5T and 3T).

Only one year after first results of HHe MRI in human lungs was demonstrated [58] [4] [59] [60], human imaging with HXe was shown by Mugler et.al. [5]. However in the following years HHe research lead the field of hyperpolarized gas imaging in humans while HXe was limited to animal studies. This had two reasons: First, hyperpolarization methods for HHe were more advanced and hyperpolarization levels and production rates were higher for HHe than for HXe. Second, because the gyromagnetic ratio for ^3He is by a factor 2.75 higher than for ^{129}Xe (Table 2.4), SNR is higher. Recently however there is increased interest in HXe human imaging. Due to the critical shortage of ^3He supplies⁸ it seems ^{129}Xe is the only alternative for cost-effective large scale clinical applications. Powered by advances in ^{129}Xe hyperpolarization methods [61] [29], HXe imaging is developing rapidly. Imaging protocols initially demonstrated for HHe imaging were successfully applied using HXe and are approaching the quality of HHe images [62]. Exploiting the solubility of ^{129}Xe in lung tissue additional functional protocols were developed studying gas uptake and gas exchange of HXe in the lung.

Compared to conventional proton imaging, MRI using hyperpolarized gases presents unique opportunities and challenges which are discussed in the following sections.

⁸Helium-3 is rare on earth. It is created as a byproduct of tritium decay. Current supplies come from the dismantling of nuclear weapons.

2.3.1 Characteristics of Hyperpolarized Noble Gases ^3He and ^{129}Xe

Non-Equilibrium Longitudinal Magnetization

The most distinguishing feature is that the longitudinal magnetization available for imaging is in a non-equilibrium state. Therefore every excitation RF pulse will irrecoverably destroy a fraction of the magnetization (proportional to $M_0 \cos \theta$, where θ is the excitation flip angle). Over the course of image encoding, magnetization is continuously depleted. Typically fast gradient echo pulse sequences using a low flip angle (e.g. FLASH = fast low angle shot) are used for hyperpolarized gas imaging.

T_1 Relaxation

T_1 relaxation in hyperpolarized gas imaging applications is much longer ($\sim 30\text{s}$, Table 2.4) than proton T_1 in fluids and biological tissues (Table 2.3). It is important to consider that the concept of T_1 for imaging is fundamentally different for proton and hyperpolarized imaging. Whereas in proton applications T_1 determines the time constant for the *recovery* of longitudinal magnetization (thermally polarized magnetization M_0 given by Eq. 2.9), in hyperpolarized studies T_1 determines the *decay* of longitudinal magnetization (since the equilibrium thermally polarized state is much less than the externally created hyperpolarized initial magnetization, $M_z(0) \gg M_0$).

In the lung the presence of oxygen, which is paramagnetic, alters the local fields and causes relaxation of hyperpolarized spins thus contributing to the T_1 relaxation time. This effect is dependent on the partial oxygen pressure and is exploited in pO₂ imaging (see 2.3.2).

Also for experiment planning it is important to consider T_1 relaxation time. After hyperpolarization, the gas is stored in a glass vessel or in a bag to be transported to the imaging site. T_1 relaxation determines the decay of the hyperpolarized state and therefore how critical it is to dose fast. For HHe stored in specially coated glass containers T_1 can reach up to 80 hours. This was successfully demonstrated by imaging a subject in Australia with ^3He gas polarized in Germany and transported

by air to Australia [63]. For HHe experiments a single hyperpolarized gas production site can distribute gas to several imaging centers. This concept is used in practice in Europe by the PHELINET research network, where gas is polarized in Mainz, Germany and distributed to research centers all over Europe. For HXe T_1 is much shorter (~ 2 hours). It is therefore important to have a HXe polarizer on site, i.e. in the hospital or at the research institution where the MRI scanner is located.

Diffusivity

The diffusion coefficients for the gases ^3He and ^{129}Xe (see Table 2.4) are orders of magnitude larger than the proton diffusion coefficient in biological tissue. This causes signal loss due to diffusion attenuation while imaging gradients are applied. On the other hand, the high diffusivity of hyperpolarized gases enabled the development of ADC diffusion imaging which is capable of probing alveolar size in the human lung (see 2.3.2).

Chemical Exchange of ^{129}Xe

While ^3He is practically insoluble in biological tissue, ^{129}Xe is lipophilic. The partition coefficient for ^{129}Xe in tissues is 0.1 [14]. In addition, the large electron cloud of ^{129}Xe interacts with the chemical environment resulting in a range of different NMR frequencies. Thus, upon inhalation various NMR resonances are observed corresponding to HXe in the gas phase (0 ppm), dissolved in tissues or blood plasma (~ 198 ppm) and bound to hemoglobin (species dependent, 200 - 218 ppm) [64] [19] [65] [66]. Further, HXe atoms are in dynamic exchange between these different compartments which has implications for imaging. For example, the effective T_1 relaxation time of the gas phase HXe magnetization is reduced due to loss of hyperpolarized spins in the gas phase upon diffusion into tissue and blood stream. Also T_2 is reduced due to spins diffusing from the gas phase into tissues and blood, where they exhibit a different NMR resonance frequency and accumulate additional phase before diffusing back to the gas phase. On the other hand, HXe exchange occurring between alveoli and lung tissue mirrors the gas exchange of oxygen and carbon-dioxide

which provides a unique opportunity for functional imaging.

	^3He	^{129}Xe
Gyromagnetic ratio γ [MHz/T] ^a	-32.4	-11.8
Abundance [%], natural ^a	1.37×10^{-4}	26
Abundance [%], enriched		86
Diffusion coefficient D [cm ² /s], self ^b	2.05	0.062
Diffusion coefficient D [cm ² /s], air ^b	0.86	0.14
Ostwald coefficient in lung tissue	<0.01 ^c	0.1 ^d
Diffusion coefficient D [cm ² /2], tissue ^e	-	3.3×10^{-6}
Chemical shift range in the lung [ppm]	<1 ^f	~ 250 ^g
T ₁ Relaxation Time in the lung [s]	32 ^h	18 ⁱ
T ₂ Relaxation Time in the lung [s]	2-3 ^j	0.3 ^k
T ₂ [*] Relaxation Time in the lung [ms] at 1.5 T	28 ^l	50 ^m
T ₂ [*] Relaxation Time in the lung [ms] at 3T	14 ^l	27 ^m

Table 2.4: Properties of hyperpolarized gases ^3He and ^{129}Xe . Relaxation times were measured in the human lung unless noted otherwise.

^a [67], ^b [68], ^c [69], ^d [14], ^e [27], ^f [70], ^g [15], ^h [71], ⁱ administered with 21% oxygen [72], ^j rat lung [73], ^k measured at 0.2 T [23], ^l [74], ^m [75]

2.3.2 Imaging Protocols

Spin Density Imaging

Spin density imaging depicts regional ventilation in the lung (Fig. 2-7). The technique was applied to study ventilation defects in smokers [76], asthma [6] [77], COPD [4] and CF (cystic fibrosis) [7] patients and also in healthy elderly volunteers [78]. Dynamic ventilation imaging was used to depict the distribution of ventilation in lung transplant patients [79] and air trapping in obstructive disease [80].

ADC Diffusion Imaging

Diffusion encoding protocols were developed to assess parenchymal microstructure. A Stejskal-Tanner gradient pair inserted in a gradient echo sequence measures the apparent diffusion coefficient (ADC) of polarized spins. Phase accumulation due to a positive gradient lobe is exactly compen-



Figure 2-7: HXe spin density 3D volume acquisition. Coronal, sagittal and axial image slices and a 3D volume rendering from a single 3D HXe acquisition with isotropic 6.4 mm spatial resolution. Images were acquired using the xenon chest coil discussed in the following chapter. Adapted from [81]

sated by a subsequently applied negative gradient lobe for stationary spins. Depending on the gradient strength and the time allowed for diffusion, spins displaced due to diffusion will not become rephased resulting in a signal loss. The ADC derived from the diffusion attenuation is related to the geometrical structure restricting spin diffusion. Short time scale diffusion methods were applied to probe alveolar size and to depict regional air space enlargement due to tissue loss in emphysema patients [82] [83] [84] as well as early changes in asymptomatic smokers [85] [10]. ADC imaging correlated well with PFTs of global lung function [8] and with the clinically established imaging modality for emphysema, CT [9]. Further, ADC imaging was able to depict the gravity-dependent deformation of healthy lung tissue [86] [87] [88]. Through modelling quantitative measurements of physiologically relevant parameters such as mean chord length (L_m) and surface-to-volume ratio (S/V) [11] [89] [90] were obtained. To probe different length scales the range of diffusion times was extended to very short time-scale diffusion imaging [91] as well as to long time-scale [92] [93]. Time scale independent diffusion imaging is enabled by the acquisition of multiple diffusion weightings (“q-space” imaging, [94]). For ADC imaging with HXe (see Fig. 2-8), it has to be taken into account that the ^{129}Xe diffusion coefficient is lower. Thus higher gradients have to be used to encode the diffusion contrast [95] [96].

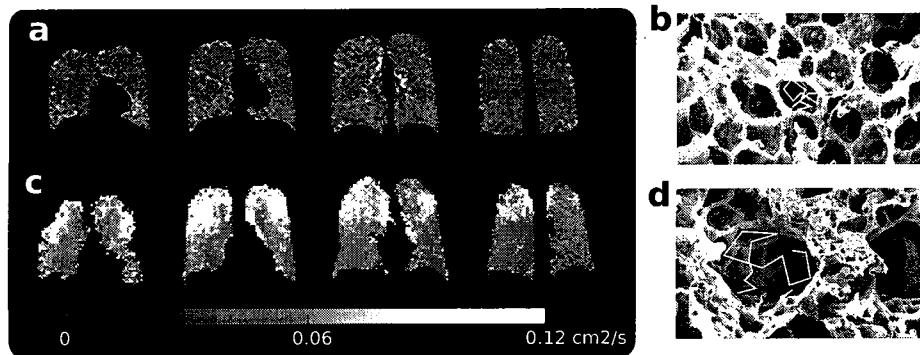


Figure 2-8: ADC diffusion imaging in a healthy subject (a) and a subject with COPD (c). Scanning electron microscopy x400 from healthy mouse (b) and mouse with emphysema after smoke exposure (d). Restricted diffusion path of ¹²⁹Xe schematically shown in yellow. Mean and standard deviation of ADC in subject with COPD (c) is increased (mean \pm std = 0.061 \pm 0.023) compared to ADC in a healthy subject (mean \pm std = 0.038 \pm 0.013). This finding indicates increased regional heterogeneity and increased alveolar size as expected for emphysematous septal wall destruction as shown in (d). (b) and (d) adapted from [97]

pO₂ Imaging

The longitudinal relaxation time T_1 depends on the partial pressure of oxygen. Therefore imaging protocols that measure T_1 relaxation times in the lung are able to measure the regional partial pressure of oxygen (pO₂). The importance of this is evident from the fact, that in regions of the diseased lung, where the exchange of oxygen and carbon-dioxide in the lung is restricted, the alveolar partial pressure of oxygen is increased [12] [98] [99] [100]. For HXe, pO₂ imaging was recently demonstrated in healthy subjects [101] [72] and subjects with lung disease [102].

T_2^* Imaging

Susceptibility gradients at interfaces between air and lung tissue cause rapid dephasing of the transverse magnetization. The time constant of this process T_2^* is therefore related to alveolar size [103]. In vivo results at 1.5 T and 3 T showed approximately linear dependence of T_2^* on field strength [104] [75].

¹²⁹Xe Applications Involving the Dissolved Phase

Unlike HHe, HXe dissolves in parenchymal tissue structures where it experiences a chemical shift of its resonance frequency [15] [16]. Spectroscopy of HXe in a mouse lung revealed several distinct resonance peaks at ~ 190 - 205 ppm [17]. Observing the signal evolution of the resonance peaks while continuously delivering HXe, the authors assigned the three major dissolved phase resonances to HXe dissolved in parenchymal tissue, blood and well-perfused tissue (e.g. heart and muscle). In order to understand the temporal dynamics of HXe as it diffuses into the dissolved phase compartments, a spectroscopical method was developed. Spectrally selective RF pulses saturate the dissolved phase magnetization and after a delay time allowed for diffusion, the signal recovered in the dissolved phase is recorded (Fig. 2-9). Repeating the experiment for several delay times the HXe diffusion process can be quantified with a time constant and a plateau saturation value for the exponential signal recovery function [19]. Through modelling of the HXe diffusion process, important structural parameters of the lung parenchyma related to the gas exchange process were determined such as S/V [20], alveolar wall thickness, capillary diffusion length, pulmonary perfusion, relative blood volume [21] and diffusion capacity [22].

Imaging protocols which directly interrogate HXe in the dissolved phase include chemical shift imaging (CSI) [105], xenon alveolar capillary gas transfer (XACT) [18], Dixon imaging [106]. Since HXe dissolves in the blood, within ~ 4 s it is transported to the brain. Brain spectroscopy and CSI were reported in animal studies [64] [107] and human studies [108]. Very recently two independent studies showed direct dissolved phase imaging of HXe in the lung which were able to depict heterogeneity in gas uptake in subjects with obstructive lung disease [24] [25] [109].

However even after long diffusion times, HXe magnetization in the dissolved phase reaches only few percent of the gas phase magnetization. As a consequence all methods involving HXe dissolved phase magnetization are challenged by low SNR. Therefore implementations were limited to spectroscopy or low image resolution.

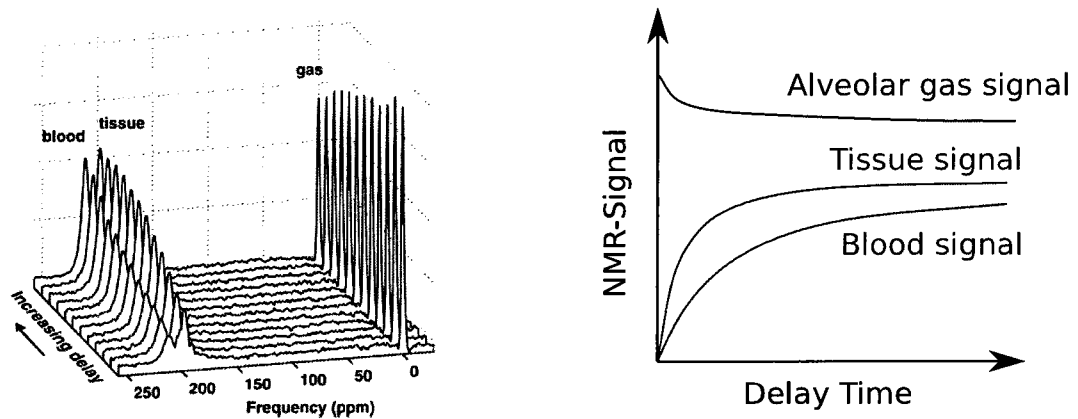


Figure 2-9: Dynamic spectroscopy of HXe spectra in the lung. Due to diffusion of HXe atoms across the air-blood tissue barrier, the spectroscopic signal of the dissolved phase resonances corresponding to parenchymal tissue and blood increases with increasing delay time allowed for diffusion. Note that the spectra are scaled according to the NMR flip angle applied (90° on dissolved phase resonances, $\sim 7^\circ$ on gas phase resonance). Even at long delay times the dissolved phase magnetization reaches only few percent of the gas phase magnetization. Thus the gas phase signal only slightly decreases with HXe uptake in tissue and blood. Adapted from [21]

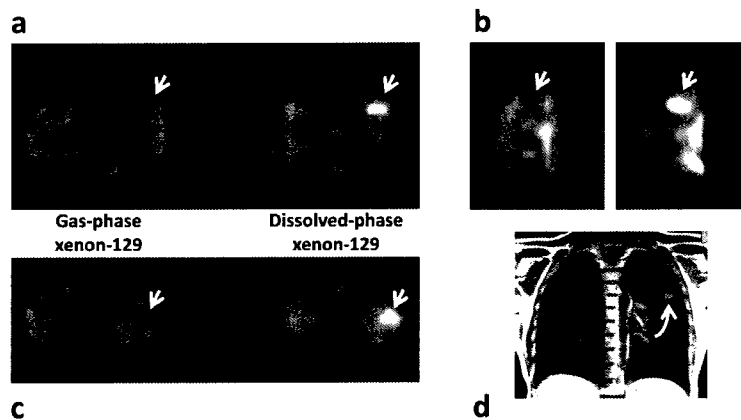


Figure 2-10: Direct dissolved phase imaging of a pulmonary nodule. An incidental finding in a volunteer showing increased local perfusion on direct dissolved phase imaging. The finding was confirmed on a proton HASTE acquisition. Adapted from [109]

In order to obtain information about the dissolved compartment without being limited by the low SNR of HXe in the dissolved phase, Ruppert et al developed a technique called xenon polarization transfer contrast (XTC) [26] [27] [28]. In XTC, HXe is imaged in the gas phase, while spectrally selective RF pulses saturate the magnetization in the dissolved phase. Allowing for a certain time of diffusion the saturated dissolved phase spins exchange with the polarized spins from the gas phase. Repetition of this process results in a measurable reduction of gas phase magnetization. Taking the ratio of HXe gas phase images acquired after and before exchange contrast encoding, yields maps weighted by xenon exchange. Since XTC maps are acquired using gas phase HXe, they have relatively good SNR, while the contrast in the maps stems from the HXe exchange. XTC in humans was first demonstrated by Patz et al [101] [23]. Distinguishing tissue from blood exchange is possible using spectrally narrow saturation pulses [65] and was applied to study sickle cell disease [110].

To summarize, one distinguishes two classes of applications involving the dissolved phase of HXe. While the direct interrogation of dissolved phase HXe, initially demonstrated in spectroscopical applications, can be termed “uptake” experiments, XTC-type imaging can be termed “exchange” experiments. In uptake experiments HXe diffuses and accumulates in the dissolved phase compartment where it saturates in tissues, while HXe dissolved in blood is transported away from the exchange sites in the lung parenchyma towards the heart. Thus uptake experiments involving the blood resonance include perfusion contrast. On the other hand in exchange experiments the contrast stems from HXe exchange between gas and dissolved phase compartments.

2.4 Parallel Imaging

In MRI the total image acquisition time is given by the number of spin excitations times the repetition time (TR). The number of spin excitations is determined by the k-space matrix size which is related to image size and resolution (Eq. 2.29 and Eq. 2.30). Thus, for a given FOV, the total ac-

quisition time is proportional to image resolution. Advances in hardware and pulse sequence design increase SNR and allow for higher resolution imaging which improves the diagnostic capabilities of existing MRI techniques or even enables the detection of previously unseen pathological conditions. In order to keep acquisition protocols at a clinically feasible length, techniques to speed up image acquisition are needed to accompany these advances. Parallel imaging makes use of RF array coils with multiple receiver channels to accelerate image acquisition. The localized sensitivity profiles of the independent coil array elements can be employed to replace gradient encoding steps in the image reconstruction algorithm.

In the final section of this chapter, parallel imaging is introduced as a method to accelerate MRI acquisitions. Hardware and software requirements for parallel imaging are described. This section concludes by discussing the SNR independence of parallel imaging acceleration in hyperpolarized applications.

2.4.1 Phased-Array Coils

Phased-array coils were introduced by Roemer et al in 1990 [111]. While single channel volumetric coils were typically used to cover the sample, it was widely accepted, that the surface coil, a simple resonant circuit loop placed close to the sample, provides the highest possible SNR for a volume at depth equal to its diameter inside the infinite conducting half space. However the surface coil only covers a limited FOV, i.e. only regions as large as the diameter of the coil can be imaged. Roemer realized that similar to phased-array radar or ultrasound applications, surface coils can be combined in an array. The result was a coil with the superior sensitivity of a surface coil combined with an extended FOV. The NMR signal is received simultaneously in each array element. To fully utilize the benefits of the array coil, independent signal reception in each receiver element is crucial. To achieve this, Roemer introduced additional electronics along the signal receive path, designed to prevent coupling between the individual surface coil elements.

In his ground-breaking paper Roemer does not only start a revolution in MRI RF Hardware by introducing the phased-array coil for extended FOV imaging, he also describes image reconstruction algorithms for the parallel received signal. The concepts derived in this paper laid the basis for parallel image reconstruction algorithms which were developed soon after.

2.4.2 Parallel Image Reconstruction Algorithms

In parallel imaging the image acquisition time is reduced by skipping k-space lines. However, if the distance between two subsequent k-space lines is increased, while the total extent of k-space (which determines the resolution, Eq. 2.30) is kept constant, the Nyquist criterion is not fulfilled (Eq. 2.29). Therefore aliasing is introduced, which results in a fold-over artifact in the image. In 1997, Sodickson et al realized that Nyquist undersampled images can be artifact free reconstructed using the localized sensitivity profile information from phased-array coils (Fig. 2-11). He called this algorithm SMASH (simultaneous acquisition of spatial harmonics) [112]. With SMASH Sodickson realized that the superposition of multiple receive coil sensitivity profiles can replace spatial frequency encoding accomplished by gradient phase encoding. Later, many other methods followed, such as AUTO-SMASH [113], SENSE [114], PILS [115] and GRAPPA [116]. These methods employ different image reconstruction algorithms to un-alias the Nyquist undersampled k-space data. They have in common that they depend on the use of phased-array coils. One distinguishes two classes of parallel image reconstruction algorithms: k-space based and image based, depending on if the coil information is employed before or after the Fourier transform. The most commonly used methods today are SENSE, which is image based and GRAPPA, which is k-space based.

GRAPPA

In GRAPPA (generalized autocalibrating partially parallel acquisitions [116]), the Fourier transform (Eq. 2.27) for the y-component (which is the phase encoding direction) is rewritten to incorporate

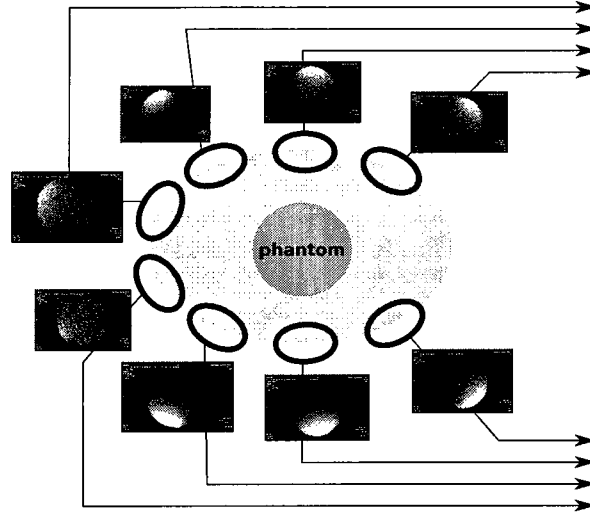


Figure 2-11: Localized sensitivity profiles of receiver channels in an array coil. Data are acquired simultaneously and independently in each channel. Each channel has its dedicated receive path. Thus the data size is proportional to the number of array elements.

the coil sensitivities. Thus the signal in a single coil l is given by:

$$S_l(k_y) = \int dy \rho(y) \cdot C_l(y) \cdot e^{ik_y y} \quad (2.32)$$

where $C_l(y)$ is the variation of the sensitivity profile of coil l along the y -direction. Other k -space lines (at a distance $m\Delta k_y$) are related by spatial harmonics:

$$S_l(k_y + m\Delta k_y) = \int dy \rho(y) \cdot C_l(y) \cdot e^{i(k_y + m\Delta k_y)y} \quad (2.33)$$

Thus, if the k -space lines $k_y \pm m\Delta k_y$ in the neighborhood of k_y are skipped, they can be replaced using a superposition of coil sensitivities $C_k(x, y)$ with weights $n_{k,l,m}$:

$$C_l(y) \cdot e^{im\Delta k_y y} \approx \sum_{k=1}^{N_c} n_{k,l,m} \cdot C_k(x, y) \quad \text{with} \quad k, l = 1, \dots, N_c$$

$$m = 1, \dots, R - 1 \quad (2.34)$$

where the indices k, l run over the number of coil elements and N_c corresponds to the total number of coils in the array, while m runs over the number of skipped k-space lines and R is the acceleration factor. Inserting Eq. 2.34 in Eq. 2.33 yields:

$$S_l(k_y + m\Delta k_y) \approx \sum_{k=1}^{N_c} n_{k,l,m} \cdot S_k(k_y) \quad (2.35)$$

which can be rewritten in matrix form:

$$\vec{S}(k_y + m\Delta k_y) \approx \hat{w}_m \cdot \vec{S}(k_y) \quad (2.36)$$

In GRAPPA the weights are estimated using training data, which are fully sampled k-space lines in the center of k-space (because SNR is at maximum in the center of k-space). Replacing \vec{S} in Eq. 2.36 with these so called ACS (auto-calibration signal) lines, the matrix equation can be solved to determine the weights \hat{w}_m . The non-square matrix $\hat{S}(k_y)$ is inverted using the Moore-Penrose inverse (i.e. instead of simply using \hat{A}^{-1} , for inversion of a non-square matrix $(\hat{A}^H \hat{A})^{-1} \hat{A}^H$ has to be used instead):

$$\hat{S}_{ACS}(k_y + m\Delta k_y) \cdot \underbrace{(\hat{S}_{ACS}(k_y)^H \hat{S}_{ACS}(k_y))^{-1} \hat{S}_{ACS}(k_y)^H}_{\text{Moore-Penrose inverse of } \hat{S}_{ACS}(k_y)} = \hat{w}_m \quad (2.37)$$

where $\hat{S}_{ACS}(k_y)^H$ is the Hermitian conjugate of $\hat{S}_{ACS}(k_y)$. After determining the weights from the ACS lines, the undersampled remainder of k-space can be reconstructed using Eq. 2.36.

SENSE

SENSE (sensitivity encoding [114]) is image based, i.e. the aliasing artifact is removed after the Fourier transform is applied to reconstruct images from k-space. Aliasing causes signals from different spatial locations to occupy the same image voxel. The number of overlapping voxels N_A corresponds to the acceleration factor R if the object size along the phase encode direction equals

the FOV ($R = N_A$). If the object is smaller, then some voxels will have $N_A < R$ and if the object is larger $N_A > R$ for some voxels⁹. Using coil sensitivity information the signal overlap in aliased image voxels can be resolved. To begin, the aliased image \vec{I} can be written as the product of the coil sensitivity matrix \hat{C} and spin density vector $\vec{\rho}$:

$$\vec{I} = \hat{C} \cdot \vec{\rho} \quad (2.38)$$

where the vector \vec{I} contains elements I_i with $i = 1, \dots, N_c$, corresponding to measured signal intensities in respective array elements, while the vector $\vec{\rho}$ contains the spin density values at the true voxel locations ($\vec{\rho}$ contains elements ρ_i with $i = 1, \dots, N_A$). The elements of the coil sensitivity matrix \hat{C} correspond to the coil sensitivity values for all coils (row indices) and all spatial locations (column indices). The matrix equation can be solved to obtain the spin density $\vec{\rho}$ using again the Moore-Penrose pseudo-inverse, since the sensitivity matrix \hat{C} in most cases is not a square matrix (i.e. the number of coils is greater than the acceleration factor)

$$(\hat{C}^H \hat{C})^{-1} \hat{C}^H \cdot \vec{I} = \vec{\rho} \quad (2.39)$$

SENSE vs GRAPPA

SENSE and GRAPPA, even though fundamentally different approaches to reconstruct missing data, provide nearly identical image reconstruction quality [117]. SENSE as a very straightforward and easy to implement approach is available on all clinical MRI systems, thus widely used. If an accurate coil sensitivity map is available SENSE provides the best possible reconstruction with optimized SNR. GRAPPA on the other hand provides robust reconstruction even if accurate sensitivity maps are difficult to obtain, since GRAPPA extracts sensitivity information from k-space. Further, the

⁹If the object is larger than the FOV additional phase wrap cannot be resolved by SENSE reconstruction.

GRAPPA approach of using the central k-space lines employs global information and as a result is relatively insensitive to local inhomogeneities.

2.4.3 SNR in Parallel Imaging

In conventional proton MRI, the SNR is proportional to the number of k-space samples collected (Eq. 2.31). Therefore undersampling as is the case in parallel imaging will decrease SNR proportional to the square root of the undersampling (acceleration) factor R :

$$\text{SNR}_{PI} = \frac{\text{SNR}}{g \cdot \sqrt{R}} \quad (2.40)$$

The g -factor or geometry factor describes additional noise enhancement in the SENSE reconstructed image due to non-orthogonality of receiver channels. In an ideal case, the individual receivers are completely independent (orthogonal) and the g -factor is equal to one. On the other hand if there is a complete overlap of sensitivity regions, the g -factor goes to infinity. Thus for designing an array coil, the g -factor can be simulated to determine the optimum coil configuration for the desired parallel imaging application. Strictly speaking, the g -factor is derived for SENSE image reconstruction however it works for GRAPPA as well, since GRAPPA is subject to the same orthogonality condition for receiver channels.

2.4.4 Parallel Imaging for Hyperpolarized Gas MRI

In proton MRI, SNR is reduced with increasing acceleration factor, however in hyperpolarized applications SNR does not depend on the acceleration factor. Whereas in proton MRI, the signal during the course of image acquisition is replenished via longitudinal T_1 relaxation, in hyperpolarized MRI the signal is in a non-equilibrium state. Every RF excitation pulse (with flip angle θ) therefore reduces the available longitudinal magnetization M_0 to $M_0 \cdot \cos\theta$. The SNR of an acquisition is determined by the transverse magnetization component ($\propto \sin\theta$) of the center k-space line.

Thus the SNR for a sequential cartesian encoding scheme (see Fig. 2-6 a) is given by:

$$SNR \propto \sqrt{N_{ex}} \cos^{(n_0-1)} \theta \sin \theta \quad (2.41)$$

where N_{ex} is the number of excitations and n_0 is the number of excitations before the center of k-space is reached. Taking the derivative of SNR with respect to θ yields the optimum flip angle [118]:

$$\theta_{max} = \arctan \left(\frac{1}{\sqrt{n_0 - 1}} \right) \quad (2.42)$$

If the optimum flip angle is chosen in hyperpolarized imaging the SNR becomes independent of the number of excitations [118] [119].

Parallel imaging in hyperpolarized MRI is therefore especially suitable to push acceleration factors to the theoretical limit. Even higher acceleration factors could be achieved in future studies by combining parallel imaging with the so called “compressed sensing” image reconstruction, which employs sparsity to reconstruct undersampled acquisitions (a concept similar to jpeg image compression) [120].

The g -factor noise enhancement (Eq. 2.40) still applies to hyperpolarized parallel imaging. Good coil design (channel decoupling) keeps the g -factor at a minimum.

CHAPTER 3

PHASED-ARRAY XENON CHEST COIL

3.1 Introduction

A single RF coil in MRI can serve both purposes, excite spins in the sample and after image encoding also receive the signal from spin precession. However the design goal for RF transmit coils is to create a homogeneous spin excitation in the region of interest in the sample, whereas for RF receive coils sensitivity is the design goal in order to pick up the small NMR signal. Therefore separate coil designs for transmit and receive coils will result in better performance with the tradeoff of a more complicated design.

In clinics today phased-array coils are the state of the art for receiver coils to provide good SNR and parallel imaging capability for fast MRI. Proton phased-array coils with up to 32 receiver channels have become the clinical standard for head and body coils. In research settings up to 128-channel coils are used [121].

The first array coil for hyperpolarized applications was introduced by Lee et al [119]. It was a 24-channel coil for HHe. Lee later introduced a 128-channel HHe coil, which is currently the highest simultaneously useable number of channels available on certain research scanners with extended receive chain hardware. Today commercially available scanners provide up to 32-channel capability. In 2010, Meise et al presented a 32-channel array coil for HHe [122]. To our knowledge the 32-channel coil presented in this work is the first HXe phased-array coil (first results from this coil were presented in 2009 [123]). In 2010 Porea et al also introduced an 8 channel HXe coil [124].

While proton applications use the scanner built-in body coil as transmit coil, for hyperpolarized imaging an integrated transmit coil tuned to the NMR resonance frequency, has to be custom built. Transmit coils can be characterized as single channel volume coils. In practice, the best coil design for homogeneous and efficient spin excitation is the birdcage design, introduced by Hayes et al in 1985 [125]. Space is very limited inside the MRI scanner and an asymmetric coil shape makes optimum use of the available space. An asymmetric birdcage was recently introduced by De Zanche et al as a HHe transmit/receive coil [126]. We incorporated the asymmetric birdcage design for the transmit coil integrated with the 32-channel receive array.

To summarize, we decided on a 32-channel phased-array receive coil in combination with an integrated asymmetric birdcage transmit coil [123], because this design provides an optimum solution for hyperpolarized imaging by enabling high SNR and parallel imaging capability on the receive side while providing homogeneous spin excitation on the transmit side.

In the following sections some background on RF coil design is given, followed by methods of design and construction of the HXe human chest coil. The chapter concludes with coil characterization and initial imaging results of healthy subjects and subjects with lung disease.

3.2 Background

3.2.1 Why Tuning?

The goal in MRI is to quantify the magnetization in a sample. Typically this magnetization is rather small and thus difficult to detect. In 1946 Block and Purcell discovered that it is possible to detect the variable flux of magnetization by excitation of the sample and subsequent detection of the spin precession via a resonant approach. The signal generated in the receiver loop can be improved by using a resonant device. The *emf* induced in the loop is multiplied by the quality factor Q of the coil (Q is defined as the energy stored divided by the energy dissipated per precession period). However since both, signal and noise are multiplied, the SNR advantage is not obvious at first. In fact, the

SNR is improved by designing the receiver as a filter, where part of the broadband noise is filtered out, while the narrow band signal is passed. Therefore SNR in a resonant receiver is proportional to $1/BW$, where BW is the bandwidth of the filter. The view of an RF coil as a noise filter is illustrated experimentally in Fig. 3-1.

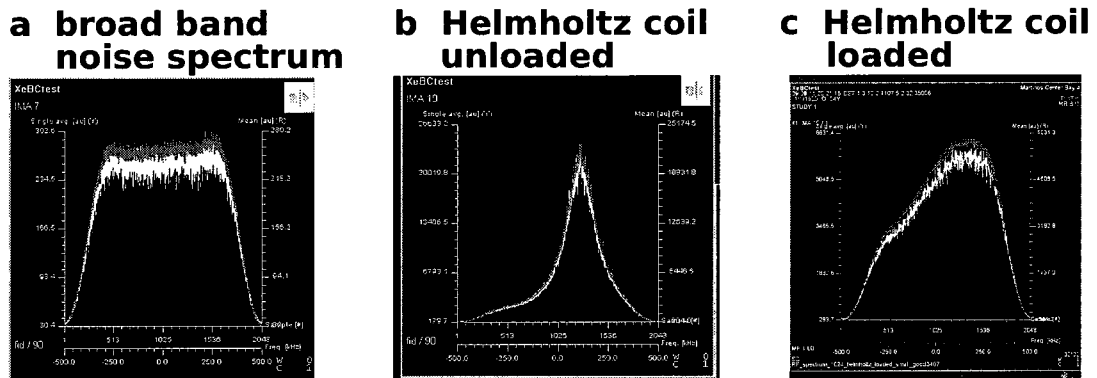


Figure 3-1: The RF coil as a noise filter. The scanner is set to receive broadband noise around the resonance frequency of the coil (a) which is filtered when the unloaded RF coil is plugged in (b). The quality of the coil/filter is reduced as soon as the coil is loaded with the sample, resulting in a lower, broader peak around the resonance (c).

An equivalent circuit for a simple surface coil is shown in Fig. 3-2, consisting of resistance R (to represent noise) and inductance L (the coil loop). Introducing a capacitor C in a parallel resonant circuit RLC configuration as shown, makes the coil act as a filter for the noise transmission. The resonance frequency ω of the RLC circuit is given by

$$\omega = \frac{1}{\sqrt{LC}}. \quad (3.1)$$

At the resonance frequency, the impedance of the circuit is purely resistive, i.e the imaginary part is zero (inductor and capacitor cancel each other), and thus at a minimum ($R = R(\omega)$). In high Q coils, the resistance is only a few Ohms.

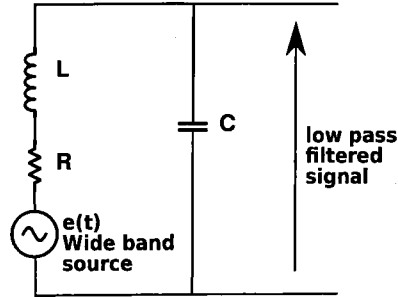


Figure 3-2: Surface coil equivalent circuit. Resistance (R), inductance (L) and capacitance (C) in parallel RLC configuration.

3.2.2 Why Matching?

Matching refers to impedance matching of the low impedance resonant coil to the 50 Ohm signal transmission line leading to the preamplifier. There are three reasons for matching: 1) to avoid reflection of signal power in the transmission line, however this is a broadband effect and therefore has no direct consequence on SNR performance; 2) to maximize the power transfer; 3) to match to the optimum noise figure impedance of the preamplifier¹.

Figure 3-3 shows the frequency dependence of the impedance of a parallel resonant circuit. Graphically, impedance matching is achieved where the real part of the coil impedance curve intersects the 50 Ohm line. At this point the NMR resonance frequency ω_1 is lower (or higher if ω_2 is chosen) than the circuit resonance ω_0 . However at high Q, the width of the resonance peak is narrow, such that the NMR resonance frequency is very close to the parallel circuit resonance ($\omega_0 \approx \omega_1$). The inductive (or capacitive) impedance remaining at the matching point is compensated by a capacitor (or inductor if ω_2 is chosen). If this cannot be achieved with a single capacitor in the loop, other matching circuits are possible, the most simple one is a series match, adding another capacitor in series at one of the outputs. As shown in Fig. 3-3, impedance matching is narrowband. At perfect

¹Even though most preamplifiers are optimized at 50 Ohm, some preamplifiers require 200 Ohm matching.

matching, all power will be dissipated in the coil resistance. As illustrated by the blue curve, which represents the real part of the coil resistance under loaded conditions (higher coil resistance, lower Q), the matching point is shifted. Thus matching has to be done under loaded conditions, i.e. with the sample in place. In practice matching is most easily done on a Smith Chart, which on a polar plot shows real and imaginary parts of the impedance.

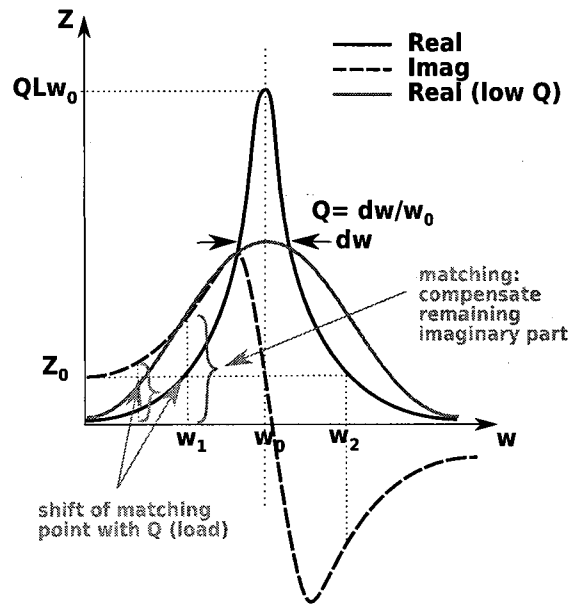


Figure 3-3: Impedance frequency dependence of a parallel resonant circuit, near resonance. The matching point is illustrated where the curve representing the real part of the impedance intersects $Z_0 = 50 \Omega$. A matching circuit is required to compensate for the remaining imaginary impedance. It is further illustrated how the matching point depends on the Q of the coil. Adapted from [127].

3.2.3 Array Design

In order to build an array, multiple surface coils need to be placed next to each other. However, upon bringing two resonant circuits close to each other, their mutual inductance will cause the initial single resonance frequency to split (Fig. 3-4). Considering the coupling effect of coil 2 on coil 1, the impedance Z_{coil} is given by [111]:

$$Z_{coil} = R_1 + \frac{\omega^2 L^2 k^2}{R_2 + Z_1} \quad (3.2)$$

If coil 2 would not exist, the impedance of coil 1 would equal R_1 . The second term in Eq. 3.2 represents the noise power coupled between the coils, where k is the mutual inductive coupling constant and Z_1 is the impedance seen by coil 2. The coupling term approaches zero if either Z_1 is made very large or the coupling constant k is made zero. In this case the total noise resistance equals that of a single isolated coil. In practice two approaches exist: 1) critical overlap to eliminate coupling k and 2) “preamplifier decoupling” to make impedance Z_1 very large. Approach 1 is achieved by overlapping two neighboring coils, i.e. adjusting the distance between coil centers such that a critical overlap is achieved at which the mutual inductance cancels (Fig. 3-5). Critical overlap designs however only minimize coupling between nearest neighbors. For next nearest neighbors additional decoupling is provided by “preamplifier decoupling”. In this method, the low input impedance of the preamplifier is transformed via a $\lambda/4$ cable to a high impedance at the coil. In practice, the impedance transformation can also be achieved with a lumped element circuit (π - or T-circuit) instead of the $\lambda/4$ cable.

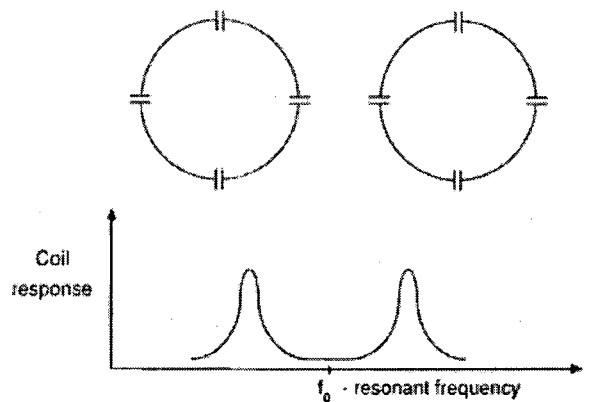


Figure 3-4: Frequency split caused by two resonant circuits. Adapted from [111].

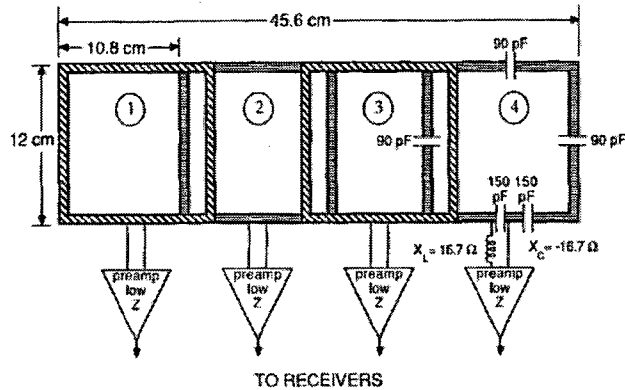


Figure 3-5: Resolved frequency split by critical overlap of neighboring coils. Adapted from [111].

Since the transmit coil is separate, additional design criteria have to be accomplished. During signal transmission the receiver surface coils have to be detuned in order not to disturb the transmit B_1 field. Active detuning during transmit is also an important safety concern, since a resonant coil can focus the transmit B_1 field onto certain body parts which could locally increase SAR (Specific Absorption Ratio measured in W/kg) levels beyond safety thresholds. To achieve active detuning a resonant trap circuit is implemented in each receiver which is switched using a PIN diode activated by the MRI scanner (“active detuning”).

3.2.4 Transmit Coil

The design goal for a transmit coil in MRI is to obtain a homogeneous spin excitation (B_1 field) throughout the sample volume. Theoretically this is achieved either 1) by a uniform current distribution flowing on the surface of a sphere or 2) by a cosine distribution of line currents flowing on a cylinder surface. The created B_1 field is perpendicular to the current flow direction, i.e. in case 1) parallel to the symmetry axis of the coil geometry (“axial resonator”) and in case 2) perpendicular to the axis of coil geometry (“transverse resonator”).

The most simple approach for a case 1) axial resonator is the Helmholtz configuration, which consists of two large loops separated ideally by a distance equal to the loop radius. In this design the sphere surface is reduced to a representation by the two loops. This design was implemented in our coil as a prototype. However the homogeneity was poor, resulting in up to 50% B_1 variations across the region of interest. The simple design and implementation comes with the tradeoff of low field homogeneity².

In 1985 Hayes et al introduced the birdcage design, which is a transverse resonator (case 2). The birdcage design provides excellent B_1 homogeneity and until today is probably the most common transmit coil (often also used as transmit/receive coil). The birdcage design is implemented in most clinical MRI scanners as the integrated “body coil”. A further advantage of the birdcage design is that it is naturally driven in quadrature mode thus providing a circular B_1 which has higher efficiency by a factor of $\sqrt{2}$ than a linear B_1 . The equivalent circuit of the birdcage design is a ladder network of filters. These can either be high pass or low pass filters depending on if the tuning capacitors are placed in the endrings or the legs (Fig. 3-6).

Upon excitation, waves propagate through the filter network. At certain frequencies the waves combine constructively, which are the resonant modes of the birdcage. In the high pass filter design higher order modes are of lower frequency than the resonant mode, whereas in the low pass filter design higher orders correspond to higher frequencies. The excited currents flowing in the birdcage legs have a cosine distribution:

$$I_n = I(2N) \cos(\theta_n + \Phi) \quad (3.3)$$

where n is the leg number, I_n is the current flowing in the respective leg, θ_n is the relative angle to determine the leg position and Φ is the spatial phase factor which is defined by the driving ports

²A similar Helmholtz transmit coil by Meise et al also showed 50% B_1 variation [122]

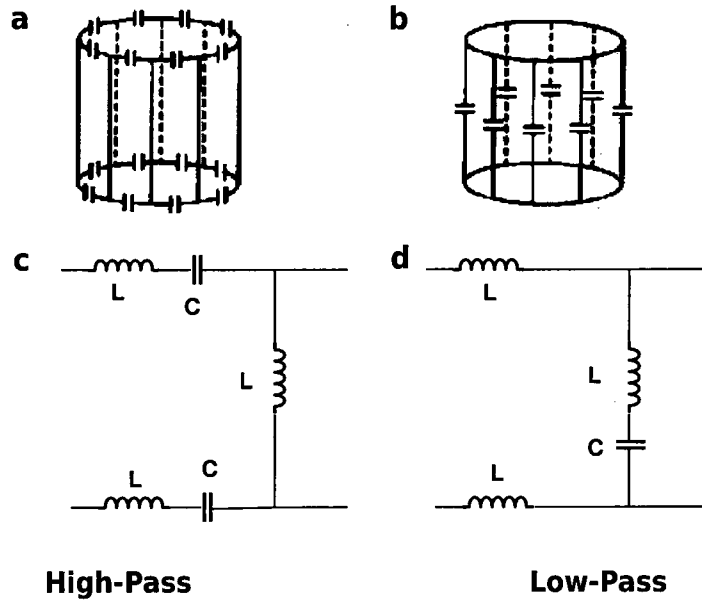


Figure 3-6: High- and Low-Pass birdcage design (a,b). Equivalent circuit diagrams showing one representative element of the ladder network (c,d). For the high pass design capacitors are placed in the endrings (a,c) while for the low pass design capacitors are in the legs (b,d). In the high (low) pass higher order modes are lower (higher).

and which will determine the orientation of the resulting B_1 field. The superposition of fields created in each leg yields the B_1 field amplitude, which is given in the center of the birdcage by (for exact derivation see e.g. [127]):

$$B_y = \frac{2v_0 I}{\pi d} \frac{l}{\sqrt{l^2 + d^2}} \left(1 + \frac{d^2}{l^2 + d^2} \right) \cdot \zeta \quad (3.4)$$

Here v_0 is the NMR resonance frequency, l and d are the long and short axis of the birdcage cylinder and ζ is a shape factor that depends on the number of legs in the birdcage. For a 12 rung this factor is approximately 0.78.

Due to space constrictions in the magnet bore (which is 60 cm in diameter), for our purposes an asymmetric geometry taking into account the available space determined by the circular bore and patient bed, was the only solution to fit a transmit coil, a receive array and (importantly) a patient.

However this significantly increases the complexity in tuning the birdcage. In order to achieve a homogeneous B_1 field, symmetry is important. In the original birdcage with perfect cylindrical geometry the symmetry is easily realized by placing equal value capacitors in the circular endring. Leifer et al introduced elliptical birdcages [128]. He showed that using conformal transformation mapping the leg positions from a circular to an elliptical cross section yields a good approximation to the optimum cosine current distribution. As a result, the legs are spaced unequally in physical angle, but they are located at equal increments of electrical phase. De Zanche et al went on to extend the conformal mapping approach to an asymmetric design [126]. We followed his approach for our asymmetric birdcage design. Figure 3-7 shows the geometry of our asymmetric birdcage design together with a schematic illustrating the cosine current distribution.

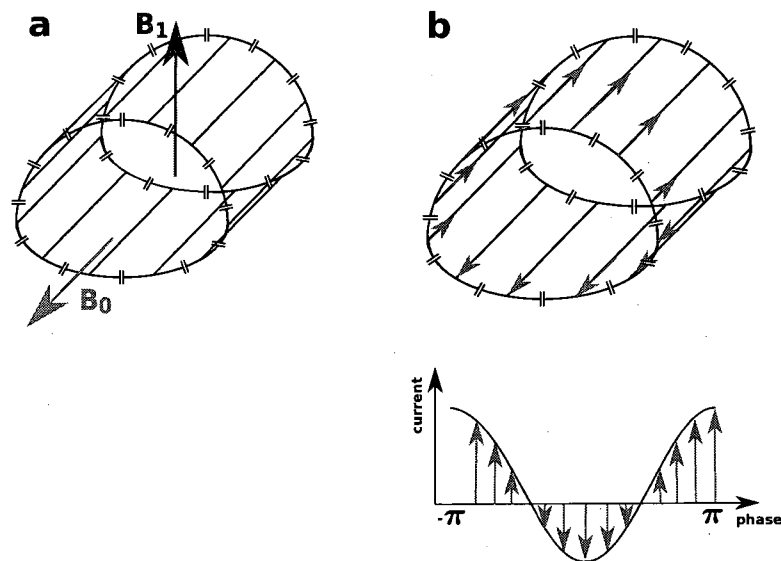


Figure 3-7: Schematic of the asymmetric birdcage coil. The birdcage is a transverse resonator, i.e. the created B_1 field is perpendicular to the coil geometry (cylinder) axis (a). The ideal current distribution for a homogeneous B_1 field is a cosine distribution (b). Our coil shape consists of a circle with radius $r=11.1$ inch and a partial ellipse with axis $a=11.1$ inch and $b=5.6$ inch.

For such a coil geometry, De Zanche et al simulated the B_1 field using the method of moments, which is a numerical method to obtain the B_1 field by superposition of fields created from small current elements. The simulation shows that even using an asymmetric design, excellent field ho-

mogeneity can be achieved if the conformal mapping approach is used (Fig. 3-8).

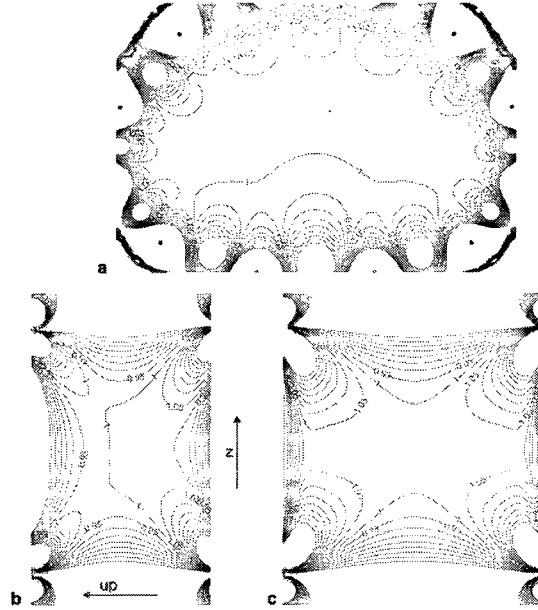


Figure 3-8: Transmit field simulation for the asymmetric birdcage. B_1 field map simulated using the method of moments in (a) transverse, (b) sagittal and (c) coronal views. The contours are normalized to 1 representing the amplitude at iso-center. Excellent field homogeneity is achieved throughout most of the volume even for the asymmetric shape. Intensity fall-offs occur towards the endrings in the sagittal view (b) which has to be taken into account when designing the length of the birdcage. Adapted from [126].

Considering the chain network equivalent circuit of the birdcage coil (Fig. 3-6), a matrix approach is suitable to analyze the network. If A is the matrix, describing the impedances of the network chain, input voltage v_1 and current i_1 are related to output v_2 and i_2 as

$$\begin{pmatrix} v_1 \\ i_1 \end{pmatrix} = A(\omega) \begin{pmatrix} v_2 \\ i_2 \end{pmatrix} \quad (3.5)$$

Closing the chain network in a circular configuration as is the case for the birdcage means practically shortening input and output. This yields the resonance condition for the birdcage coil:

$$A^{2N}(\omega) = I \quad (3.6)$$

where N is the number of legs and I is the identity matrix. This equation can be solved by calculating the eigenvalues of A . The solution of the eigenvalue equation yields the resonant frequency modes (for details see e.g. [127]).

For the asymmetric high pass birdcage the eigenvalue equation can be written as [126]:

$$\begin{bmatrix} EV_A \\ EV_B \end{bmatrix} = \lambda \begin{bmatrix} LV_A \\ LV_B \end{bmatrix} \quad (3.7)$$

where L is the matrix of the birdcage meshes' mutual and self inductances, v_A and v_B are the eigenvectors with sin and cos-current distributions respectively and eigenvalue λ . The resonant mode frequency ω is given by $\lambda = -\omega^2$. In order to tune the asymmetric birdcage, the inductances L can be measured and the capacitors can be calculated solving Eq. 3.7 [126].

To relate the transmit coil to the MRI scanner, the coil is fed through two ports which are spatially separated by 90° , e.g. in our 12 rung birdcage the feed ports were chosen at rung 5 and 8 (Fig. 3-9). The two ports are driven 90° out of phase. Further, the transmit coil needs to be switched from the transmit channel during the transmit phase to an "off"-state during the receive phase in the imaging sequence. Both purposes are solved by implementing a "quadrature hybrid". The quadrature hybrid is a four port network which is switched using PIN diodes between two ports (Tx="on" corresponding to MRI scanner transmit signal and in our case since the receive coil is the separately implemented array, Rx="off" sent to ground) to send a signal with 90° phase shift to two remaining ports, which are connected to the feed points of the birdcage coil (Fig. 3-9).

One important point to be taken into account when designing transmit coils is that voltages V_c across capacitors can be quite high:

$$V_{c,peak} = \sqrt{2PR^{-1}X_L} \cdot \xi^{-1} \quad (3.8)$$

Here P is the transmit signal power, R is the coil resistance, X_L is the impedance of the coil

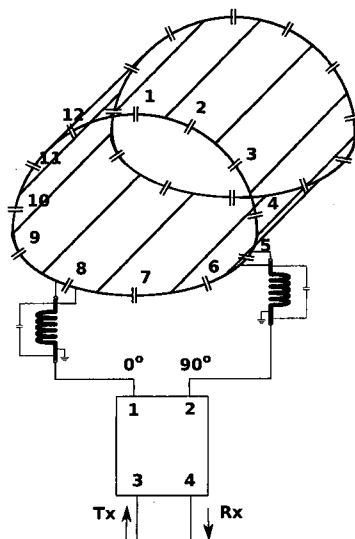


Figure 3-9: Schematic of the asymmetric birdcage coil connected to the quadrature hybrid. The feed ports to drive the birdcage coil are at ports 5 and 8, which are connected to a quadrature hybrid feeding the signal 90° out of phase. Trap circuits at the feed ports prevent common mode currents flowing on the shield of the coaxial cables limiting signal transmission.

inductance and the factor ξ equals the number of capacitors in the simplest case of a loop coil with distributed capacitors in series. The high power transmit signals are transmitted through 50 Ohm cables keeping voltage requirements on components along the transmit path, e.g. in the T/R switch, relatively low. However the resistance in the coil itself can be as low as a few Ohms for a good Q coil at the resonance. Considering that the RF power amplifier provides several kW of transmit power (up to 32 kW for proton body coil, 8kW for multi-nuclear local transmit coil in Siemens MRI systems), according to Eq. 3.8, voltages across capacitors in the transmit coil can reach up to few kV. If components are chosen which do not have sufficient voltage tolerance, arching might occur which can be a risk to the patient. Arching will also distort transmit RF pulses and eventually destroy coil components.

3.3 Methods

3.3.1 32-Channel Phased-Array Receive Coil

Clinical MRI scanners allow for a maximum of 32 receiver channels. We therefore decided on a 32-channel phased-array receive coil. The 12 cm diameter of the coils was determined by the FOV to be covered. The coils were arranged on a rigid former in a hexagonal tiling pattern with 15 elements on the top shape and 17 elements on the bottom shape (Fig. 3-10a). In order to achieve decoupling by critical overlap the center-center distance between coils is $0.75 \times$ diameter.

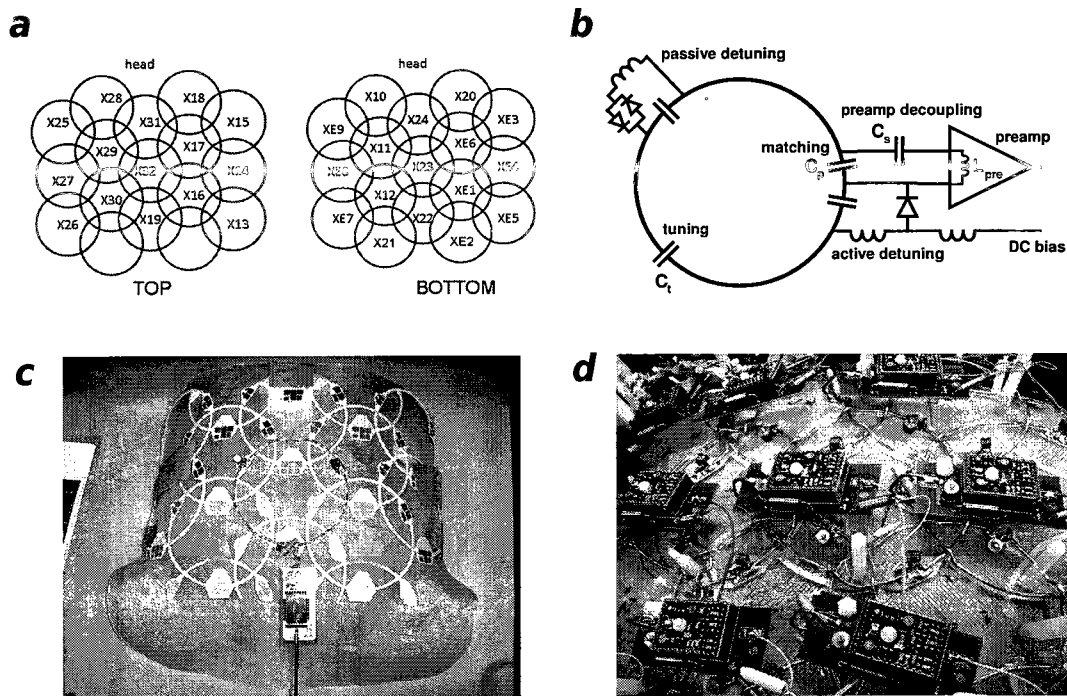


Figure 3-10: 32-channel phased-array. The array layout contains 15 elements on the top chest plate and 17 elements on the bottom plate (a). Array elements are placed in critical overlap with each neighbor in a hexagonal tiling pattern. Circuit diagram of the individual element contains tuning and matching capacitors, passive detuning trap circuit, preamplifier decoupling parallel resonant circuit, active detuning bias line with chokes to separate RF from DC lines (b). The top array during the manufacturing process with solder pads for components (c). The finished array with preamplifiers directly mounted above surface coil receivers (d).

For the individual surface coil design, in order to optimize performance, the Q-ratio (the un-

loaded to loaded quality factor of the coil) has to be optimized. We compared different approaches for element design: single and double wound circuit board layout, wire coil. Q-factors, advantages and disadvantages of the different approaches are summarized in Fig. 3-11 and Table 3.1. We decided on the wire design (copper wire, AWG 12) since it provided the best Q-ratio. The advantage of wire coils compared to circuit board coils was already discussed by Wiggins et al [129]. An additional advantage of the wire coil design is that the area fraction covered by copper is reduced thus minimizing eddy current effects which is especially important for sequences with high gradient slew rates (e.g. diffusion sequences).

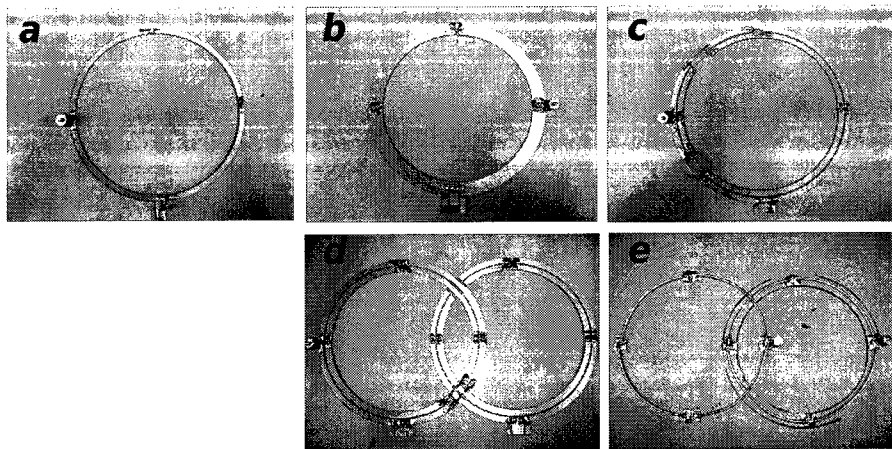


Figure 3-11: Comparison of surface coil designs. Coils (a-d) are manufactured from FR4 circuit board, whereas coil (e) is manufactured from AWG 12 tin plated copper wire.

Coil	Q	Qratio	comments
1. single turn thin	224	3.2	easy to implement
2. single turn thick	275	3.9	high cap values (550pF)
3. single turn thick	292	4.1	better cap values (220pF, 100pF)
4. double turn	323	4.6	
5. wire coil	433	5.75	more difficult to implement

Table 3.1: Comparison of Q-factors for different surface coil designs. Coil 1-4 were manufactured from FR4 circuit board, whereas coil 5 was manufactured from wire AWG 12. The wire coil showed the best unloaded Q and also the best Q-ratio.

The wire coils were tuned to 34.07 MHz, the resonance frequency of HXe at the 2.96 T field of the Siemens TIM Trio MRI system (Siemens Medical Solutions, Malvern, PA). For tuning non-magnetic low voltage capacitors (11-series, Voltronics Corporations, Denville, NJ) were used. The wire inductor and the capacitors were soldered on a custom cut FR4 circuit board placed on the rigid former (Fig. 3-10c). A decoupled probe was used to measure Q-factors of individual elements with an S21 measurement³. A series match was used to match the impedance of the coil to 50 Ohm. Matching is evaluated using a S11 measurement after attaching a cable across the matching capacitor⁴.

In order to detune the receive elements during transmit a resonant trap circuit is implemented which is switched using an active PIN diode (Richardson Electronics) (“active detuning” in Fig. 3-10b). The MRI system provides up to 32 DC bias lines, which have to be shared since not only 32 receiver channels, but also the transmit coil detuning and the transmit/receive switch incorporate actively switched PIN diodes. Note that sharing of a bias line for diodes will decrease the Q of the trap circuit, because the resistance of the diode is proportional to the bias current and therefore should be avoided wherever possible. The inductors inside the active detuning trap circuit are formed from copper wire in order to achieve a good Q component. Active detuning is measured using the decoupled probe and an S21 measurement. The detuning performance equals the difference between the active detuning circuit turned off and on using the PIN diode. An additional passive detuning circuit is implemented. This circuit turns on if the active detuning circuit fails and the transmit B_1 field excites large currents in the surface coil loop. Bias to the active detuning circuit is given through a

³A decoupled probe consists of two loops which are placed in critical overlap next to each other in order to cancel the mutual coupling. The two probes are connected to port S11 and port S22 of a network analyzer. The network analyzer obtains an S21 measurement by transmitting a broadband signal through port S11 to one loop which interact with the sample and a resonance can be determined by picking up the signal with the second loop connected to S22.

⁴For an S11 measurement the attached cable is connected to one port (S11) of the network analyzer. A broadband signal is transmitted and at the resonance frequency an absorption peak is found. The depth of the peak (in dB) is a measure of power reflection (matching quality at the resonance frequency).

choke (J.M. Miller) in order to separate RF and DC current pathways⁵.

After active detuning is implemented, the individual elements are tuned, matched and decoupled via critical overlap in an iterative fashion building up the array. Individual elements can be turned on or off using a custom designed tuning rig which uses switches to pass and LEDs to visualize DC currents activating the PIN diodes in the active detuning trap circuits. With the help of the rig the coupling between individual elements can be optimized while the complete array is in place.

The preamplifiers are tuned and the noise figure is optimized at the 34.07 MHz resonance (Stark Contrast, Erlangen, Germany). Preamplifiers have low input impedance and specific input phase in order to be implemented for preamplifier decoupling purposes. The preamplifiers are powered from the output using 10 V provided by the scanner. We chose to mount the preamplifiers directly above the surface coil loop. This has two advantages: 1) signal losses caused as the signal is transmitted long distances are avoided and 2) a practical single piece design is achieved rather than having a separate box for the stack of preamplifiers. It is important to consider that preamplifiers are mounted such that they are not perpendicular to the strong B_0 magnet field. Like the well-known Hall effect there is a magnetic field influence on the GaAs-FET transistor in the preamplifier, which depends on the field orientation and has severe effects on noise figure and also input reflection (thus affecting preamplifier decoupling performance inside the magnet).

The preamplifiers are implemented with additional circuitry to achieve preamplifier decoupling, which adds to critical overlap decoupling. Preamplifier decoupling is a crucial part in the array design. In our case we chose to implement preamplifier decoupling using a parallel resonant circuit. The preamplifier input impedance consists of a small real part and a not negligible inductive impedance ($L_{equivalent}$). The matching capacitor C_p (Fig. 3-10b) is chosen such that looking into the coil the impedance equals $50+jX$ Ohm. Then C_s was adjusted so that

⁵A choke is a high impedance inductor (~ 10 nH). Thus the impedance $Z = i\omega L_{large}$ is 0 for DC currents ($\omega = 0$) and large for RF ($\omega \neq 0$). Similarly high impedance capacitors (~ 1000 pF) are used to block DC currents while passing RF currents.

$$j\omega L_{equivalent} = j\omega L_{preamp} - \frac{1}{(j\omega C_s)} \quad (3.9)$$

with $L_{equivalent} < L_{preamp}$. The resulting $L_{equivalent}$ forms with C_p a resonant circuit at the Larmor frequency of HXe which causes a high impedance in the coil (Fig. 3-10b).

The preamplifiers are placed on a circuit board, which was custom designed and incorporated the preamplifier decoupling capacitor C_p (tunable), as well as a path for the PIN diode bias current given through a choke (Fig. 3-12). The preamplifier board further incorporates pads for soldering coaxial input and output cables. On the input side (from the coil) a semi-rigid coax was used to connect the coil to the preamplifier board, whereas on the output side the coaxial cable was combined with cables from other preamplifiers and lead to plugs (Stark Contrast, Erlangen, Siemens) which are connecting the coil to the MRI scanner. Wherever possible pathways of output cables are lead through “virtual grounds” in order to minimize disturbance from electrical fields. Only 31 coils are wired up in order to spare one receive channel to be connected to the transmit coil receive port for testing purposes.

Before the output cables reach the plugs cable traps are implemented to prevent common mode currents which would disturb the transmitted signals (Fig. 3-13).

3.3.2 Integrated Asymmetric Birdcage Transmit Coil

Our initial coil prototype featured a simple Helmholtz coil as the transmit coil. The Helmholtz coil design is the simplest volume coil design. It consists of two loops placed below and above the sample at a distance ideally equivalent to the radius of the loops. However the coil did not provide sufficient B_1 homogeneity.

We therefore redesigned the transmit coil, replacing the Helmholtz coil with a birdcage design. Typically birdcage coils are circular or elliptical, but in order to optimize space available for the patient we implemented an asymmetric birdcage based on a coil designed by De Zanche et al [126].

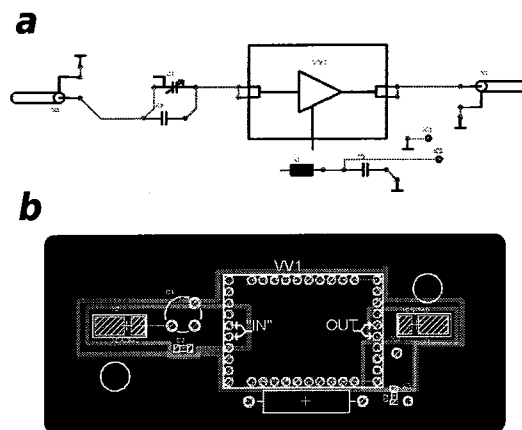


Figure 3-12: A schematic showing the preamplifier board design. The board was design used Eagle Circuit Editor software (Cadsoft Computer, Pembroke Pines, FL, USA). Circuit diagram (a) and board layout (b) contain mounting points for preamplifier sockets, soldering pad for choke for DC bias line, variable capacitor mount for preamplifier decoupling circuit and soldering pads for coaxial input and output cables.

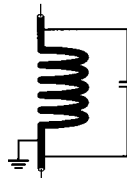


Figure 3-13: Cable trap schematic. Cable traps are implemented to prevent common mode currents flowing on conductor shield. This simple trap forms a resonant circuit by soldering a capacitor onto the ground shield at the endpoints of a coil wound by the cable.

The asymmetric coil consists of a circular top half with a radius of 11.1 inch and a partial ellipse on the bottom with axis $a=11.1$ inch and $b=5.6$ inch (Fig. 3-14). The upper part of the coil is detachable for easy patient access. The two halves are joined together via a mechanical latch with an integrated banana plug which provides the electrical connection. The capacitors are placed in the endrings, which corresponds to a high pass coil, i.e. higher order modes are lower in frequency. This avoids coupling of the HXe birdcage to the proton body coil birdcage, which is at a higher frequency. The HXe birdcage design incorporates 12 rungs. Due to the asymmetric design the capacitors are not of equal value. We started with high voltage capacitors (25-series, Voltronics Corporations, Denville,

NJ), with values approximately 20 % higher than the values reported and theoretically derived by De Zanche et al for a HHe coil [126]. While tuning the coil we tried to contain the symmetry by adjusting capacitors on all positions equivalently.

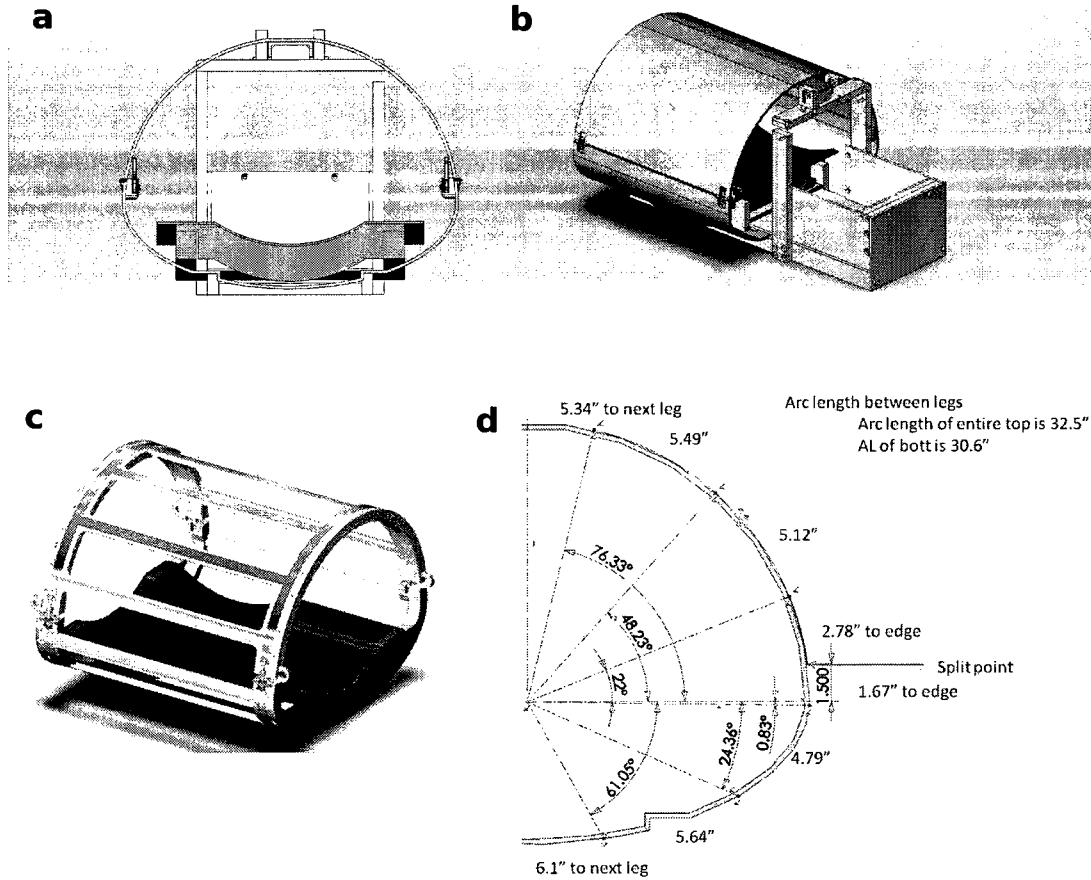


Figure 3-14: Drawings of the asymmetric birdcage. Solidworks drawings show the mechanical shape of the asymmetric birdcage with bottom array plate in place (a,b). Shown are also the handles to open the top half for patient access using a hinge mechanism. A box inside which the patient's head will lie (b) is used to mount cables and also contains the T/R switch. The 12 legs and 2 endrings copper layout is shown in (c) with exact dimensions illustrated in (d).

Unlike the De Zanche coil, our birdcage does not incorporate a shield in order to keep the option for obtaining proton images using the scanner body coil. Since the MRI system contains an RF shield between the proton body coil and the gradient coils, this shield couples to our unshielded birdcage transmit coil when it is positioned inside the MRI scanner. We therefore needed to tune and

match the coil in an environment that matches the properties of the body coil shield. A simulator with similar dimensions was developed inside which tuning and matching of the transmit coil was performed (Fig. 3-15).

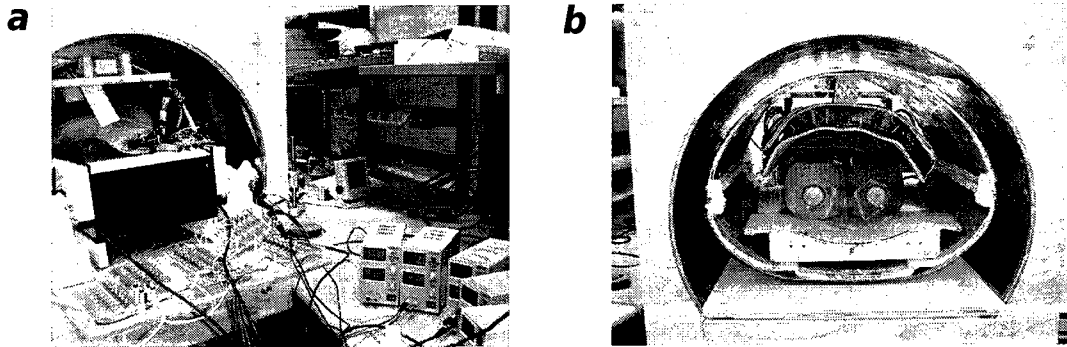


Figure 3-15: Tuning setup for coil tuning. The setup consists of a bore simulator which simulates the RF shield inside the MRI system. Further, salt water phantom bottles simulate body load. A custom designed circuit board rig enables switching on and off of individual receive elements in the array using the PIN diode activated active detuning circuits.

The resonant modes of the birdcage were measured using either an S11/S22 measurement by connecting a cable to the feed ports (rung 5 and 8, see Fig. 3-9) or using a decoupled probe and measuring S21 within the coil volume. The S21 measurement can also give an estimate of field homogeneity by probing the field amplitude at different positions within the volume of interest. During tuning it was also important to minimize the coupling between the two perpendicular resonant modes in order to optimize the coil for quadrature performance. The mode coupling was measured by measuring the transmission between the feed ports using an S21 measurements.

The transmit coil needs to be detuned during receive in order not to couple to the receive array during signal acquisition. To detune the transmit coil, high power PIN diodes (Microsemi Corporation, Irvine, CA) are incorporated in the endrings which are switched by DC bias lines connected through a choke.

In order to switch the signal pathway between transmit and receive states, a quadrature hybrid is implemented. This is a four port circuit which additionally implements a 90° phase shift between

two output ports using $\lambda/4$ transmission lines (Fig. 3-16). Quadrature driving of the birdcage coil results in a circular B_1 field, which increases transmit efficiency by a factor of $\sqrt{2}$ compared to linear driven volume coils.

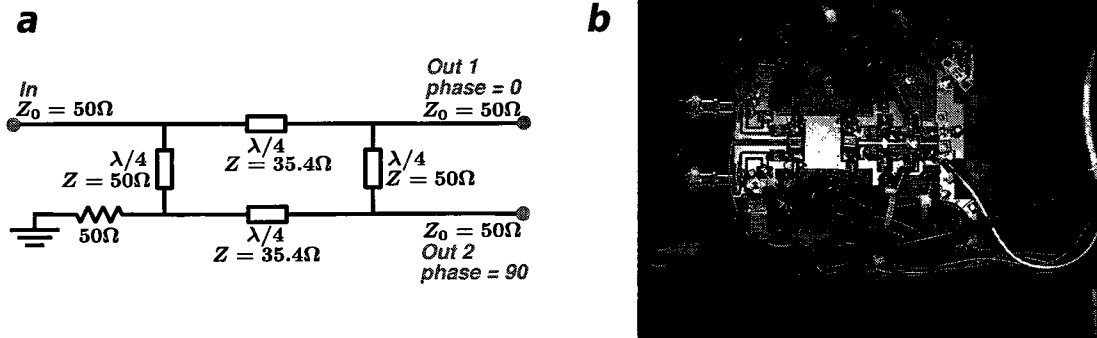


Figure 3-16: Quadrature hybrid. A schematic shows the circuit (a). A photo shows the practical realization of the hybrid with coaxial cables as the $\lambda/4$ -transmission lines (b). The hybrid is switched between transmit and receive states using PIN diodes.

The PIN diode logic, switching coils on and off depending on transmit or receive phase in the pulse sequence is realized using so called “coil files” which are read by the scanner software to apply appropriate PIN diode switching during the pulse sequence.

The finished HXe human chest coil with 32-channel phased-array receive and integrated asymmetric birdcage transmit coil is shown in Fig. 3-17.

3.4 Results

3.4.1 Receive Array

Coil Characteristics

The unloaded quality factor (Q) of a single wire surface coil was 400. The Q -ratio, i.e. the ratio of unloaded to loaded Q was 5.75 (Table 3.1). Matching was determined by measuring the reflection on the output cable and was adjusted to (-20) - (-30) dB under loaded conditions. After the receiver

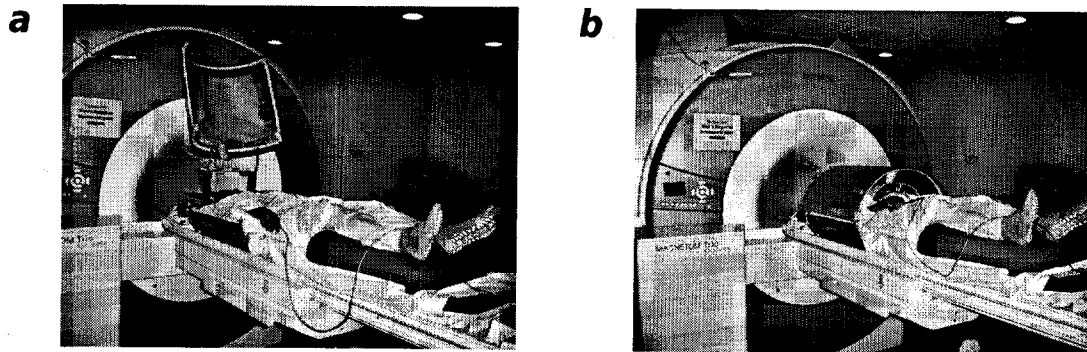


Figure 3-17: The finished chest coil with volunteer at the MRI scanner. The coil is placed on the patient bed. A hinge mechanism allows the bottom part of birdcage and array to open for easy patient access (a). In the closed position, the coil is ready to be moved inside the magnet bore (b).

coils were assembled in the array, spatial overlap decoupling between next neighbors was adjusted with a result of less than -12 dB coupling for each pair. The method of preamplifier decoupling further improved the decoupling to better than -35 db. An example of preamplifier decoupling as measured using the decoupled probe, is shown in Fig. 3-18.

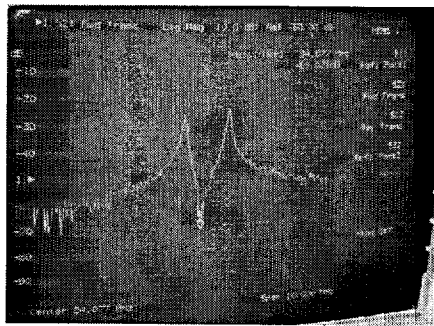


Figure 3-18: Example of preamplifier decoupling measured using the decoupled probe and an S21 measurement. Even though the method is conceptually the same (a parallel resonant circuit to obtain high impedance in coil), the peaks in preamplifier decoupling typically are narrower than during active detuning (not shown).

Noise Coefficient Matrix

After the coil wires and plugs are assembled, the decoupling between individual elements can be measured by collecting noise statistics using the MRI scanner. In order to obtain a most realistic measurement, the data were collected while a volunteer was lying in the coil (loading changes coupling). The correlation between receiver elements is assessed by calculating the noise correlation coefficient matrix (Fig. 3-19). The noise correlation matrix C with elements $c_{i,j}$ is the inner product of the noise signal time series measured in coil i with the noise signal measured in coil j [130]:

$$c_{i,j} = \frac{1}{N-1} \mathbf{n}_i \mathbf{n}_j^H \quad (3.10)$$

where the N is the number of noise samples acquired and \mathbf{n} is a row vector containing the noise time series. Subtracting the mean and normalizing by the square root of noise variances σ yields the correlation coefficient matrix:

$$r_{i,j} = \frac{\mathbf{n}_i \mathbf{n}_j^H - a_i a_j^* N}{\sigma_i \sigma_j} \quad (3.11)$$

The correlation coefficient is also known as Pearson's r statistic. The rows and columns of the matrix \mathbf{r} correspond to the receiver channel number. The matrix entries correspond to a relative measure of receive channel coupling. The diagonal elements are equal to 1, since by definition any signal is perfectly correlated with itself.

Root-Sum-of-Squares Compared to Adaptive-Combine Image Reconstruction

Ideally the 32-channel array elements would receive signals independently from each other, which can be reconstructed to an image covering a region corresponding to the localized sensitivity profile of the surface coil element. Individually reconstructed images are shown in Fig. 3-20. In order to obtain the combined image covering the total FOV seen by the array coil, the individual images have

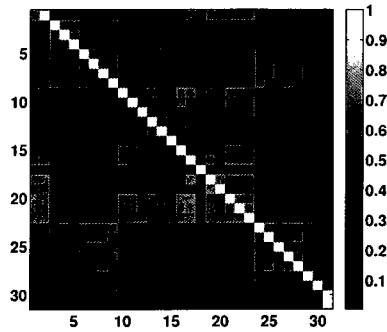


Figure 3-19: Noise correlation coefficient matrix. The rows and columns correspond to the receiver channel number. The intensity of the image pixel corresponds to the coupling between respective channels. Here the mean over all channels = 0.25.

to be combined. This can be achieved either via a simple root-sum-of-squares addition or using a method called “adaptive-combine” which takes into account the correlation between the channels in order to optimize SNR. Figure 3-21 shows on the example of two different image slices with different SNR ⁶, that the adaptive combine reconstruction improved SNR in the good SNR posterior slice, whereas in the center slice with very low SNR the appearance of the noise pattern is modified.

3.4.2 Transmit Asymmetric Birdcage

Coil Characteristics

Measured on the bench the unloaded Q of the asymmetric birdcage vertical mode was 220 and for the horizontal mode 140. Measured inside the scanner (with the scanner bore shield in place) the Q decreased only slightly to 205 for the vertical mode and 130 for the horizontal mode. These results are comparable to the results obtained by De Zanche et al for their asymmetric HHe birdcage coil (vertical mode Q = 220, horizontal mode Q = 120 [126]). The Q ratio of our birdcage was approximately 2. On the bench the two resonant modes were tuned to 30 MHz since sliding the birdcage into the scanner bore shifted the frequency up to the HXe resonance of 34 MHz. Inserting

⁶SNR in the center slice is lower due to the sensitivity drop off with distance away from the receiver surface coil.

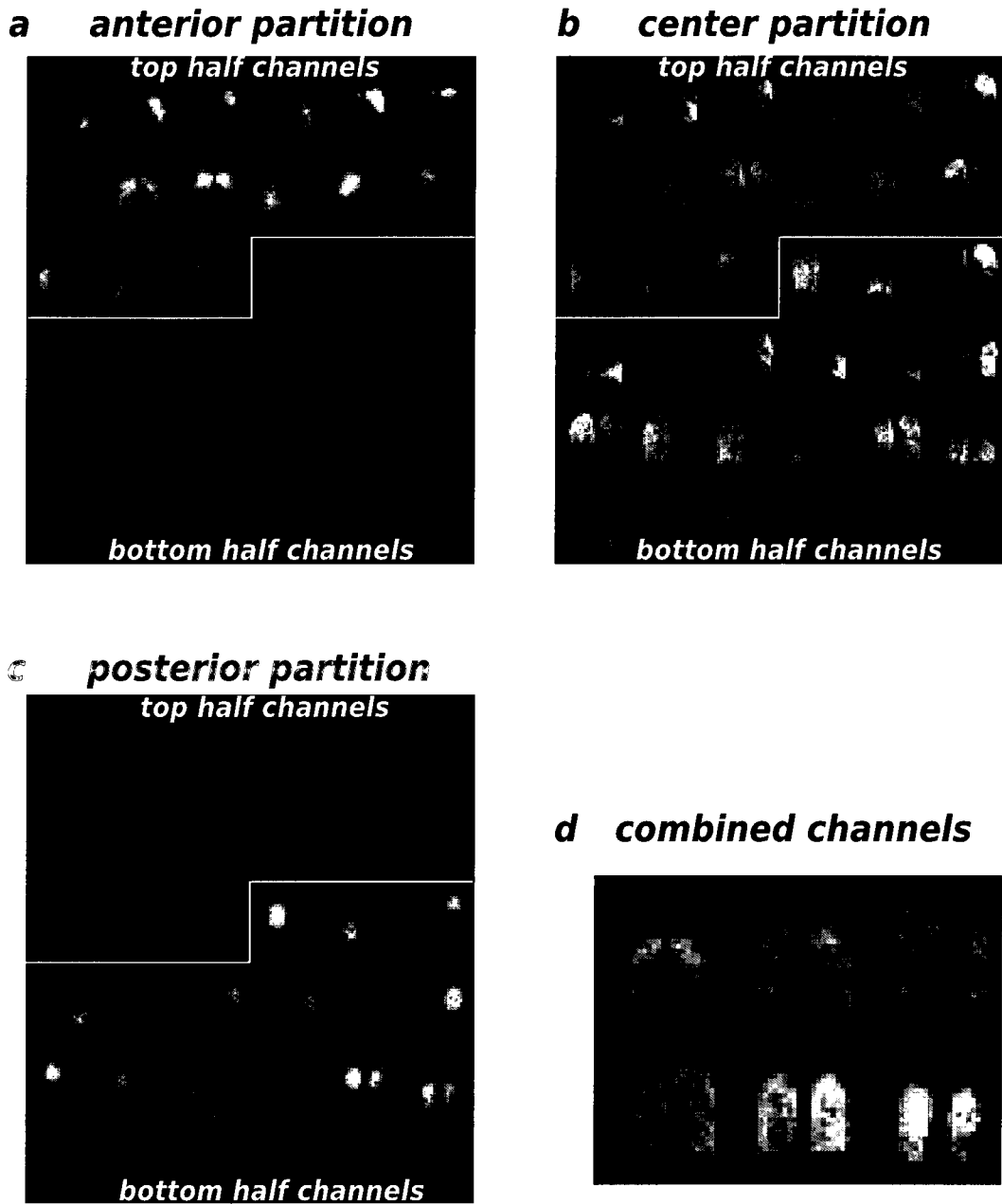


Figure 3-20: Images reconstructed in uncombined receiver channels. This is an example to illustrate the localized sensitivity profiles of the individual receivers. From this point on the combined image can be obtained using either a simple sum of squares addition or the more advanced adaptive-combine reconstruction which takes into account the noise correlation between channels in order to optimize SNR. The surface coil receivers have only limited depth sensitivity which is illustrated by high (low) signals in top (bottom) half channels in the anterior image partition which is close to the top half (a) and vice versa in the posterior image partition (c) while the center slice shows approximately equal SNR for top and bottom half channels (at equal distance from both array halves) (b).

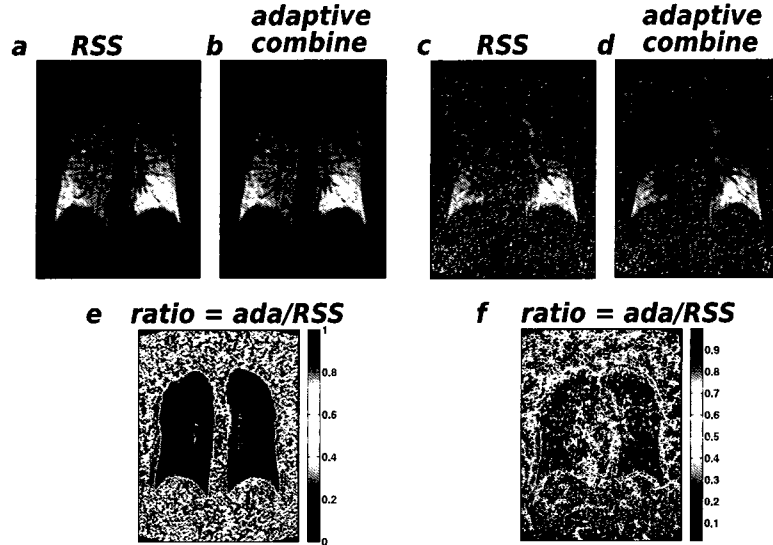


Figure 3-21: Root-sum-of-squares (RSS) compared to adaptive-combine image reconstruction. Note that in the 2D multi-slice acquisition with generally low SNR, the posterior slice (a,b) has better SNR than the center slice (c,d) due to the array surface coil sensitivity profile. Adaptive combine reconstruction (b) is able to remove streaking artifacts visible in RSS reconstruction (a), while in the low SNR center slice adaptive combine (d) changes the noise pattern around the borders of the lung. Ratio of adaptive combine and RSS reconstruction shows improvement in SNR for the posterior slice adaptive combine reconstruction (e) but no general improvement is apparent in the low SNR center slice (f).

the array into the birdcage decreased the efficiency of the birdcage by approximately 15%. Final measurements inside the scanner bore, with the actively detuned array in place and with a human volunteer loading the coil yielded for the two birdcage resonant modes a reflection of -20 dB and -12 dB at the 34.08 MHz (S11 measurement), while the decoupling (transmission) between the two modes was -12 dB (S12 measurement).

Transmit Homogeneity

In order to assess the performance of the coil regarding the transmit homogeneity, B_1 maps were acquired (Fig. 3-22). The pulse sequence used to obtain B_1 maps collected two 3D FLASH acquisitions during a breath hold. Each RF excitation pulse reduces the non-equilibrium longitudinal magnetization M_0 to $M_0 \cdot (1 - \cos \alpha)$, where α is the excitation flip angle. Thus, the ratio of two

identical image acquisitions I_1 and I_2 yields a B_1 map, characterizing the regional flip angle distribution:

$$\alpha = \arccos \left[\left(\frac{I_2}{I_1} \right)^{1/N} \right] \quad (3.12)$$

Here N corresponds to the number of RF excitations between k-space centers of I_1 and I_2 .

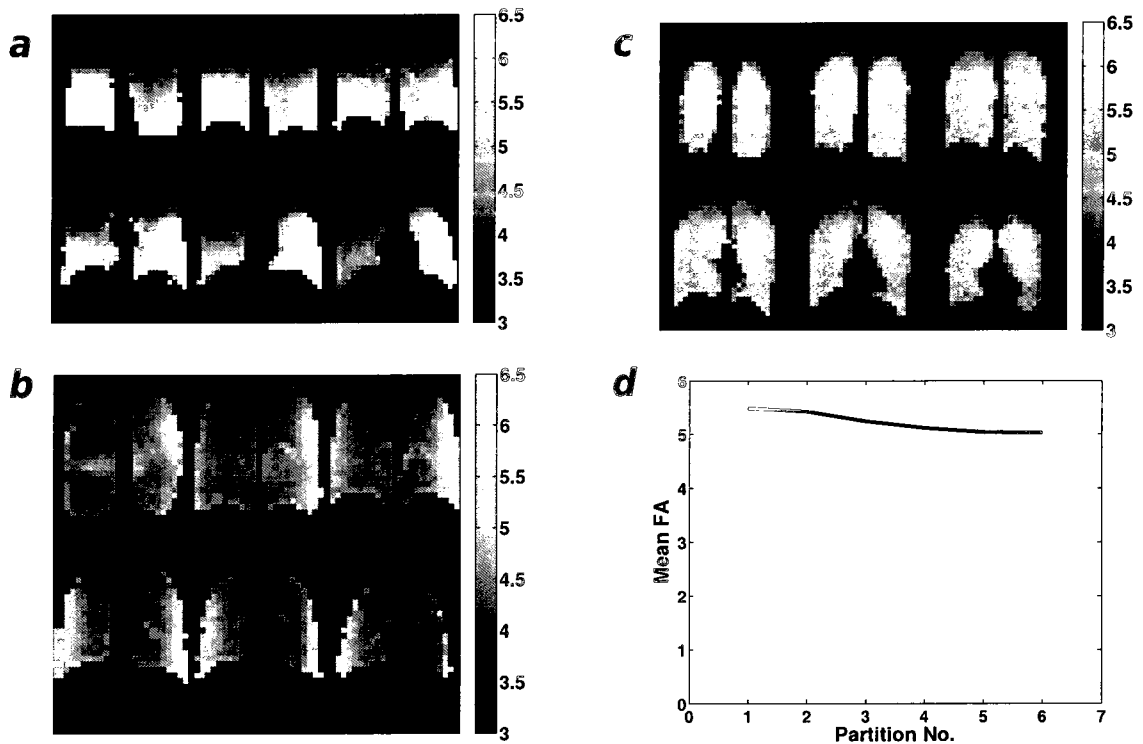


Figure 3-22: B_1 map for the birdcage transmit coil and for comparison two other T/R coils. For a T/R wrap coil (a), flip angle mean (std) = $5.4^\circ \pm 1.3^\circ$ and ratio std/mean = 0.24, for a larger vest coil (b), flip angle mean (std) = $4.4^\circ \pm 0.6^\circ$ and ratio std/mean = 0.14. The birdcage transmit coil (c) has a significantly improved transmit field homogeneity, with flip angle mean (std) = $5.2^\circ \pm 0.4^\circ$ and ratio std/mean = 0.08. Plotting the mean flip angle for each partition as a function of partition number (d), a gradient with higher flip angles in the posterior partitions was found. The total difference (anterior-posterior) was $\approx 10\%$.

3.4.3 Spin Density Imaging in Healthy Subjects and Subjects with Lung Disease

Spin density images were acquired using the new human chest coil. The superior sensitivity of the array coil is demonstrated by the excellent image quality of the high resolution images (2.1 mm in plane resolution) (Fig. 3-23). Images were accelerated by a factor 2 and reconstructed using the GRAPPA algorithm [116]. No remaining fold-over artifacts were observed. In high resolution ventilation images of subjects with lung disease (asthma, Fig. 3-24 and COPD, Fig. 3-25) ventilation defects were clearly characterized. Acceleration factors up to 6 (3x2) were feasible as demonstrated in a 3D-TrueFISP acquisition⁷ in a healthy subject (Fig. 3-26). The acceleration enabled by the 32-channel receive array reduced the total acquisition time from 8 s to only 2 s. The parallel imaging performance of the array was further demonstrated in a spiral acquisition, where a (simulated) reconstruction using only 4 out of the fully sampled 11 spiral interleaves achieved comparable image quality (Fig. 3-27). The reconstruction using only 4 interleaves was performed by discarding 7 spiral k-space trajectories in order to simulate an accelerated acquisition. The reconstruction algorithm incorporated Principal Component Analysis (PCA)-based channel compression before the parallel image reconstruction. Using a 5% tolerance, the algorithm used 14 (out of 31) virtual coils, which is a relatively high ratio indicating that the individual channels are fairly independent [131].

3.5 Discussion and Conclusions

Challenges in hyperpolarized gas imaging arise from the non-equilibrium state of the longitudinal magnetization available for image encoding. Each RF excitation will inevitably destroy a fraction of the available magnetization. Further, for most applications image acquisition has to be performed during a single breath hold thus limiting the total time available for image encoding and additional

⁷TrueFISP is the SIEMENS acronym for a steady-state-free-precession pulse sequence which is characterized by superior SNR due to its use of alternating RF flips (+/- α) which preserve longitudinal magnetization during the course of imaging.

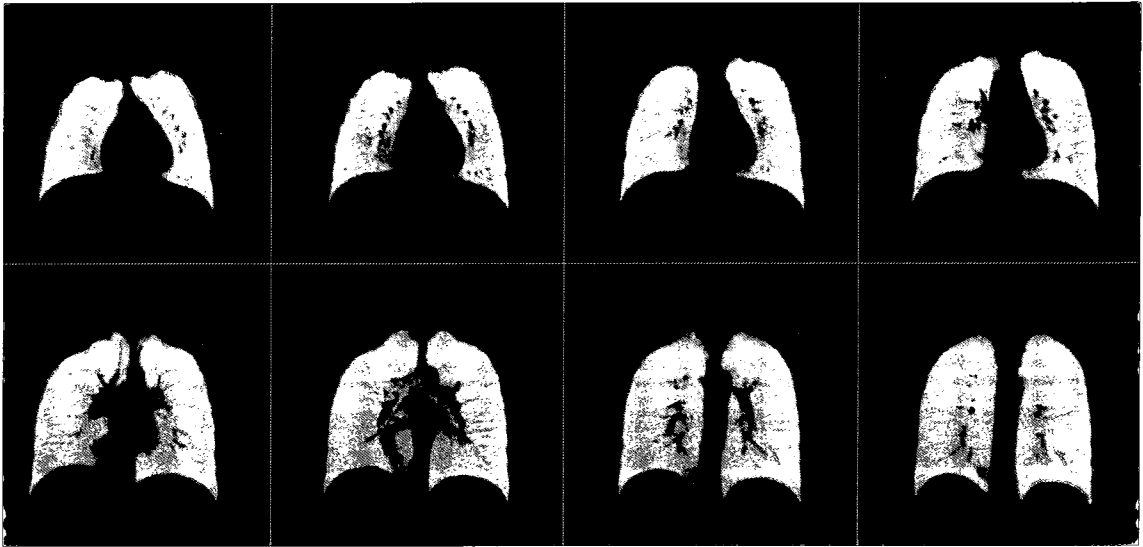


Figure 3-23: Ventilation scan from a healthy volunteer using the 32-channel coil. Image acquisition was a 2D FLASH sequence, with resolution $2.1 \times 2.1 \times 10 \text{ mm}^3$, acceleration factor 2.

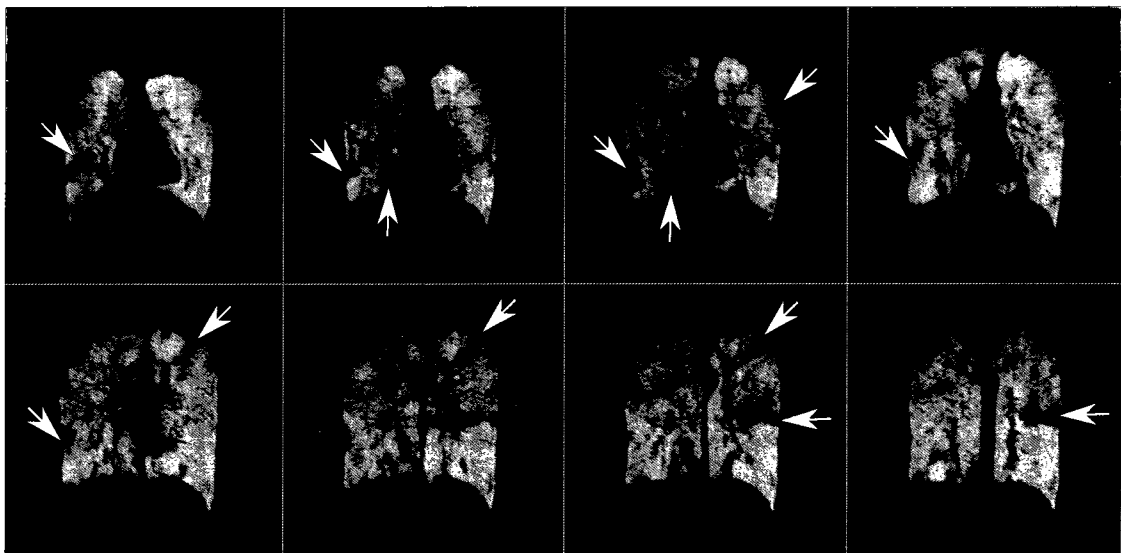


Figure 3-24: Ventilation scan from an asthmatic patient using the 32-channel coil. Image acquisition was a 2D spiral sequence, with resolution $1.6 \times 1.6 \times 10 \text{ mm}^3$. White arrows indicate ventilation defects.

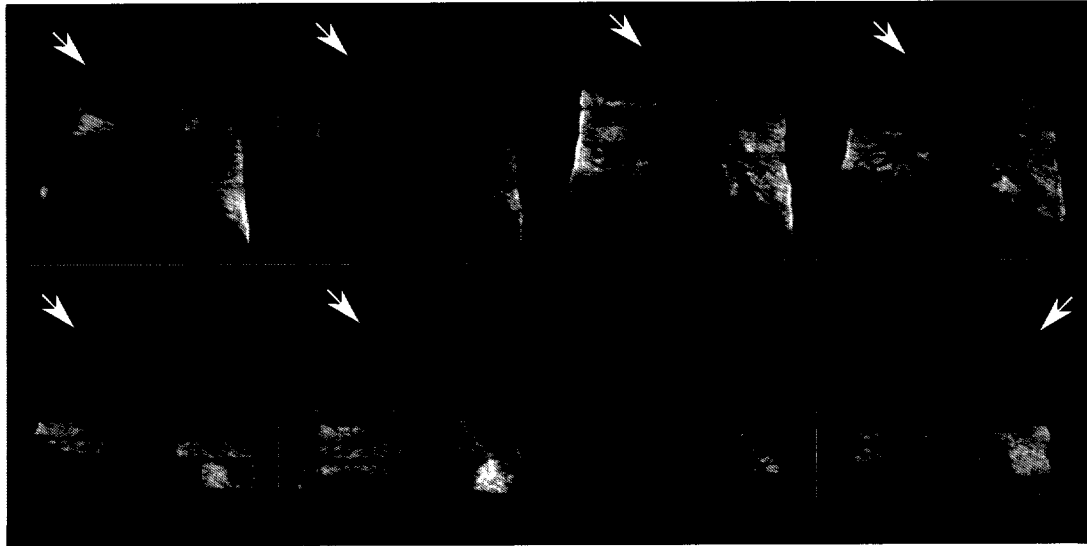
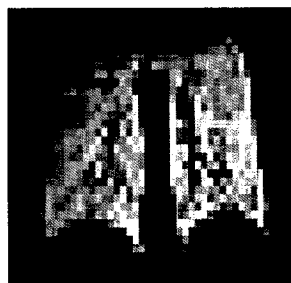


Figure 3-25: Ventilation scan from a COPD patient using the 32-channel coil. Image acquisition was a 2D FLASH sequence, with resolution $3.3 \times 3.3 \times 15 \text{ mm}^3$, acceleration factor 3. White arrows indicate right upper lobe which is poorly ventilated.

a fully sampled



b accelerated 3x2

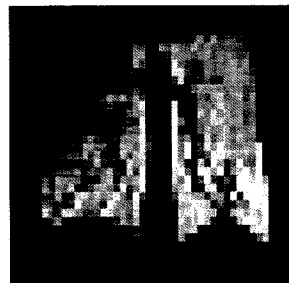


Figure 3-26: TrueFISP 3D spin density acquisition fully sampled and accelerated in 2D by $R=3 \times 2$. The acceleration reduced the total 3D acquisition time from 8s to 2s. GRAPPA image reconstruction using coil sensitivity information was able to remove aliasing artifacts from the undersampled acquisition. Image quality of the accelerated acquisition is comparable to the fully sampled acquisition.

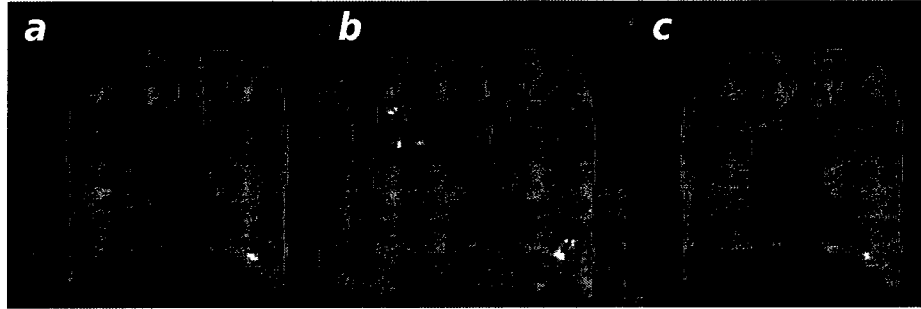


Figure 3-27: Spiral acquisition of asthmatic subject with simulated parallel reconstruction. a) fully sampled reconstruction b) undersampled reconstruction using only 4 out of 11 spiral interleaves c) parallel image reconstruction using only 4 out of 11 spiral interleaves. Parallel image reconstruction (c) clearly improves image quality if compared to conventional reconstruction (b) using the same undersampled spiral data set.

contrast generation in functional imaging applications. Parallel imaging enables accelerated image acquisitions using phased-array receive coils. Whereas reducing the number of acquired samples results in an SNR penalty in proton applications this is not the case in hyperpolarized imaging, since the penalty for SNR due to the decreased noise sampling is compensated by an SNR boost if an optimum flip angle is used for the reduced number of RF excitations. In this work, we designed, built and evaluated a 32-channel phased-array receive coil with an integrated asymmetric birdcage transmit coil for HXe imaging at 3T.

The receive array enabled highly accelerated image acquisitions, up to factor 6 in 3D acquisitions which reduced the total scan time in this case from 8 s to only 2 s. This is important, since for functional imaging applications, such as pO₂, ADC and XTC multiple image acquisitions are required within a single breath hold. With recent improvements in gas hyperpolarization levels [29] [132], higher SNR allows for better image resolution which may lengthen the required breath hold time beyond the capability of patients. Therefore, parallel imaging enabled using an array coil as presented in this work, is a necessary step in order to continue improving hyperpolarized gas imaging applications. To even further reduce acquisition times recently demonstrated non-linear image reconstruction algorithms such as compressed sensing [120] can be combined with parallel imaging

in future studies. Unlike for proton applications, this can be pushed to the limit in hyperpolarized applications, since no SNR penalty arises from undersampling. In fact a phased-array coil actually provides improvements in SNR compared to previously used volume T/R coils. This has two reasons. First, the receiver surface coil intensity profile provides increased SNR especially in anterior and posterior image slices (close to the coil). Second, parallel imaging reduces the acquisition time and thus decreases magnetization decay due to longitudinal relaxation. To our knowledge, image resolutions as shown for a healthy volunteer in this work were never before achieved in the field of HXe MRI (in-plane resolution 2.1 mm).

Regarding channel coupling, the noise correlation between receivers was found to be relatively high in our array (mean coupling 25%, whereas Meise et al measured a mean of 9% [122]). The reason for this is most likely that overlap decoupling between neighboring channels is more difficult to implement in practice using wire coils compared to a circuit board array layout as in [122]. However as shown by Roemer et al [111], channel coupling can be compensated for by using image reconstruction algorithms which involve channel correlation information. This was also confirmed experimentally in this work by comparing RSS to adaptive combine reconstruction which improved SNR.

The integrated asymmetric transmit coil provided excellent field homogeneity (8% variation across the total FOV) superior to more commonly used wrap-coil or Helmholtz designs. This is important, since a homogeneous image excitation makes most efficient use of the non-equilibrium magnetization by avoiding to deplete the signal non-uniformly regionally. Further, transmit homogeneity is important for unbiased contrast generation in functional imaging. If the flip angle is non-uniform throughout the FOV, it is uncertain if variations in the obtained contrast map resulted from physiological variations (as desired) or from the incomplete contrast encoding due to a regional variation in the flip angle.

A limitation of this coil design is that, because the birdcage has to be relatively large in order to

accommodate the array coil, the filling factor (ratio of sample volume to coil volume) is lower than for traditional volume coils which are used for both, transmit and receive and can be placed tight around the sample. The lower filling factor η of the integrated design results in reduced efficiency. The sensitivity (or efficiency) of an NMR probe ($B_1/(I_0\sqrt{r})$) is proportional to the generated B_1 amplitude per applied current (Eqs. 2.14 and 2.16) and noise resistance \sqrt{r} . Therefore the sensitivity is proportional to $\sqrt{\eta Q}$, since the quality factor $Q = \frac{L\omega}{r}$. An additional factor to be taken into account is that the presence of the array within the volume of the transmit coil decreases its efficiency. The oscillating transmit B_1 field induces eddy currents in electrically conducting components of the array, thus dissipating energy. Efficiency of the transmit coil is important, since the RF power amplifier provided by the Siemens MRI system for multi-nuclear applications only supplies up to 8 kW of transmit power, whereas this is less of an issue in proton applications since the proton amplifier supplies up to 32 kW. Further, the lower gyromagnetic ratio of HXe compared to 1H (or HHe), requires that in order to achieve the same flip angle the transmit power must be approximately a factor 7 higher. A practical measure of transmit efficiency is the reference voltage, which is defined as the voltage required by the MRI scanner in order to achieve a 180° flip using a 1 ms rectangular RF pulse. The reference voltage for the proton body coil integrated into the Siemens 3T MRI scanner is approximately 400 V. The reference for our custom designed xenon transmit birdcage coil is approximately 1100 V. This seems large however considering that the reference voltage is proportional to $1/\sqrt{\gamma}$ the reference voltage for an equally sensitive HXe coil is expected to be approximately a factor two larger:

$$\frac{U_{Xe-129}}{U_{H-1}} \propto \sqrt{\frac{\gamma_{H-1}}{\gamma_{Xe-129}}} = \sqrt{\frac{42.6\text{MHz/T}}{11.7\text{MHz/T}}} \approx 2 \quad (3.13)$$

These efficiency considerations can be a limitation for pulse sequence design. In most applications short pulses are desired (to keep TE short which minimizes SNR loss). The relatively low transmit coil efficiency, caused by low filling factor and array loading, is a disadvantage of this

coil design. In the future however issues related to transmit efficiency can be easily resolved by implementing a more powerful RF power amplifier for multi-nuclear applications.

In conclusion, the 32-channel phased-array receive coil enables highly accelerated image acquisitions. The ability of faster image acquisition can be used to acquire higher resolution images or for contrast encoding in functional imaging applications or simply to reduce the time required for breath holding in existing imaging protocols. The integrated asymmetric transmit birdcage coil showed good B_1 field homogeneity which is crucial in order to make efficient use of magnetization throughout the whole imaging FOV as well as for unbiased contrast generation in functional image applications. Even though similar implementations of the two coil designs were presented separately before in the field of HHe MRI ([122], [126]), the combination of a 32-channel phased-array with an asymmetric birdcage, to our knowledge, represents the first of its kind.

CHAPTER 4

HYPERPOLARIZED ^{129}Xe

GAS-EXCHANGE IMAGING OF LUNG

MICROSTRUCTURE

4.1 Introduction

Today, the clinical diagnosis for most lung diseases relies primarily on clinical history and global assessment of lung function provided by pulmonary function tests (PFTs). A global assessment of lung function as in PFTs however has only limited sensitivity and potential to differentiate disease phenotypes. Imaging of lung structure using computed tomography (CT) is a clinically used adjunct for the diagnosis of certain lung diseases. Image contrast in CT is based on lung tissue density and state-of-the-art scanners at best achieve resolutions on the mm-scale. Furthermore, the significant radiation dose for the subject associated with high resolution CT limits frequent use.

There currently exists no method for measuring regional gas exchange within the lung, and early diagnosis, phenotyping and monitoring of lung disease would greatly benefit from such a tool. The main physiological function of the lung is the exchange of respiratory gases from the alveolar air spaces, through the respiratory epithelium and capillary endothelium, into the blood. The size of relevant structures is on the micrometer scale [36], far below the resolution limit of current in vivo diagnostic imaging modalities.

The development of hyperpolarization methods for ^{129}Xe [133] led to its use as an inhaled contrast agent for MRI [3]. Upon inhalation, hyperpolarized ^{129}Xe (HXe) follows the functional pathway of gas exchange in the lung by diffusing from alveolar air spaces into alveolar septa, a structure 5-8 microns thick consisting of blood and tissue regions [36]. HXe atoms dissolved in lung tissues exhibit a large chemical shift (~ 200 ppm) relative to their gas-phase resonance frequency [15] (Fig. 4-1), which enables image acquisition methods to distinguish gas- and dissolved-phase xenon [5] [17] [64], and permits imaging of lung function such as gas exchange [23] [26] [27] [28] and alveolar-capillary gas uptake [18] [25] [134]. Through modeling of xenon diffusion, physiologically important microstructure parameters, such as parenchymal tissue-to-alveolar-volume ratio [26] [27] [28] [23], surface-to-volume ratio [23] and blood-gas barrier thickness [21], can be determined. However, the latter two have only been demonstrated in whole-lung spectroscopy experiments. The reasons for this are two-fold. First, due to the low partition coefficient ($\lambda=0.1$ [14]), the dissolved-phase xenon magnetization is much less than ($\sim 2\%$) the gas-phase magnetization. Second, in order to extract the wall thickness or surface-to-volume ratio, the xenon diffusion process has to be encoded at multiple time points. Imaging at multiple time points is fundamentally limited by SNR, since the magnetization of HXe is in a non-equilibrium state and is continuously depleted during image encoding. Furthermore, HXe acquisitions in humans are usually performed during breath holding and multiple encodings proportionately lengthen the acquisition time.

The xenon polarization transfer contrast (XTC) MR method pioneered by Ruppert and colleagues [26] [27] [28] overcomes the difficulty of imaging xenon in the dissolved phase by encoding xenon exchange information into the relatively large gas-phase signal. In this study, we implemented XTC MRI in four dimensions by extending the original single-exchange-time 2D-projection acquisition to a 3D acquisition that characterizes the gas-exchange process for multiple delay times. We call this method multiple exchange time xenon polarization transfer contrast, or MXTC [135] [136] [137] [138] [139].

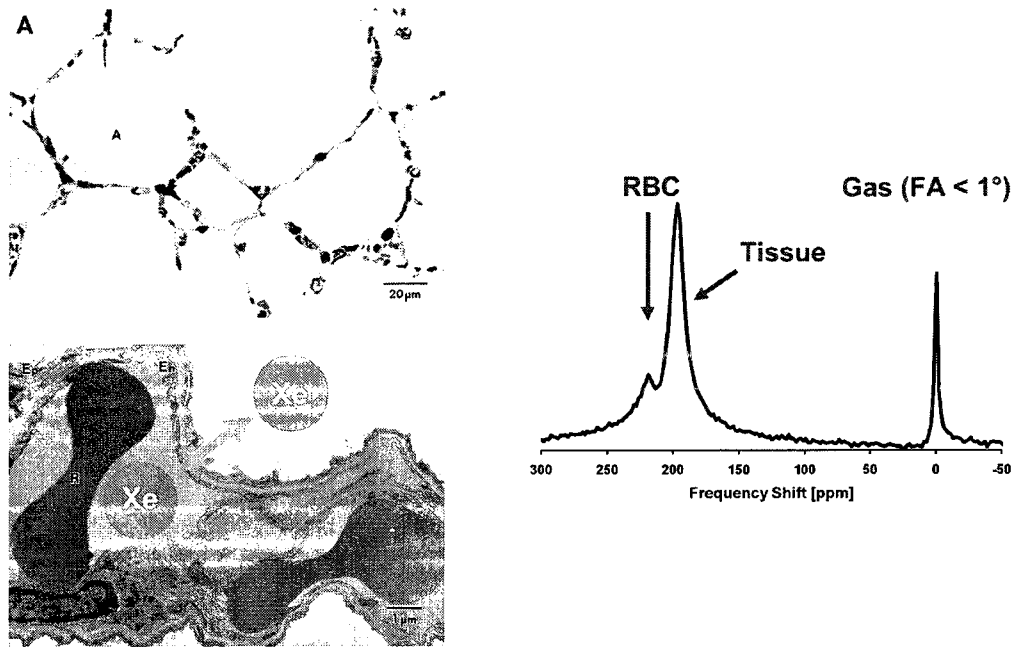


Figure 4-1: ^{129}Xe dissolved in tissue. A micrograph of the lung parenchyma is shown (where A indicates an alveolus) as well as a cartoon of a HXe atom exchanging between septum and alveolus. Dissolved-phase xenon experiences a chemical shift of approximately 200 ppm compared to its gas-phase resonance frequency. Note that the resonances in the spectrum are scaled according to the applied flip angle, which is $\sim 90^\circ$ on the dissolved-phase resonance and $< 1^\circ$ on the gas-phase resonance. Courtesy of K. Ruppert.

By collecting data at multiple delay times, MXTC enables regional mapping of two lung-function parameters: 1) MXTC-F, the long exchange-time depolarization value, which is proportional to the ratio of functional tissue-to-alveolar-volume and 2) MXTC-S, the square root of the xenon gas-exchange time constant, which is proportional to the ratio of septal wall thickness and the square root of xenon membrane diffusivity. Only structures in the lung parenchyma that are actively involved in the gas-exchange process contribute to image contrast. This makes the technique specifically sensitive to disease-induced alterations of lung microstructure that compromise gas exchange.

The goal of this study was to develop the MXTC technique and assess the potential utility of MXTC to detect disease-induced alterations of functional lung microstructure. We describe preliminary findings of MXTC parameter mapping in healthy subjects and subjects with COPD or asthma.

For two COPD subjects, we also compared the results for MXTC-F, the functional tissue-density parameter, with HXe apparent diffusion coefficient (ADC) imaging, which probes alveolar size and with direct dissolved-phase imaging. Further, for one of the COPD subjects, we also compared MXTC-F to CT imaging, the current gold standard to depict tissue destruction from emphysema.

4.2 Background

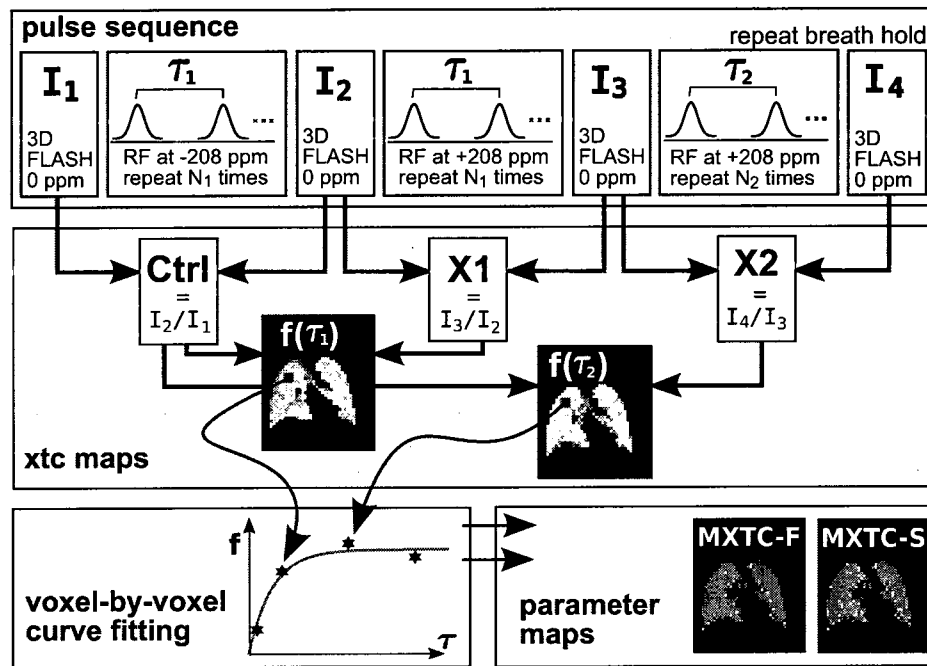


Figure 4-2: A schematic showing image acquisition and data analysis workflow. Four 3D-FLASH images (I_i) were acquired during a single breath hold, separated by a series of Gaussian saturation pulses centered at the dissolved phase at +208 ppm (XTC contrast $X1$ and $X2$) or at -208 ppm (control contrast $Ctrl$ for T1-normalization). From the image ratios, which were normalized by the control contrast and corrected for different flip angles in respective 3D-FLASH acquisition, depolarization maps ($f(\tau)$) were calculated, which reflect the xenon gas-phase magnetization decay due to xenon exchange occurring during a characteristic delay time τ . In two to four breath holds, four to eight depolarization maps were obtained. Curve fitting yielded two parameters for each imaging voxel: the depolarization value for infinite delay times (MXTC-F) and the square root of the time constant of the xenon exchange (MXTC-S). The fitting parameters are proportional to tissue-to-alveolar-volume ratio and mean septal wall thickness.

A schematic of the MXTC pulse sequence is shown in Fig. 4-2. Conceptually, it is based on

a single breath-hold implementation of XTC (for details, see ref. [23] [26] [27] [28]). However, for the MXTC implementation, four 3D-FLASH image sets of gas-phase HXe are acquired (labeled I_1 , I_2 , I_3 and I_4), rather than three 2D-projection images as in ref. [23]. These image sets are separated by a series of frequency-selective saturation pulses, centered either at -208 ppm relative to the gas phase for control contrast (applied between I_1 and I_2) or at +208 ppm to affect ^{129}Xe dissolved in blood and parenchymal tissue, and create XTC contrast (applied between I_2 and I_3 for the first XTC contrast of the image set, and between I_3 and I_4 for the second XTC contrast of the image set). After each saturation pulse during the XTC contrast-generation periods, the longitudinal magnetization in the dissolved phase is (ideally) destroyed. During the selected delay time τ between saturation pulses, HXe atoms in the gas-phase exchange with xenon atoms in the dissolved phase, whose longitudinal magnetization is much lower (ideally zero). This results in a net decay of xenon magnetization in the gas phase. Repetition of this process results in a measurable reduction of gas-phase magnetization, creating XTC contrast. The control acquisition reflects all other contributions to the gas-phase signal decay (e.g., T1 and HXe removal by the blood stream) and is used for normalization purposes.

The sequence parameters for all four 3D acquisitions (I_i) are identical except for the excitation flip angle, which is increased for acquisitions I_3 and I_4 to maintain an adequate signal-to-noise ratio (SNR). In the following, only the analysis of the first XTC acquisition using I_2 and I_3 is described. The analysis based on I_3 and I_4 is performed in an analogous fashion. For acquisitions I_2 and I_3 , the gas-phase depolarization per saturation pulse (f_τ) for a given delay time τ is calculated by normalizing the contrast ratio (I_3/I_2) with the control ratio (I_2/I_1) and accounting for the different excitation flip angles in the respective image acquisitions ($\alpha_1, \alpha_2, \alpha_3$):

$$f_\tau = 1 - \left(\frac{I_3 I_1}{I_2^2} \cdot \frac{(\sin \alpha_2)^2 (\cos \alpha_1)^{N-K}}{\sin \alpha_3 \sin \alpha_1 (\cos \alpha_2)^{N-2K} (\cos \alpha_3)^K} \right)^{1/N_p} \quad (4.1)$$

where I_i represents the signal intensities in the i th FLASH image set, N_p is the total number of

saturation pulses, N is the total number of image excitation pulses, and K is the number of image excitations before reaching the center of k-space.

For MXTC, depolarization maps (f_τ) are acquired at several different delay times. The process of xenon exchange as a function of delay time can be modeled using the solution to the differential equation of Ficks second law of diffusion with Dirichlet boundary conditions. Thus, the magnetization loss in the gas phase due to xenon exchange after a 90° saturation RF pulse centered at the dissolved-phase region is given by [27]:

$$f_\tau = F_{max} \left(1 - \sum_{n=1}^{\infty} \frac{8}{((2n-1)\pi)^2} e^{-D_m \left(\frac{(2n-1)\pi}{L_i} \right)^2 \tau} \right) \quad (4.2)$$

where F_{max} is the gas-phase depolarization for an infinitely long delay time and corresponds to the measurement parameter MXTC-F, D_m (0.33×10^{-5} cm²/s [27]) is the xenon diffusion constant in the septal wall, and L_i is the average functional septal wall thickness. At technically feasible delay times (> 5 ms), keeping only the first term in the infinite series is a good approximation:

$$f(\tau) = F_{max} \left(1 - \frac{8}{\pi^2} e^{-\frac{\tau}{\tau_c}} \right) \quad (4.3)$$

where τ_c is the exchange-time constant with which the saturated dissolved-phase magnetization is replenished:

$$\tau_c = \frac{L_i^2}{D_m \pi^2} \quad (4.4)$$

Fitting of the measured gas-phase depolarization to Eq. 4.3 permits extraction of the maximum depolarization value MXTC-F and the exchange-time constant τ_c . At long delay times, all xenon atoms saturated in the dissolved phase exchange with the gas phase and thus the depolarization ratio (F_{max}) divided by the partition coefficient (Ostwald solubility $\lambda=0.1$ [14]) yields the tissue-to-alveolar-volume ratio:

$$\frac{V_{\bar{i}}}{V_a} = \frac{F_{max}}{\lambda} \quad (4.5)$$

$V_{\bar{i}}$ is the functional parenchymal tissue volume and V_a is the alveolar gas volume. Note that MXTC-derived parameters refer to the functional subset of structures in the lung parenchyma that are directly involved in the gas exchange. We therefore use $V_{\bar{i}}$, in order to distinguish it from the purely structural definition of parenchymal tissue volume V_i defined in the field of ex-vivo histology. Using the second fitting parameter, MXTC-S ($\text{MXTC-S} = \sqrt{\tau_c}$), and Eq. 4.4, the average functional septal wall thickness $L_{\bar{i}}$ can be calculated as:

$$L_{\bar{i}} = \sqrt{\tau_c D_m} \cdot \pi \quad (4.6)$$

Since, in this study, MXTC was implemented with a non-selective saturation of the dissolved-phase magnetization, no distinction is made between red blood cell and tissue compartments within the parenchyma. Therefore the functional wall thickness refers to the entire septal wall.

4.3 Materials and Methods

4.3.1 General Study Protocol

General Study Protocol for Rabbits

All animal protocols were approved by the University of Virginia Institutional Animal Care and Use Committee. Animal experiments were performed with four New Zealand rabbits (R1-R4) weighing approximately 5 kg. The rabbits were anesthetized with a mixture of Xylazine 5 mg/kg and Ketamine 50 mg/kg. The animals were then intubated with an endotracheal tube and placed in a custom-made ^{129}Xe transmit/receive birdcage RF coil (IGC Medical Advances, Milwaukee, WI). At the beginning of each experiment, 20 ml or 40 ml of hyperpolarized ^{129}Xe were dispensed from a

large Tedlar bag into a plastic syringe, which was used to ventilate rabbits starting at end-expiratory volume. The valve connecting the endotracheal tube to the syringe was closed for the duration of the experiment (~ 10-15 s). Animal studies were conducted on a 1.5-Tesla commercial whole-body scanner (Avanto, Siemens Medical Solutions, Malvern, PA), modified by the addition of a broadband amplifier.

General Study Protocol for Human Subjects

For this preliminary study, four healthy, non-smoking subjects (H1-H4), two subjects with COPD (C1, C2) and one with asthma (A1) (Table 4.1) were recruited. All studies were performed under a Physician's IND for imaging with HXe using a protocol approved by our Institutional Review Board. Before each imaging procedure, written informed consent was obtained from the subject after the nature of the procedure had been fully explained. Spirometry and an electrocardiogram were performed immediately before and after the imaging session (Table 4.1). Oxygen saturation levels and heart rate were monitored throughout the experiment. Before the subject was placed in the RF coil, a test dose of xenon was administered. All subjects tolerated the test dose well although some had mild central nervous system effects such as mild transient numbness or tingling, and alterations in affect.

The total volume of generated HXe was distributed in 500 ml Tedlar bags allowing for up to four breath hold experiments. Gas mixtures given to human subjects for each breath hold consisted of 500 ml HXe, 150 ml oxygen and 100 ml room air. The oxygen and room air mixture was contained in a second 500 ml Tedlar bag, which was connected with the HXe bag by a Y-connector. The subjects would inhale the gases from both bags simultaneously, ensuring a minimum concentration of 21% oxygen in the lung. The subjects were asked to breath in the mixture starting at residual lung volume (RV). One healthy subject (H3) was additionally imaged at total lung capacity (TLC) by breathing in additional room air after the xenon-oxygen-air mixture was administered. Imaging

studies for human subjects were conducted on a whole-body 3T MRI system (TIM Trio, Siemens Medical Solutions, Malvern, PA), modified by the addition of a broadband amplifier. A custom made 32-channel receive array coil with integrated asymmetric birdcage transmit coil was used for human studies [123]. ADC and dissolved-phase studies were performed on a 1.5T MRI system (Avanto, Siemens Medical Solutions, Malvern, PA) using a flexible transmit/receive chest RF coil (IGC Medical Advances, Milwaukee, WI).

ID	Age	Gender	FEV ₁	FEV ₁ /FVC	Healthy Status	Acqu.
H1	20	M	105	88	Healthy	MXTC
H2	21	M	89	83	Healthy	MXTC
H3	19	F	104	84	Healthy	MXTC, Diss, ADC
H4	19	F	112	84	Healthy	Diss
C1	54	F	81	66	COPD	MXTC, Diss, ADC
C2	42	F	71	66	COPD	MXTC, Diss, ADC, CT
A	48	F	74	64	Asthmatic	MXTC

Table 4.1: Human subject information.

4.3.2 Hyperpolarized-Gas Production

¹²⁹Xe was polarized using a commercial prototype system (Xemed LLC, Durham, NH) [132] via spin-exchange optical pumping ([133], [132], [29]). For each set of experiments, two liters of xenon gas were accumulated in the frozen state. Subsequently, the gas was thawed into four 500-ml Tedlar bags for four breath-hold imaging experiments. In order to maintain at least 21% oxygen entering the lungs, each HXe dose was administered together with an oxygen-air mixture as described above.

4.3.3 Imaging Protocols

The MXTC pulse sequence as outlined in Fig. 4-2 and described in the Background section was implemented on a 3T MR scanner. In human studies, due to hardware limitations on the 3T scanner, the flip angle for the saturation RF pulses was limited to a maximum of 75°, resulting in incomplete

saturation of xenon magnetization in the dissolved phase [140]. A correction factor for the computation of the XTC contrast maps was determined from spectroscopic XTC experiments performed at 1.5T by comparing the gas-phase depolarization for 75° saturation pulses to that for 90° pulses. (This correction factor will be confirmed by additional studies in the future; while it affects the quantitative values in MXTC maps it does not change their qualitative appearance. Further, knowledge of the precise factor is not required to perform comparison of maps acquired in different subjects but using identical experimental parameters.) For rabbit studies 90° saturation pulses were achieved.

For human studies, the imaging parameters for the four FLASH acquisitions in the MXTC pulse sequence were: TR / TE 7.7 / 2.5 ms, image resolution 9.2 x 9.2 x 21-24 mm³, matrix 48 x 30 x 10, acceleration factor 3, reference lines 21, and receiver bandwidth 260 Hz/pixel. Non-selective, 500- μ s, rectangular RF pulses with flip angles of 1°, 1°, 2° and 4° were used for acquisitions I₁, I₂, I₃ and I₄, respectively. The flip angles for I₃ and I₄ were higher to maintain adequate SNR. Saturation pulses were 75°, 3-ms Gaussian RF pulses centered at the dissolved phase at 208 ppm. Data was collected during two to four consecutive breath-hold acquisitions (with two XTC contrasts per breath hold for human studies).

For rabbit studies only three FLASH acquisitions (one XTC contrast) were acquired per breath hold. The imaging parameters for the animal studies were: TR / TE 6 / 3 ms, image resolution 3.5 x 3.5 x 7 mm³, matrix size 32 x 28 x 10, receiver bandwidth 260 Hz/pixel, imaging flip angles 1°, 2° and 4° for the respective FLASH acquisitions. Up to eight breath holds were performed. To minimize registration errors due to different breath-hold positions, identical xenon doses and breath-hold maneuvers were used for each acquisition.

The details of the direct dissolved-phase acquisitions are explained in [25] and only briefly described here. The dissolved-phase resonance of ¹²⁹Xe is imaged directly by setting the RF transmitter and receiver frequencies to the 208 ppm resonance. Carefully adjusting imaging parameters such as flip angle (a narrow-bandwidth RF pulse is centered on the dissolved phase resonance such

that only a small side lobe of the RF-pulse profile excites the gas-phase resonance), bandwidth and resolution allows to simultaneously acquire the chemically shifted images of gas-phase xenon (ventilation) and dissolved-phase xenon (gas uptake). The ratio of the two images gives the normalized dissolved-phase map. Imaging parameters for direct dissolved-phase imaging were: flip angle 20° , TR/TE 50/2.8 ms, image resolution $12 \times 12 \times 20$ mm³, matrix size 36×80 , BW 100 Hz/pixel.

Apparent diffusion coefficient (ADC) imaging in humans has been studied extensively with hyperpolarized ³He (e.g., [8], [9], [10], [141]) and successfully applied to probe alveolar size [11]. However, there is much less experience with ADC imaging in humans using HXe. In this study, HXe short-time scale ADC maps were acquired using a standard interleaved, two b-value (0 and 10 s/cm²), slice-selective 2D-GRE implementation with a diffusion time of 3.2 ms. Other imaging parameters were: TR / TE 14 / 10 ms, flip angle 7.5° , image resolution $5 \times 5 \times 30$ mm³, matrix 96×66 , slices 6, and receiver bandwidth 220 Hz/pixel. The first image (b=0 s/cm²) was used as a spin density image to depict ventilation in subjects with lung disease.

CT data were obtained from a GE Light Speed 16 detector-row CT scanner (GE Medical Systems, Milwaukee, WI). Each scan was acquired during a short breath hold after the subject was told to take a deep breath and hold it. Coronal image slices were reconstructed at 5-mm slice thickness for the identification of emphysematous regions and additionally at 20-mm slice thickness for comparison to hyperpolarized-gas imaging techniques.

We obtained a measurement for the absolute lung volumes in the human subjects using proton MRI 3D TrueFISP acquisitions during breath holds at RV and TLC. Lung volume measurements were done at a 1.5T MRI system (Avanto, Siemens Medical Solutions) and the receive coil was a commercial 15-channel phased-array chest coil (Siemens Medical Solutions). Imaging parameters were: TR/TE = 1.7 / 0.72 ms, image resolution $3.9 \times 3.9 \times 3$ mm³, matrix $108 \times 128 \times 72$, acceleration factor 2, reference lines 24, BW 1.1 kHz/pixel.

4.3.4 Data Analysis

The raw k-space data were transferred from the MRI scanner and analyzed offline using MATLAB (MathWorks Natick, MA). Images from accelerated k-space acquisitions in human studies were reconstructed with the GRAPPA algorithm [116]. Regions of noise and low SNR in the reconstructed spin density images were removed with a threshold mask. From each breath hold data set one (rabbit) or two (human) XTC depolarization maps were calculated according to Eq. 4.1. As described earlier, depolarization maps were multiplied by a correction factor of 1.5 to account for the 75° saturation pulses in human studies. The complete MXTC data set, consisting of depolarization maps for several delay times, was fit on a voxel-by-voxel basis to Eq. 4.3 using nonlinear weighted least-square fitting. The fitting weights were the measurement errors of the depolarization maps. These were estimated using the standard deviation within each image slice. This is a valid approximation under the assumption that in the relatively large voxels not structural features but only measurement uncertainty determines the in-plane variation in the maps. The quality of each voxel fit was evaluated using the distribution of the reduced χ^2 -statistics ($Q(\chi^2/\nu, \nu)$, where ν are the degrees of freedom). Poor voxel fits with a large χ^2 ($Q < 0.05$) were rejected and corresponding voxel fit parameters were marked as invalid and excluded from further analysis.

Maps for the two fitting parameters, the maximum depolarization MXTC-F and the square root of the time constant MXTC-S ($S = \sqrt{\tau_c}$), were obtained. Using Eqs. 4.5 and 4.6, physiological microstructure parameters were calculated from the fitting parameters.

The direct dissolved-phase images were masked and the ratio of the registered dissolved-phase and gas-phase images was obtained.

ADC maps for human studies were calculated using the noise-masked image ratio ($I_{ADC,2}/I_{ADC,1}$) and b-value (10 s/cm²):

$$ADC = -\frac{1}{b} \frac{I_{ADC,2}}{I_{ADC,1}} \quad (4.7)$$

where $I_{ADC,1}$ and $I_{ADC,2}$ are the signal intensities in the $b=0$ and $b=10$ s/cm² images, respectively. For COPD subject C2, CT data were reconstructed coronally for comparison with the coronal MR acquisitions. Regions of emphysema were defined as pixels in the lung with an attenuation less than -950 HU [43].

Proton images for lung volume estimation were reconstructed offline in MATLAB (MathWorks, Natick, MA). After both, automatic and manual thresholding, pixels within the lung volume were counted and multiplied by the voxel volume. The same reconstruction was applied to the first FLASH image in the MXTC acquisition to obtain an estimate of the absolute lung volume during the MXTC experiment. Errors from automatic and manual thresholding as well as due to partial volume effects were estimated by repeated analysis with varying threshold levels and were found to be within a few percent.

4.3.5 Statistical Analysis

In order to investigate the dependency of the microstructure parameters on lung volume, an unpaired two-tailed Students t-test was applied comparing distribution means of the high lung volume experiment to the low lung volume experiment. At constant lung volume, one-way ANOVA was used to analyze the effect of image slice number in order to assess the parameter dependency along the gravitational direction. We further quantified the gravitational parameter dependence by linear fitting of parameter value medians of each image slice as a function of anterior-posterior (AP) position, starting at the most posterior partition. Significance of the slope of the linear fit was evaluated using Students t-test, comparing the slope to zero. The slope of the linear fit (AP-gradient) was normalized using $(\Delta X/X)/\Delta h$, where ΔX is the absolute parameter change over the positional change Δh along the AP direction and X is the median parameter value.

In order to quantify the extent of agreement between different imaging modalities, each image was segmented into eight regions of interest (ROIs) and the correlation of values corresponding

to the ROIs from different imaging modalities was determined. The strength of correlation was quantified using Spearman's rank correlation coefficient ρ .

4.4 Results

4.4.1 Estimation of Absolute Lung Volume

The subtle effects of lung microstructure deformation, which we seek to study using MXTC, strongly depend on lung inflation. Results for volume measurements based on proton MRI TrueFISP acquisitions are illustrated in Fig. 4-3 and Table 4.2. We compared our experimental results to predicted ventilation lung volumes for healthy subjects considering height and age [142]. There is some uncertainty associated with the method of pixel counting (threshold level, partial volume effects), however a far greater variability originated in the degree of subject effort. This is evident from the fact, that the measured vital capacity ($VC=TLC-RV$) is generally less than predicted [142] and varied strongly among subjects. The lung volume analysis suggested that the actual lung volume during MXTC was close to the predicted Functional Residual Capacity (FRC).

ID	Sex	Age	Height	Lung Volumes [Liter]					
				TLC pred.	TLC meas.	RV pred.	RV meas.	FRC pred.	XTC meas
H1	m	20	175	6.9	5.2	1.5	1.7	3.2	3.0
H2	m	21	175	6.9	3.8	1.5	2.0	3.2	4.0
H3	f	19	164	5.0	5.0	1.3	1.5	2.7	3.0
H3 TLC									4.7

Table 4.2: Absolute lung volume estimation for MXTC studies. Total lung Volumes (V_{tot}) for three healthy subjects included in the MXTC study are measured by thresholding and pixel counting of 3D-TrueFISP proton MRI scans. Predicted values from an empirical reference [142] correspond to ventilation volumes (V_a). Also shown is the measured total lung volume from the MXTC experiment. Assuming that $V_{tot} = V_a + V_t$ and $V_t = \text{const}$, the vital capacity $VC=TLC-RV$ can be compared. VC measured was found to be lower in all cases than VC predicted from [142], most likely due to subject effort.

TLC = total lung capacity; RV = residual volume, FRC = functional residual capacity

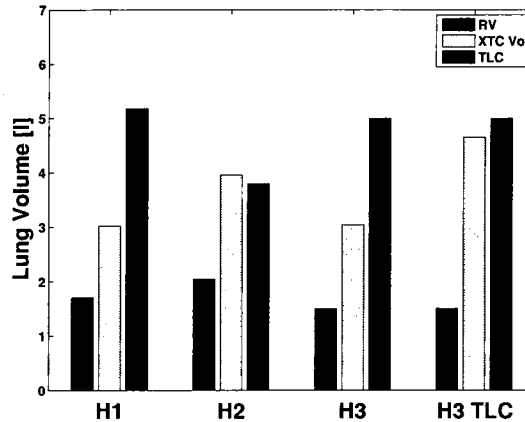


Figure 4-3: Absolute lung volume estimation for MXTC studies. Estimation of absolute lung volumes by pixel counting. Subjects were asked to hold their breath at RV and at TLC for a TrueFISP proton acquisition. A threshold mask was applied and the absolute lung volumes were calculated by pixel counting. Results show that absolute lung volumes during scanning strongly depend on subject cooperation, i.e. RV measured (blue) was higher than RV predicted, TLC measured (red) was lower than TLC predicted [142]. Subject H3 is on MRI measured absolute volumes within 300 cc of the predicted values [142], whereas on the other extreme subject H2, when asked to breath to TLC was 3 liters below predicted TLC. The analysis shows that during low volume XTC experiments (RV + oxygen, air, xenon mixture), subjects were approximately at FRC, i.e. $\sim 50\%$ TLC (H1-H3, green). For the TLC XTC experiment (H3 TLC) lung volume analysis shows consistency between absolute lung volume measured during XTC and during proton scanning and, as expected, a clear difference in lung volume to proton scanning at RV.

4.4.2 Curve Fitting Quality

Representative voxel fits are shown in Fig. 4-4.

After voxel-by-voxel curve fitting of MXTC data, a p-value was calculated to assess the fit quality ($p=1-Q$, see chapter 4.3.4). A respective p-value map is shown in Fig. 4-5 for subject H3. The center slices show higher p-values (lower fit quality), probably due to the decreased SNR for center partitions due to the sensitivity profile of the array receive coil. Another area of low fit quality is around the edges of the lung, especially close to the diaphragm and around the heart, most likely caused by motion (arrows in Fig 4-5).

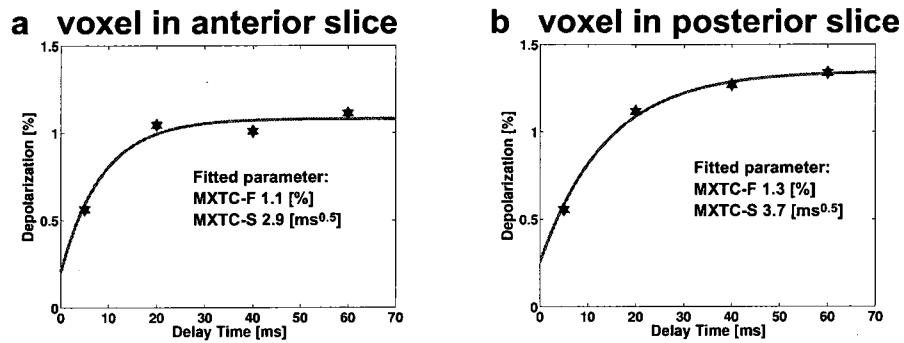


Figure 4-4: Representative MXTC voxel fits. For healthy subject H3 showing voxel data and fit in anterior (a) and posterior (b) image slice. Fitting parameter MXTC-F and MXTC-S are both higher in posterior slice.

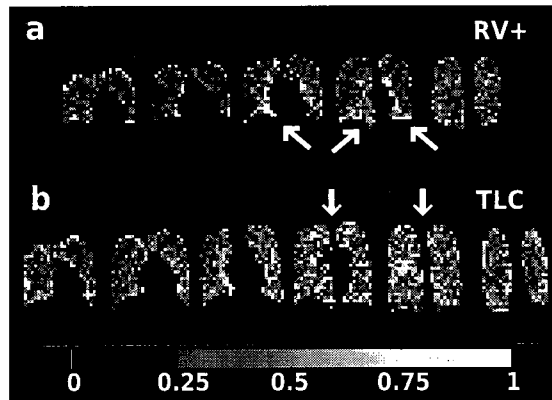


Figure 4-5: Maps of fitting quality of MXTC data. The quality of fit is illustrated for each image voxel by a p-value calculated from the χ^2 -statistics of the weighted fit result. Large p-values correspond to large fitting error χ^2 . The maps show regions of low fit quality around the edges of the lung and around the heart possibly caused by motion (white arrows in (b)). During the TLC experiment SNR was lower resulting in overall decreased fit quality, especially at the center partitions since the sensitivity of the surface coil receivers decreases with distance (white arrows in (a)).

4.4.3 Microstructure Parameter Maps in Healthy Lung Physiology

Maps for the fitting parameters MXTC-F and MXTC-S are shown for human subject H3 and rabbit R2 in Figs. 4-6 and 4-7. At the low lung volume (Fig. 4-6/4-7 a,b) we observed a homogeneous distribution of microstructure parameter values within each image slice and a gradient along the gravitational direction. Parameter values were increased in posterior images, which are the de-

pendent lung regions in the supine position. At the high lung volume (Fig. 4-6/4-7 c,d) all three parameter maps have lower values throughout the lung and the anterior-posterior (AP) gradient is less apparent. In order to rule out experimental error, one subject was also imaged prone for a single, long exchange time (60 ms) at low lung volume and we observed increased depolarization values towards the anterior images, which correspond to the dependent lung region in the prone position (Fig. 4-8).

A summary of whole lung median and standard deviation of microstructure parameters is given in Table 4.3. Assuming that within an image, i.e. within the iso-gravitational plane, the variation in the parameter distribution is due to random error only and not due to lung structure heterogeneity, the standard deviation of the respective fitting parameter distribution can be interpreted as an upper bound estimate for a confidence interval on the single voxel fitting parameter. The smallest standard deviations were found in subject H2. The fact that error estimates differ among subjects is due to the influence of external sources of error, such as motion or SNR due to variations in gas polarization levels. From the H2 data and using Eq. 4.5 and 4.6, we conclude that MXTC has the potential to determine tissue-to-alveolar-volume ratio and septal wall thickness with an accuracy better than 2% (corresponding to the standard deviation of MXTC-F: $\text{STD}(\text{MXTC-F})=0.2\%$) and $0.9\ \mu\text{m}$ ($\text{STD}(\text{MXTC-S})=0.5\ \text{ms}^{0.5}$) respectively.

4.4.4 Parameter Dependence on Lung Height and Ventilation Volume in Healthy Lung Physiology

Considering the whole lung at different ventilation volumes, we found that the means of the parameter distributions for both, MXTC-F and MXTC-S, were significantly lower at higher lung volume. Using a two-tailed Students t-test the differences were found to be significant with p-values < 0.0001 in human and rabbit studies.

To evaluate the effect of AP-position (image slice number) on parameter distributions, we used

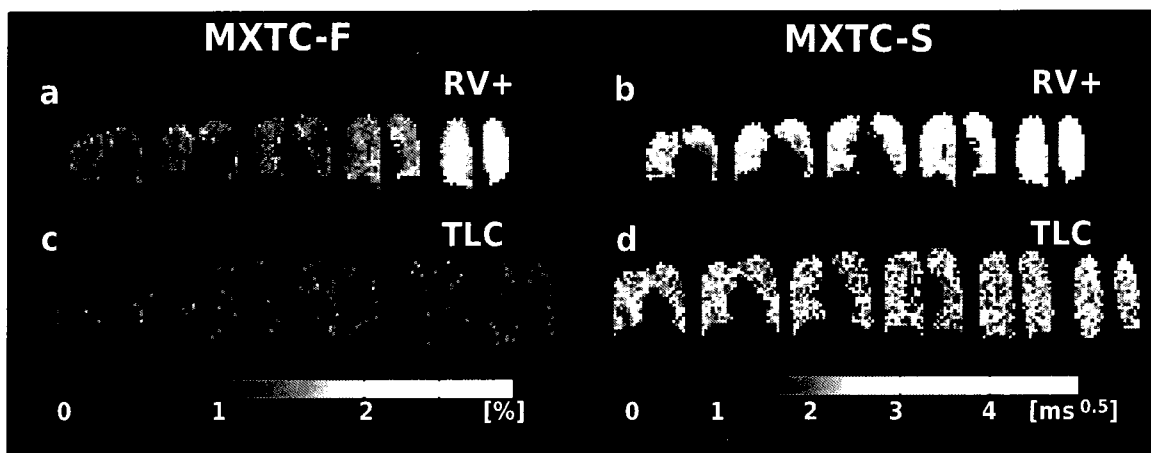


Figure 4-6: MXTC parameter maps for a healthy human subject at two different lung volumes. Maps for tissue-to-alveolar-volume ratio parameter MXTC-F, and septal wall thickness parameter MXTC-S are obtained from MXTC curve fitting (subject H3). At the lower lung volume (RV+) (a,b) elevated parameter values were found in dependent lung regions (posterior partitions). At TLC (c,d), parameter values are generally lower and appear to be more homogeneous throughout the lung.

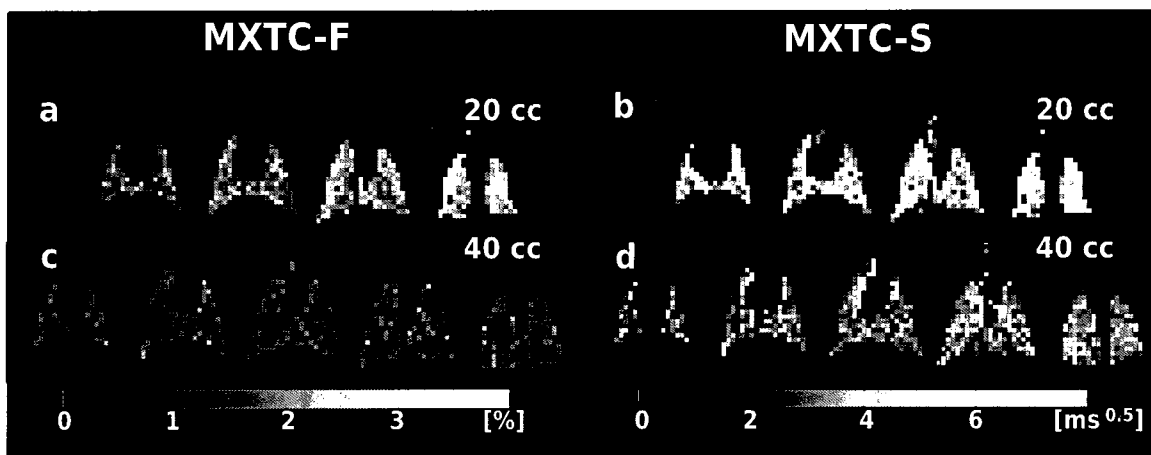


Figure 4-7: MXTC parameter maps for a rabbit ventilated to two different lung volumes. Parameter maps for tissue-to-alveolar-volume ratio parameter MXTC-F, and septal wall thickness parameter MXTC-S are shown. As for the human results an anterior-posterior (AP) gradient is clearly visible at the low lung volume (20 cc) (a,b). No AP-gradient was observed at the higher lung volume (40 cc) (c,d).

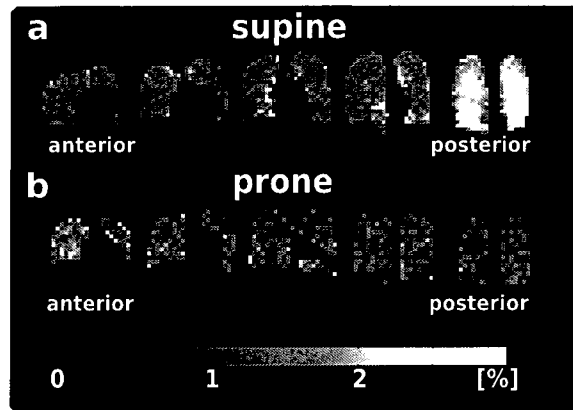


Figure 4-8: XTC depolarization maps for healthy subject H3 in the supine (a) and prone (b) position. While in the supine position higher depolarization values in the posterior (P) partitions indicate increased tissue density. This effect is consistent with the gravity-induced compression of dependent lung regions. In the prone position the orientation of the depolarization gradient is reversed as expected, since now the dependent lung regions are the anterior partitions. Also clearly visible is the better quality of the maps at 3T (a) compared to the 1.5T (b) experiment due to the RF coil (at 1.5T a custom made transmit/receive wrap coil was used with inferior B1 homogeneity and volumetric coverage compared to the 3T coil, a 32-channel phased-array receive and integrated asymmetric birdcage transmit coil).

one-way ANOVA. In human subjects at the low lung volume, the effect of AP-position accounted for 42-60 % (2-11%) of the total variation in the MXTC-F (MXTC-S) parameter variation. At TLC the effect of AP-position was less, accounting for 14% (2%) of the MXTC-F (MXTC-S) parameter variation. In rabbits at the low volume lung, AP-position accounted for 20-28% (0-6%) and at the high lung volume for 3-20% (1-3%) for the variation in MXTC-F (MXTC-S). All ANOVA results were significant (p-value < 0.005).

To further illustrate the gradient in the gravitational direction we plotted the median parameter values of each image as a function of AP-position (human, Fig. 4-9 and rabbits, Fig. 4-10). A summary of results from linear fitting of parameter value versus AP-position for all three subjects are shown in Table 4.3. For the tissue-to-alveolar-volume ratio parameter MXTC-F, the mean value \pm standard deviation for the normalized slope in three subjects at the low lung volume (RV+) was $- 6.6 \pm 0.6$ %/cm and by about a factor two lower at TLC with $- 3.2$ %/cm. The normalized slope

Human												
	MXTC-F [%]						MXTC-S[ms ^{0.5}]					
	H1	H2	H3	Mean	Std	H3 TLC	H1	H2	H3	Mean	Std	H3 TLC
WL Median	1.1	1.4	1.4	1.3	0.2	0.7	3.2	3.5	3.1	3.3	0.2	2.5
WL STD	0.5	0.4	0.5	0.5	0.1	0.2	1.6	0.9	1.0	1.1	0.4	1.4
Min Part STD	0.2	0.2	0.3	0.3	0.1	0.2	1.0	0.5	0.9	0.8	0.3	1.1
Diff AP	0.9	0.9	1.0	0.9	0.1	0.3	1.7	0.3	0.9	1.0	0.7	0.2
AP-slope [%/cm]	-7.0	-5.9	-7.0	-6.6	0.6	-3.2	-4.5	-1.0	-2.8	-2.8	1.7	-0.4
p-value	0.015	0.001	0.017	0.011	0.0	0.002	0.015	0.003	0.004	0.007	0.0	0.335
Rabbit 20 ml												
	MXTC-F [%]						MXTC-S[ms ^{0.5}]					
	R1	R2	R3	R4	Mean	Std	R1	R2	R3	R4	Mean	Std
WL Median	2.4	2.1	2.0	1.9	2.1	0.2	5.6	4.8	4.1	4.0	4.6	0.7
WL STD	0.7	0.8	1.0	0.8	0.8	0.1	1.5	1.4	1.9	1.6	1.6	0.3
Min Part STD	0.5	0.5	0.4	0.3	0.4	0.1	1.3	1.0	1.3	1.4	1.3	0.2
Diff AP	1.2	1.0	1.3	1.3	1.2	0.1	0.6	0.6	0.8	0.3	0.6	0.2
AP-slope [%/cm]	-16.1	-17.3	-22.7	-17.6	-18.4	2.9	-4.0	-4.0	-7.2	-2.8	-4.5	1.9
p-value	0.009	0.037	0.003	0.001	0.013	0.016	0.199	0.428	0.095	0.113	0.209	0.153
Rabbit 40 ml												
	MXTC-F [%]						MXTC-S[ms ^{0.5}]					
	R1	R2	R3	R4	Mean	Std	R1	R2	R3	R4	Mean	Std
WL Median	1.8	1.2	1.7	1.4	1.5	0.3	4.6	3.3	4.9	3.8	4.2	0.8
WL STD	0.5	0.4	0.5	0.5	0.5	0.1	1.5	1.6	2.0	1.3	1.6	0.3
Min Part STD	0.4	0.3	0.5	0.2	0.4	0.1	1.3	1.3	1.7	0.9	1.3	0.3
Diff AP	0.4	0.4	0.4	0.7	0.5	0.1	0.5	0.6	1.6	1.2	1.0	0.5
AP-slope [%/cm]	-7.8	-7.5	-8.2	-13.0	-9.1	2.6	-3.9	-4.5	-9.6	-9.2	-6.8	3.0
p-value	0.006	0.027	0.169	0.001	0.051	0.079	0.083	0.038	0.174	0.024	0.079	0.068

Table 4.3: MXTC results for healthy subjects (H1-H3) and rabbits (R1-R4) at two different ventilation volumes. For individual subject/rabbit parameter values MXTC-F and MXTC-S are given as whole lung (WL) median and standard deviation (STD), the minimum standard deviation for one partition (Min Part STD) to estimate the error for voxel parameter estimation, the absolute difference between most anterior and most posterior image slice (Diff AP), anterior-posterior slope of linear fitting of median parameter value as function of lung height (image slice number) normalized to whole lung median (AP-slope, multiplied by 100 to report as parameter change in %/cm) and the p-value of the AP-slope obtained by comparing to zero slope using Student's t-test. Mean and standard deviation are also given for subject/rabbit population at respective lung volumes.

for the septal wall thickness parameter MXTC-S at RV+ (-2.8 ± 1.7 %/cm) was about a factor two lower than the volume ratio (MXTC-F) slope at the same lung volume. All slopes were statistically significant (p -value < 0.05), except for the slope of parameter MXTC-S at TLC (p -value = 0.335). For rabbits the normalized slope for MXTC-F was -18.4 ± 2.9 %/cm at low ventilation volume and, similar to the human results, by approximately a factor two lower at high volume with -9.1 ± 2.6 %/cm. In rabbits, the slopes for parameter MXTC-S did not reach significance.

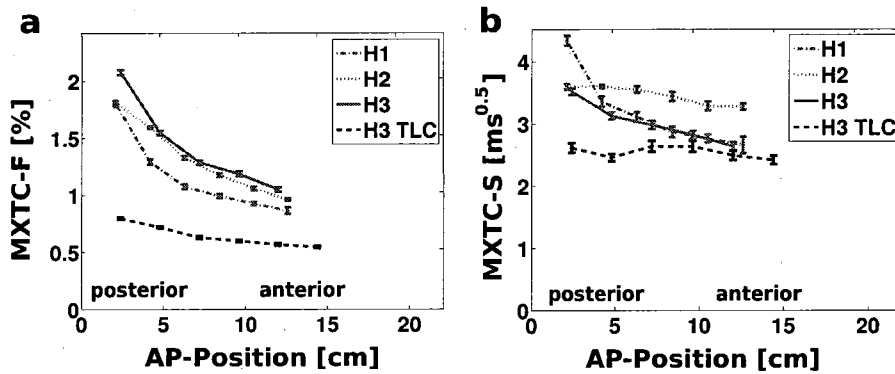


Figure 4-9: AP parameter dependence for healthy subjects at two different lung volumes. The median parameter values for each partition are plotted as a function of lung height: MXTC-F (a) and MXTC-S (b) for subjects H1-H3 at FRC (blue) and H3 at TLC (black). Errorbars are the standard error of the mean. The curves show an AP gradient for parameter values at low lung volume (blue), which is less apparent in the TLC experiment (black).

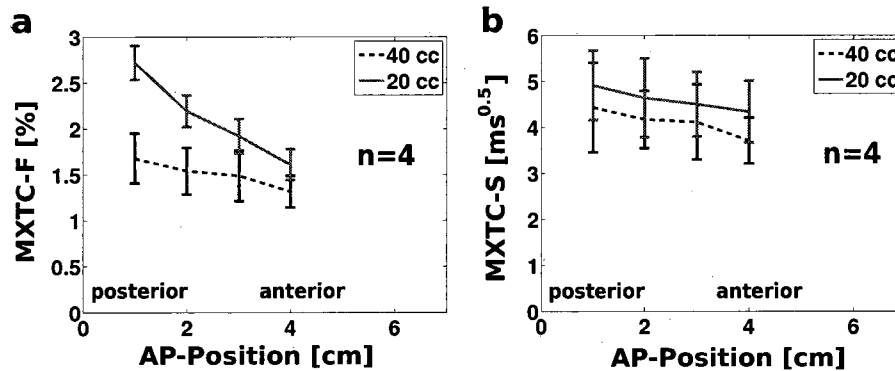


Figure 4-10: The mean parameter values (errorbars are the standard deviation of four rabbit mean values) as a function of lung height for four rabbits: MXTC-F (a) and MXTC-S (b) at 20 cc (blue) and 40 cc ventilation (black). As in the human results the AP gradient is more pronounced during the low volume experiment for MXTC-F, but no volume dependence of the gradient was found for MXTC-S. However, especially for MXTC-S, differences among rabbits are large as indicated by the errorbars.

4.4.5 Results in Subjects with Lung Disease Compared to Healthy Subjects

Spin Density Maps in Subjects with Lung Disease

Spin density images as discussed earlier depict ventilation. For the two COPD subjects included in this study ventilation images are shown in Fig. 4-11. Only few ventilation defects are visible on the spin density image of COPD subject C1. For COPD subject C2 no distinct defects, but minor shading indicates lower ventilation in the upper right lobe of anterior images.

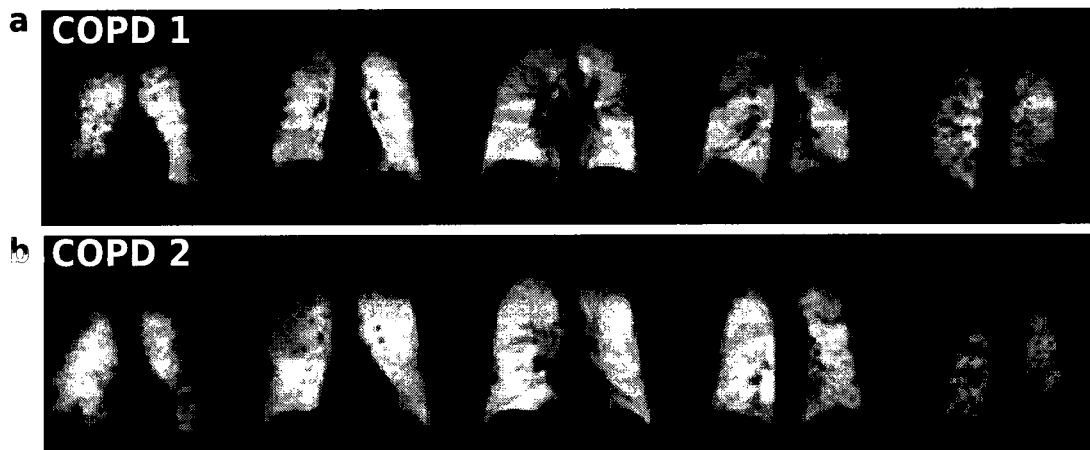


Figure 4-11: HXe spin density images showing regional ventilation in subjects C1 and C2. Ventilation appears relatively homogeneous with only few defects for COPD subject C1 (a) and few defects in most posterior slice as well as slightly less ventilated upper right lobe in anterior slices of COPD subject C2 (b).

MXTC Parameters in Subjects with Lung Disease Compared to Healthy Subjects

Maps of the two MXTC parameters from healthy subjects (subjects H1-H3) were generally homogeneous within each coronal image slice, but increased values were observed towards the posterior of the lung (Fig. 4-12 a, b). This observation is consistent with the effect of gravity-induced lung-tissue compression in dependent lung regions [87] [88] [143] [144] [145], which are the posterior image slices for a subject in supine position. The MXTC parameter maps from the two COPD subjects C1 (GOLD stage I, FEV1/FVC = 0.66, FEV1 = 81% predicted) and C2 (GOLD stage II,

FEV1/FVC = 0.66, FEV1 = 71% predicted) appeared to be considerably more heterogeneous (Fig. 4-12 e, f [subject C1] and g, h [subject C2]). Further, the parameter maps for the COPD subjects differed from those of the healthy subjects and also from each other. For the asthmatic subject (Fig. 4-12 c, d [subject A1]), the maps for the tissue density parameter MXTC-F appeared similar to healthy subjects. The values for the septal thickness parameter MXTC-S were elevated throughout the lung in all three subjects with lung disease (Fig. 4-12 d, f, h) compared to healthy subjects (Fig. 4-12 b).

To analyze differences among the parameter maps in more detail, we quantified the anterior-posterior parameter dependence by plotting the median MXTC parameter values for each image slice as a function of lung height (Fig. 4-13). Linear fitting showed that all healthy subjects had a statistically significant ($p < 0.05$) negative AP-gradient slope for the MXTC-F parameter. A negative slope corresponds to increased parameter values in posterior images, consistent with the gravitational tissue-compression effect. In contrast, COPD subject C1 did not exhibit a significant AP-slope for the MXTC-F parameter (Fig. 4-12 e, Fig. 4-13 a and Table 4.4), while COPD subject C2 had increased MXTC-F parameter values in posterior images. However, the AP dependence for subject C2 was not statistically significant (Fig. 4-12 g, 4-13 a and Table 4.4). This subject also had regions of decreased MXTC-F (Fig. 4-12 g) within images, resulting in overall lower median values for anterior images compared to the parameter range in healthy subjects (Fig. 4-13 a). The results for the asthmatic subject A1 (FEV1/FVC = 0.64, FEV1 = 74% predicted) was similar to the results of the normal subjects for the MXTC-F parameter with a significant, negative slope along the AP direction (Fig. 4-12 c, 4-13 a and Table 4.4).

The AP-slope for the wall-thickness parameter MXTC-S was statistically significant and negative for all three healthy subjects (H1-H3), but the relative changes were less than those associated with the AP-slope for MXTC-F (Fig. 4-13, Table 4.4). For subjects C2 and A1, the slope of the wall-thickness parameter MXTC-S along the AP direction was not significant, whereas for subject

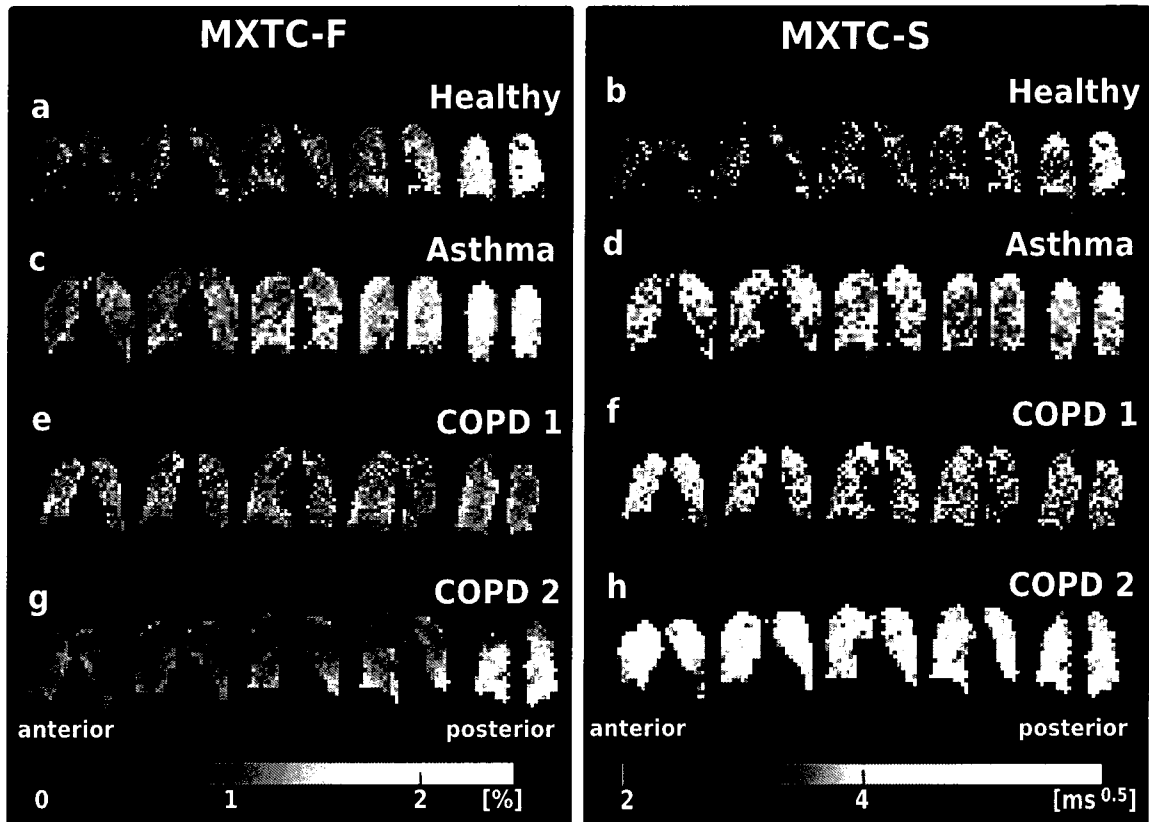


Figure 4-12: MXTC parameter maps for subjects with lung disease compared to a healthy subject. The MXTC-F parameter map, which represents regional tissue to alveolar-volume ratio, clearly shows increased parameter values in posterior images for healthy subject H1 (a) and similar for asthmatic subject A1 (c). In contrast for COPD subject C1 no substantial variation in parameter values along the anterior-posterior direction (e) is observed. For COPD subject C2 regions of decreased parameter values in the upper portions of anterior images (g) are apparent. The second MXTC parameter, MXTC-S, exhibits increased values in posterior images for the healthy subject (b), similar to MXTC-F, whereas the anterior-posterior dependence appears reversed in subject C1 (f). Compared to the healthy subject, MXTC-S in all subjects with lung disease appears elevated throughout the whole lung (d, f, h).

C1 the slope was found to be positive, corresponding to increased parameter values in the non-dependent anterior images (Fig. 4-13 b, Table 4.4). For the subjects with lung disease, the medians of the MXTC-S parameter were elevated either in all coronal images (subject C2), or in all but the most posterior images (subjects C1 and A1), relative to those observed for the three healthy subjects (Fig. 4-13 b).

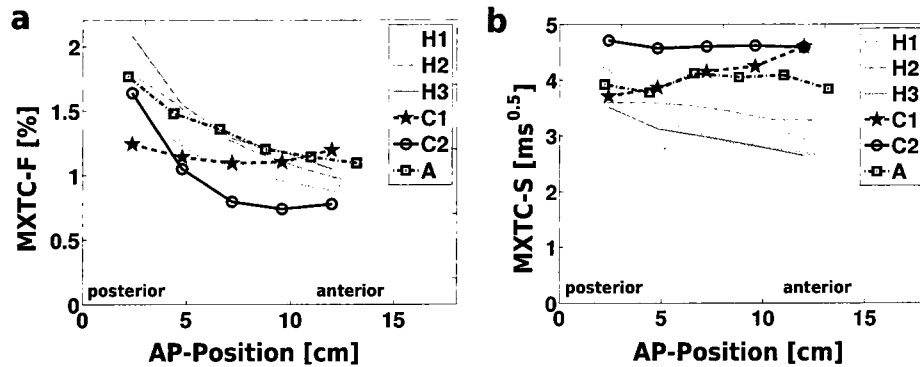


Figure 4-13: Dependence of MXTC parameters on lung height for subjects with lung disease. The median values of MXTC-F (a) and MXTC-S (b) for each image are plotted as a function of anterior-posterior (AP) position, measured from the most posterior image. Data from the healthy subjects (H1-H3) are shown in gray shading, while data from the COPD subjects (C1, C2) and asthmatic subject (A1) are plotted explicitly. For MXTC-F, the AP-dependence for A1 appears comparable to that for H1-H3, whereas C1 does not show any AP dependence and C2 has lower parameter values in anterior images (a). The MXTC-S parameter appears elevated for the subjects with lung disease (C1, C2, A1), especially in the anterior images, due to the absence of an AP-dependence in comparison to the healthy subjects (H1-H3) (b).

MXTC-F Compared to Other Imaging Techniques

For the normalized dissolved-phase ratio (i.e. dissolved-phase signal divided by gas-phase signal), the AP dependence was analyzed analogously to the MXTC analysis (Fig. 4-14, Table 4.4). As for the MXTC-F parameter, the AP-slope of the DP ratio data was negative and statistically significant for two healthy subjects (p-value < 0.01, H3 and H4 in Table 4.4). The AP dependence of the DP ratio data for subject C2 was comparable to the healthy subjects, whereas for subject C1 the AP slope was positive (p-value < 0.01, Table 4.4 and Fig. 4-14).

The CT data for subject C2 demonstrated a statistically significant and positive dependence on lung height, in concordance with MXTC-F and DP results in this subject. Analysis of the AP dependence of ADC measurements did not show a significant slope in any of the three subjects in whom ADC imaging was performed (H3, C1, C2, Table 4.4).

From the CT data for subject C2, we identified regions of emphysema by applying a threshold of

ID	H1	H2	H3	H4	C1	C2	A1
Age [y]	20	21	19	19	54	42	48
Gender	M	M	F	F	F	F	F
Health Status	Healthy	Healthy	Healthy	Healthy	COPD	COPD	Asthmatic
FEV1 [% pred]	105	89	104	112	81	71	74
FEV1/FVC	0.88	0.83	0.84	0.84	0.66	0.66	0.64
MXTC-F Med(Std) [%]	1.1(0.5)	1.4(0.4)	1.4(0.5)		1.2(0.3)	0.9(0.5)	1.3(0.3)
AP-slope [%/cm]	-7.0	-5.9	-7.0		0.0	-9.1	-4.4
p-value	0.015	0.001	0.017		0.940	0.067	0.003
MXTC-S Med(Std) [ms ^{0.5}]	3.2(1.6)	3.5(0.9)	3.1(1.0)		4.1(1.6)	4.6(0.9)	3.9(1.0)
AP-slope [%/cm]	-4.5	-1.0	-2.8		1.7	-0.2	0.2
p-value	0.015	0.003	0.004		0.006	0.301	0.743
DP Med(Std)			1.6(0.6)	1.3(0.4)	1.6(0.4)	1.3(0.5)	
AP-slope [%/cm]			-8.8	-6.5	1.3	-6.9	
p-value			0.002	0.000	0.008	0.002	
ADC Med(Std) *1e2[cm ² /s]			3.8(1.5)		5.0(1.9)	6.0(2.9)	
AP-slope [%/cm]			-0.4		0.0	3.1	
p-value			0.524		0.963	0.055	
CT Med(Std) [HU]						-872(40)	
AP-slope [%/cm]						0.6	
p-value						0.007	

Table 4.4: MXTC, ADC, DP and CT results for healthy subjects and subjects with lung disease. Results given for healthy subjects (H1-H4), subjects with COPD (C1, C2) and asthmatic subject (A1) include whole lung parameter median (Med) and standard deviation (Std), anterior-posterior (AP) slope of linear fitting of median parameter value as function of lung height normalized to whole lung median, multiplied by 100 and the p-value of the AP-slope obtained by comparing to zero slope using Student's t-test.

-950 HU (Fig. 4-15). These data were treated as the gold standard to locate regions of emphysema [43] in this particular subject and compared to results from the HXe imaging techniques. Parameter maps for MXTC-F, DP and ADC appeared qualitatively similar to the CT data, with regions of abnormally low (MXTC-F, DP) or high (ADC) parameter values identifying emphysematous tissue destruction in the upper lobes of this subject (white arrows in Fig. 4-16). Regional comparisons among MXTC-F, DP, ADC and CT in COPD subject C2 resulted in high correlations (Spearman's $\rho = 0.77-0.94$) (Fig. 4-17). For COPD subject C1 regional comparison among imaging modalities resulted in lower correlations ($\rho = 0.25-0.59$), most likely because the parameter distribution in this subject was fairly homogeneous throughout the lung and did not show distinct regional differences. For healthy subject H3 correlation between MXTC-F and DP was high ($\rho=0.94$) but low for

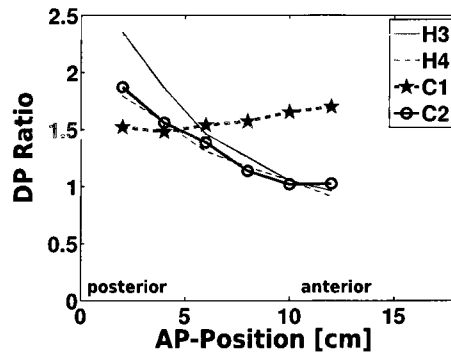


Figure 4-14: Dependence of dissolved-phase ratio (DP) parameter on lung height. Similar to MXTC-F the DP partition medians show an AP-dependence for healthy subjects (H3, H4 in gray) and subject C2 but not for subject C1.

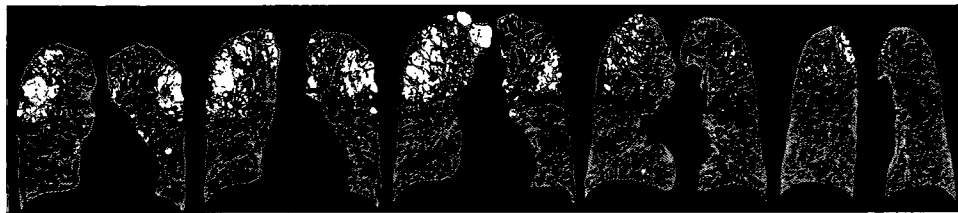


Figure 4-15: CT data analysis for COPD subject C2. A threshold mask (overlay in red) at -950 HU reveals areas of emphysema in the upper lobes of anterior images.

MXTC-F/DP and ADC ($\rho=0.11/0.22$) because ADC, unlike MXTC-F and DP did not show an AP dependence.

Histograms in Fig. 4-18 reveal distinct differences in the parameter distributions of healthy and emphysematous regions in subject C2.

4.5 Discussion

In this preliminary study we have shown that MXTC has the potential to provide a regional assessment of gas exchange and yields two parameters linked to physiologically important characteristics of the lung microstructure: 1) MXTC-F, which is proportional to the ratio of functional lung tissue-

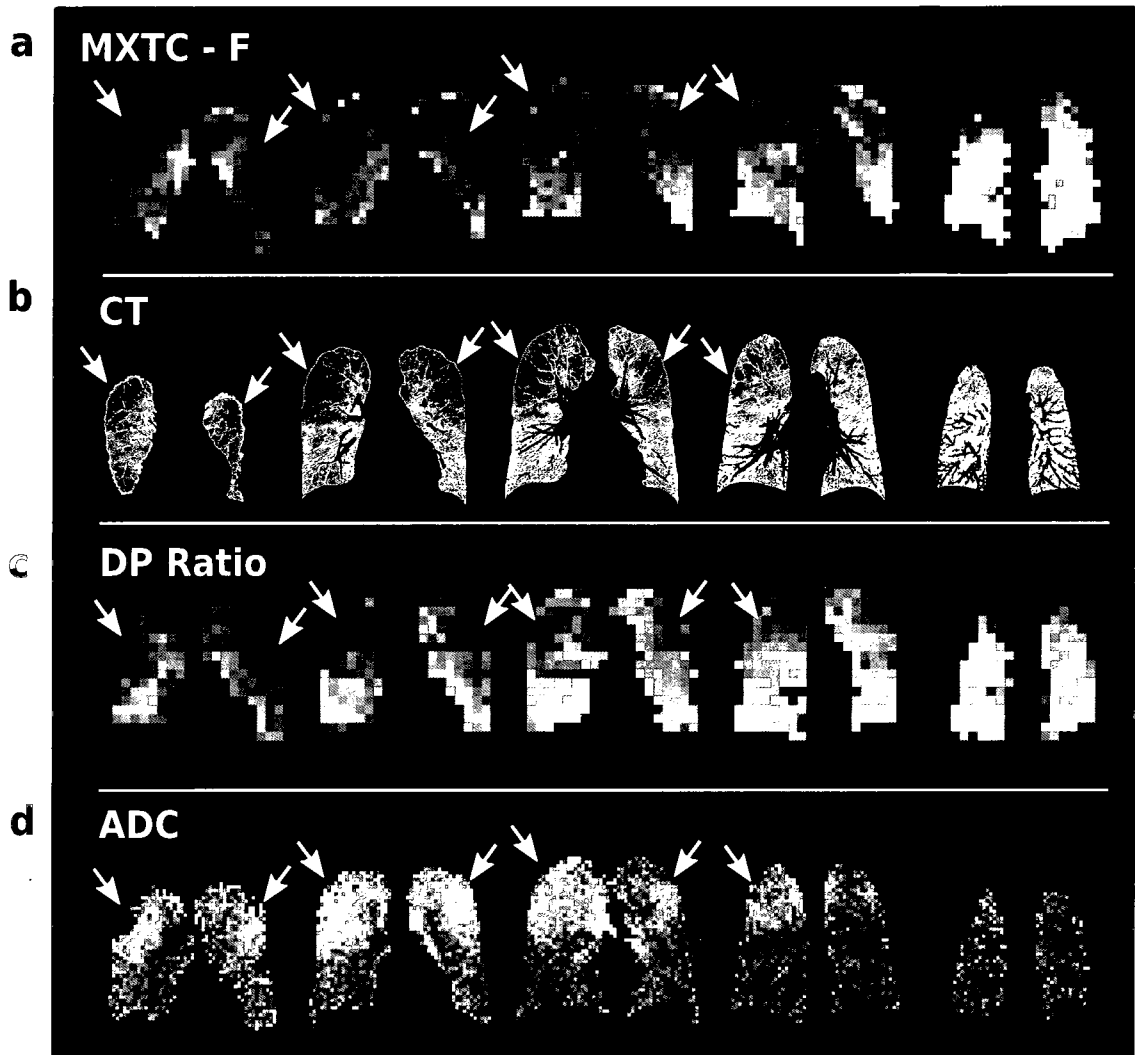


Figure 4-16: Results from CT and HXe imaging methods for COPD subject C2. The different imaging techniques depict emphysema in the same regions of the lung, which is characterized as decreased parameter values in MXTC-F (a), CT (b) and DP (c) and increased parameter values in ADC (d).

to-alveolar-volume, and 2) MXTC-S, which is proportional to the functional septal wall thickness and also reflects xenon diffusivity in the septa. Acquiring both parameters simultaneously allows a change in relative tissue density (MXTC-F), induced by a change in the number of alveolar walls per unit volume (e.g., emphysematous tissue destruction resulting in enlarged air spaces), to be discriminated from a change in the alveolar wall thickness (MXTC-S, e.g. thinning by distention secondary

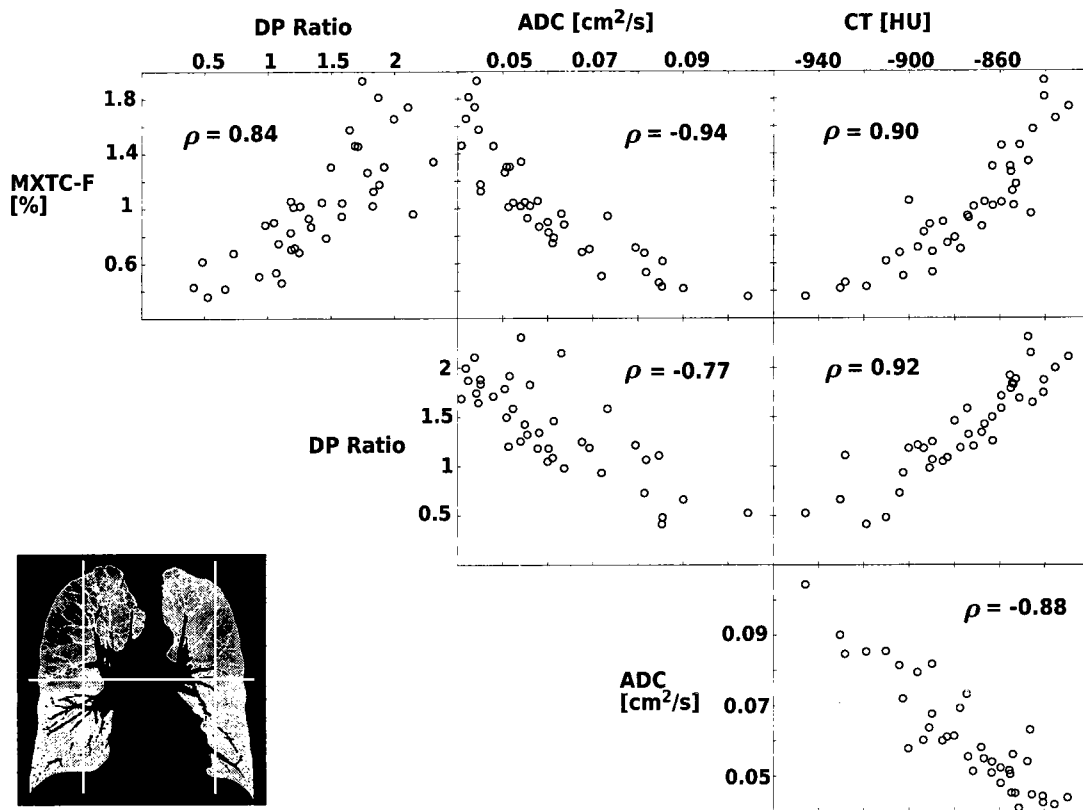


Figure 4-17: Regional correlation between HXe imaging techniques and CT. ROIs are obtained by dividing each coronal image as shown. Median parameter values for respective ROIs are compared for all techniques. Based on Spearman's value, excellent correlation was found in all cases.

to high ventilation volumes or a thickening in patients reflecting parenchymal inflammation, fibrosis or other processes that affect the septal wall thickness).

The practical application of MXTTC was facilitated by increased HXe polarization levels [132] [29], as well as by advances in RF coil technology [123]. A custom-made phased-array human-chest receiver RF coil permitted a reduction in acquisition time by parallel imaging, which allowed us to encode two delay-time points in a single breath hold. An integrated birdcage transmit coil provided increased B1-excitation homogeneity, which is crucial for unbiased contrast generation.

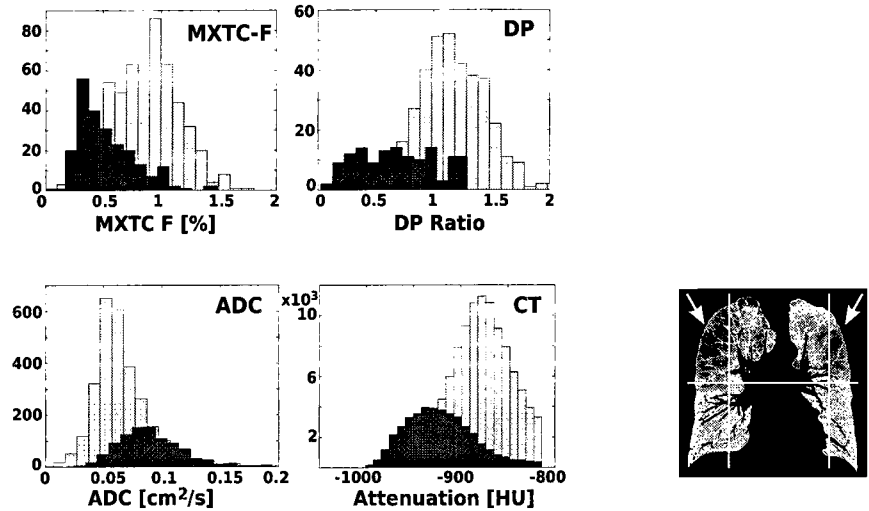


Figure 4-18: Comparison of parameter distributions in emphysematous (dark bars in plots) and healthy (light bars in plots) ROIs for the imaging methods. Emphysematous ROIs were defined in anterior partitions as indicated by white arrows.

4.5.1 Absolute Lung Volumes

Since morphometric parameters such as volume and surface densities in the lung strongly depend on inflation volume, considering the absolute lung volume is crucial while comparing results from different studies. Based on a volume analysis by pixel counting of MRI 3D acquisitions, we found that our studies at the low lung volume were at approximately FRC absolute volume. This is consistent with the fact that our results at the low volume are a factor of two higher (corresponding to half the ventilation volume and assuming tissue content is constant) compared to the TLC results. In future studies absolute lung volumes such as TLC can be determined in a pulmonary function lab for each individual subject, while the absolute lung volume during imaging could be obtained by interleaving the MXTTC pulse sequence with a fast proton image acquisition, e.g. during the contrast generation phase. The interleaved proton acquisition data could be further used to register MXTTC data from different breath holds in order to reduce the uncertainty in parameter estimation.

4.5.2 Parameter Uncertainty

The p-value map, which characterizes regional fitting quality (Fig. 4-5), indicates that fitting quality is decreased in regions affected by motion (close to the diaphragm and close to the lung borders) and regions of low SNR (in center slices, due to the receive arrays surface coil sensitivity profile). In future studies motion errors could be addressed using the interleaved proton acquisition approach mentioned earlier in combination with image registration algorithms. Further, the interleaved scheme would offer opportunities for acquisition optimization to improve SNR, e.g. collecting multiple XTC contrast maps while continuously breathing HXe (free breathing).

As discussed earlier, the standard deviation of the fitting parameter distribution within an isogravitational image slice provides an upper bound for fitting parameter uncertainty for individual voxels. Converting our best human results (H2) to physiological parameters, we can therefore conclude that MXTC has the potential to determine in vivo functional tissue-to-alveolar-volume ratio with an accuracy better than 2 % and functional septal thickness better than $0.9 \mu\text{m}$.

4.5.3 Functional Microstructure in Healthy Subjects and Rabbits

Lung Microstructure Deformation Along the Gravitational Direction

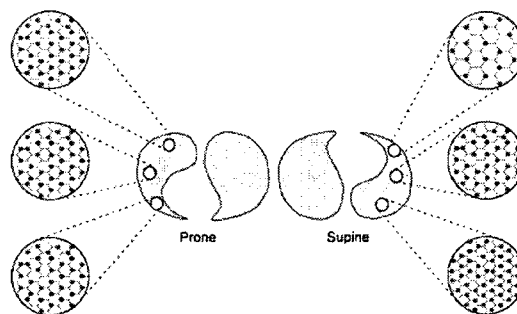


Figure 4-19: Schematic of gravity induced tissue compression. In dependent regions lung tissue is compressed in response to the weight of the lung. The effect is more pronounced at the supine position. Adapted from [146]

The compression of lung structures at low ventilation volumes in the dependent regions, caused by the lungs own weight (Fig. 4-19), is a well known effect and was also observed in various imaging studies [86] [134] [25] [143] [145] [147] [148] [149] [144] [94] [87] [88]. For our experiments the subjects were usually placed inside the MR scanner in a supine position and, as a result, the direction of non-dependent to dependent lung regions is from anterior to posterior images. In order to demonstrate the sensitivity of MXTC to assess lung microstructure, we quantified the AP-gradient of MXTC parameters in healthy subjects and rabbits. The normalized slope along the gravitational direction for the tissue-to-alveolar-volume ratio parameter MXTC-F was - 6.6%/cm for human data and a factor of 2 lower at TLC, indicating decreased lung compliance at higher ventilation volume impeding the subtle gravitational tissue deformation. Our result at low lung volume is $\sim 30\%$ higher than reported whole lung density gradients, measured at FRC with proton MRI (-4.9 ± 1.9 %/cm [145]), at RV using CT (-4.4 %/cm, [147]) and during quiet breathing with PET (-5 ± 1.2 %/cm, [148]) and SPECT (-5.1 %/cm, [149]). An important difference between MXTC-F AP-gradients and whole lung density gradients is that MXTC-F considers parenchymal structures only, whereas proton MRI, CT and transmission PET measure whole lung density gradients, which also include larger and consequently more rigid extra-parenchymal structures. In light of these considerations, the fact that our result is $\sim 30\%$ higher, is in excellent agreement with a PET study result from Brudin et.al. [144], who found that correcting for extra-capillary blood volume increases the AP-gradient by 30%.

The deformation of parenchymal lung microstructure in the supine position has been previously observed using other hyperpolarized gas MR techniques such as ADC and q-space measurements, which probe alveolar size. However, either only overall trends were observed [94] [87] or the vertical slope was less than half of our result and the literature values (~ -2 %/cm, calculated from [86] [88]). Also in recent studies of direct dissolved-phase imaging of HXe, AP-gradients were observed, indicating increased HXe uptake in dependent lung regions [134] [25].

Comparing our results for the vertical density gradient in rabbit and human studies, we found that the normalized slopes for the tissue-to-alveolar-volume parameter in the rabbit experiments are approximately three times the values found in human studies (Table 4.4). This is consistent with the result obtained by Davidson et. al. [150], who found that lung compliance in rabbits is approximately 2.5 times greater than in man.

We also observed gravitational gradients for the septal wall thickness parameter MXTC-S, however these were considerably lower than the MXTC-F gradients. The observation, that inflation volume and gravitational tissue deformation has an effect not only on the tissue-to-alveolar-volume ratio parameter, but also on the septal wall thickness parameter, indicates that the lung microstructural response is not only folding and unfolding, but also relaxation and distention of alveolar septa (Fig. 4-20).

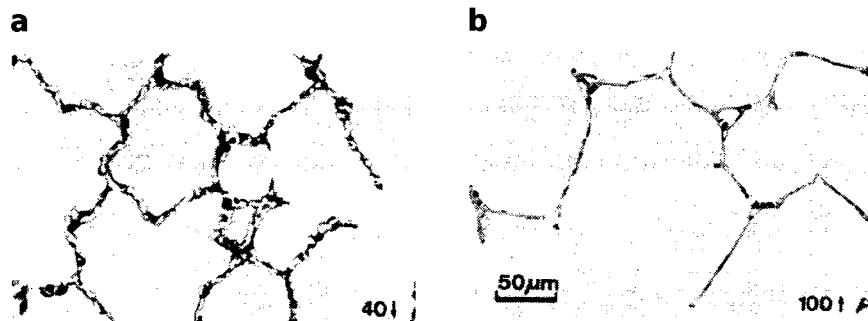


Figure 4-20: Micrograph of rabbit lung at 40% TLC lung inflation (a) and at TLC (b). At TLC alveolar air spaces are larger and septal walls appear thinner (stretched). Adapted from [151].

The Tissue-to-Alveolar-Volume Ratio Parameter MXTC-F

The gold standard for a quantitative assessment of lung structure is the use of stereological methods applied to ex vivo tissue samples [152]. The stereological method, which is the definition of physical properties of 3D structure from 2D sections, considers several levels: level 1 distinguishes parenchyma from non-parenchyma (10-15% [152]), level 2 differentiates between tissue septa and

alveolar and duct air spaces, level 3 assesses the capillary blood and alveolo-capillary tissue compartments within tissue septa and level 4 refers to tissue composition (epithelium, endothelium and interstitium) (Fig. 4-21).

Level	Magnification	Components analyzed				
I	macroscopic 1-5x	lung parenchyma				non- paren- chyma
II	light microscope ~ 100 x	"tissue" septa		pre- and post- capillary	alveolar air	duct air
III	electron microscope ~ 4000 x	capillary blood	alveolo-capillary tissue			
IV	electron microscope ~ 20 000 x		epi- thelium	inter- stitium	endo- thelium	

Figure 4-21: Classification of stereology levels. The schematic further shows the volumetric components associated with the respective level. Adapted from [30].

In this study, V_t/V_a derived from MXTC-F measures the septal volume (no distinction between tissue and blood compartments in non-selective XTC as implemented in this study) divided by total ventilation volume. The MXTC contrast however is exclusively derived from septal structures participating in gas transfer occurring between alveolar air spaces and alveolar septal walls. Therefore the reference space for MXTC parameters could be classified as a functional subspace of level 2. As a result MXTC-F derived V_t/V_a (here the tilde refers to functional volume) is expected to be lower than the parenchymal V_t/V_a derived from histology. In concordance with these considerations, V_t/V_a derived from MXTC was lower than literature results obtained by histology. For rabbits, derived from MXTC-F yielded 0.19 - 0.24 at low lung volume (FRC + 20 ml ~ 55% TLC [150] [153]) and 0.12 - 0.18 at high lung volume (FRC + 40 ml ~ 70% TLC [150] [153]). As expected these results are lower than parenchymal septal volume fraction reported by Knudsen et.al., who obtained 0.26 for at 40% TLC and 0.19 at 80% TLC [153].

The Septal Thickness Parameter MXTC-S

The calculation of mean septal wall thickness from the second parameter MXTC-S, requires knowledge of the diffusion constant D_m for ^{129}Xe in tissue structures (Eq. 4.6). Using a previously estimated value for D_m in XTC studies ($D_m = 0.33 \times 10^{-5} \text{ cm}^2/\text{s}$ [27]), we obtained 5.5 - 6.3 μm for human data at low lung volume. These results are comparable to literature values for mean septal wall thickness, which report 5-8 μm [152] [44]. MXTC as applied in this study does not distinguish between the blood and tissue resonances of dissolved-phase xenon. Therefore, the average thickness measured by xenon exchange averages over capillary diameter ($\sim 10 \mu\text{m}$ [39]) and air-blood barrier structures ($\sim 3.5 \mu\text{m}$ human, $\sim 1.2 \mu\text{m}$ rabbits [154]). The average septal wall thickness for rabbits is expected to be $\sim 1 - 2 \mu\text{m}$ thinner than for humans. However, we measured slightly higher values with 8.3 μm at 20 ml ventilation and 7.5 μm at 40 ml ventilation.

One factor of uncertainty in the calculation of the septal wall thickness is the error associated with the estimated value of the xenon diffusion constant within the lung tissue. The value we are using was calculated from the spectroscopically determined time constant for pulmonary HXe gas exchange and literature values for mean septal wall thickness [27] with the underlying assumption of a homogeneous wall composition. However, lung structures consist of various components, such as collagen, elastin, fibroblasts, basement membranes, capillaries, etc. in relative composition that varies between species [154]. Also, the neglected association and disassociation of xenon atoms with hemoglobin molecules will yield an effective diffusion constant that is lower than the true diffusion constant. Therefore, the estimated diffusion constant we used can only serve to obtain a rough estimate of the mean septal wall thickness and does not permit valid inter-species comparisons. In the future, a more comprehensive assessment of the composite parenchymal structure can be achieved by using MXTC MRI to selectively encode contrast for the individual dissolved-phase resonances of red blood cells, plasma and tissue [65].

4.5.4 Functional Microstructure in Subjects with Obstructive Lung Disease

Main findings were the excellent regional correlation of MXTC-F with HXe ADC MR imaging as well as with CT in one subject, and the observation of increased MXTC-S, indicating parenchymal thickening possibly due to inflammation, in subjects with lung disease compared to healthy subjects.

The Tissue-to-Alveolar-Volume Ratio Parameter MXTC-F

Emphysematous lung is defined as an “[...] abnormal, permanent enlargement of air spaces distal to the terminal bronchiole, accompanied by the destruction of their walls [...]” [42]. These pathological changes in lung microstructure were assessed in COPD subject 2 (GOLD stage II) by two imaging modalities that are sensitive to tissue density (MXTC-F and CT) and one that reflects airspace size (HXe ADC). For the emphysematous regions identified in this subject, we found excellent regional correlation between the experimental HXe imaging techniques and the clinically established imaging modality CT. However, since MXTC-F is based on xenon gas exchange in the lung parenchyma, this parameter represents true functional information, whereas both CT and ADC imaging represent structure, which only indirectly leads to lung function information via the structure-function relationship. Unlike COPD subject C2, subject C1 (GOLD stage I) exhibited no distinct regions in the MXTC-F maps that were consistent with the expected appearance of emphysema. On the other hand, this subject appeared distinctly different from healthy subjects due to the absence of a gravity-induced AP-gradient in median MXTC-F values.

The Septal Thickness Parameter MXTC-S

The functional importance of MXTC-S is evident, given that an increase in alveolar wall thickness is a known factor in diminishing the efficiency of gas exchange. In this study, the MXTC-S parameter in subjects with lung disease was found to be higher than that in healthy subjects. Vlahovic and colleagues ([155]) have already found a significant correlation between the degree of emphysema

and the thickening of alveolar walls (Fig. 4-22).

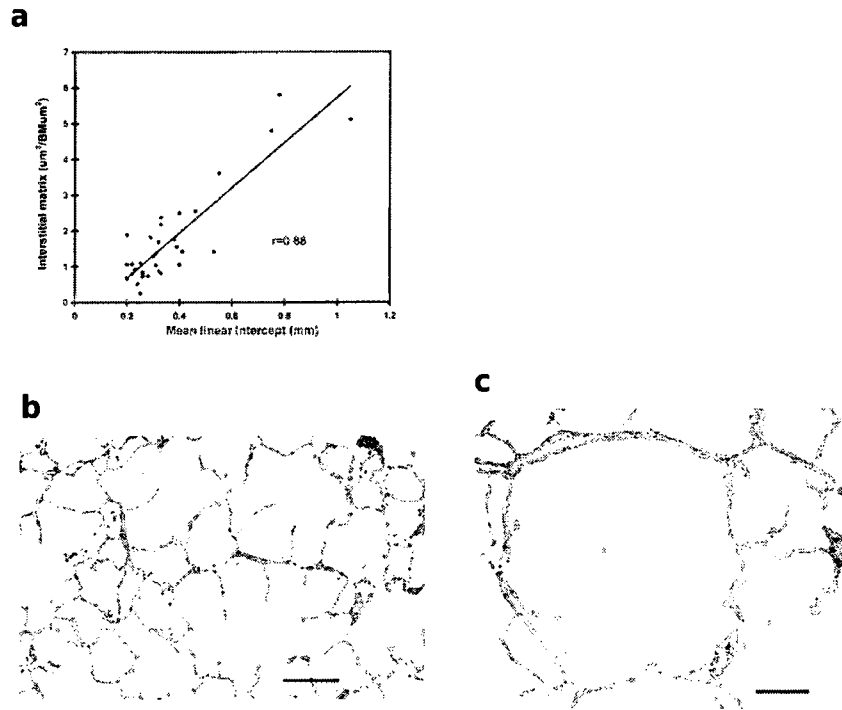


Figure 4-22: Increased interstitial thickness with degree of emphysema. (a) Correlation of L_m with the average thickness of the alveolar interstitial matrix. Matrix is expressed as volume per unit surface area of alveolar epithelial basement membrane. (b) Light microscopic photomicrograph of normal human lung. The section was stained with toluidine blue. Bar = 200 μm . (c) Light microscopic section showing the enlargement of gas exchange spaces that is characteristic for emphysema. This example illustrates the pattern of thickened interstitium observed in emphysematous lesions in human lungs. The section was stained with toluidine blue. Bar = 200 μm . Adapted from [155].

The same study also revealed an increase in the amounts of elastin and collagen relative to other constituents in the membranes. This raises the question as to whether the increase in MXTC-S is due to an increase in membrane thickness or due to a change in xenon diffusivity caused by the compositional change of the septal walls.

Our result in a healthy human subject showed that MXTC-S decreased with increased ventilation volume. According to Eq. 4.6, the observed change of $0.6 \text{ ms}^{0.5}$ in MXTC-S¹ corresponds

¹Whole lung median for MXTC-S = $3.1 \text{ ms}^{0.5}$ at low lung volume, whereas at TLC whole lung median MXTC-S =

to a change in septal wall thickness by 1.1 μm . Since the two measurements were obtained in the same subject at two different lung volumes, the change in MXTC-S must be solely due to a thinning of the septal wall at TLC. This results demonstrates that MXTC-S is capable of detecting subtle changes in septal wall thickness. Now, comparing the mean of MXTC-S for all disease subjects (C1, C2, A1) to the mean of MXTC-S for three healthy subjects (H1-H3) we observe a change of $0.9 \text{ ms}^{0.5}$ in MXTC-S² corresponding to 1.6 μm . However whether this change in MXTC-S is solely due to a change in septal wall thickness or whether a change in wall composition altering the diffusion constant contributes to the elevation of MXTC-S in certain lung diseases cannot be determined with the current implementation of MXTC. Elevated levels of elastin and collagen in the diseased lung tissue could indicate a repair process and might impact the effective xenon diffusion constant. Nevertheless, a more likely conclusion is that increased MXTC-S corresponds to septal wall thickening, indicating parenchymal inflammation, which is known to be a consistent finding in COPD and asthma [2]. Studies in a larger subject population, as well as in animal models with accompanying histology, are required to further investigate the relationship between the MXTC-S parameter and lung microstructure. However, it is already apparent from this study that the regional mapping of MXTC-S has the potential to become a powerful biomarker to non-invasively monitor disease progression and/or response to treatment by characterizing parenchymal inflammation and/or lung remodeling. To our knowledge, no other means of non-invasively estimating regional septal wall thickness or composition exist.

MXTC Compared to Direct Dissolved-Phase Imaging

MXTC-F and direct dissolved-phase imaging do not measure the same physiological parameters since there are differences in the contrast mechanisms of these two techniques. In both methods

2.5 $\text{ms}^{0.5}$, subject H3 in Table 4.3

²Mean for MXTC-S for three disease subjects (C1, C2, A1) = 4.2 $\text{ms}^{0.5}$, and mean for MXTC-S for three healthy subjects (H1, H2, H3) = 3.3 $\text{ms}^{0.5}$, Table 4.4

contrast generation is based on the property of xenon to dissolve in lung tissues. Nevertheless, in MXTC MR the image contrast stems from the exchange of xenon atoms between the dissolved phase and the alveolar airspaces. Therefore, it only reflects parenchymal structures that are directly involved in the gas exchange. On the other hand, the DP ratio contrast does not only involve xenon exchange but also incorporates xenon accumulation downstream in the pulmonary venous blood pool [25], which introduces an additional perfusion weighting. Thus, the dissolved-phase imaging contrast stems from HXe uptake. The relative weighting of perfusion (xenon accumulating in the downstream blood flow) versus gas exchange (xenon diffusing in and out of respiratory membranes at gas exchange sites) contributing to the dissolved-phase imaging contrast strongly depends on the relationship of $T2^*$ relaxation of HXe in the dissolved phase and imaging parameters such as flip angle, TR and TE [25] [156] [157]. Although the AP-slope of MXTC-F in subject C1 was not significantly positive, the AP-slope for MXTC-S was found to be very similar to the slope for DP (AP-slope = 1.72 %/cm, $p = 0.006$, Table 4.4). As discussed earlier, MXTC-S probes thickness and composition of respiratory membranes. These include thin structures ($\sim 1\text{-}2\ \mu\text{m}$) that do not contain capillaries as well as thicker structures ($\sim 10\ \mu\text{m}$) that do contain capillaries. The voxel value is an average of different types of structures. Hence, an increased MXTC-S parameter together with the increased DP ratio in the anterior partitions of subject C1 could indicate capillary recruitment accompanying increased perfusion as a result of parenchymal inflammation.

Limitations and Future Work

A limitation in the current implementation of MXTC is that, due to insufficiently available transmit power on our 3T scanner, only a maximum flip angle of 75° could be applied for the 3-ms Gaussian contrast-generating RF pulses. However, in order to completely saturate the dissolved phase, shorter-duration 90° flip angles are ideally required. Our attempt to correct for this effect, by comparing 75° and 90° spectroscopy-based XTC results and deriving a constant correction factor, is

prone to error. Therefore, we did not attempt to derive absolute results for tissue to alveolar-volume ratio and wall thickness from the MXTC parameters in this study. We further note that the uncertainty in the correction factor does not affect the main findings of this preliminary study, since data for all subjects were obtained and analyzed in the same way, and the main findings are a relative increase of the time constant for diseased subjects compared to that for healthy subjects, and the regional correlation among different imaging techniques. In future studies, absolute determination of the tissue to alveolar-volume ratio and wall thickness can be achieved by addressing the flip-angle limitation. There are several possibilities based on either a hardware solution, e.g. by implementing a more powerful broadband RF amplifier for hyperpolarized-gas studies, or on a software solution, e.g. by focusing on selective MXTC, which selectively encodes xenon gas exchange for tissue and blood resonances, as described in [65]. The higher spectral selectivity requires longer RF pulses, which will allow a 90° flip angle to be achieved with our current hardware.

In the current implementation, MXTC is a multi-breath experiment. It is therefore prone to spatial-registration errors secondary to different breath-hold positions. This issue can be addressed in future studies by implementing image-registration algorithms in the data analysis workflow [158]. It is also possible that only two XTC contrasts at two different delay times may be sufficient to derive a difference parameter, instead of the xenon exchange-time constant parameter MXTC-S, having equivalent diagnostic value for characterizing disease-induced changes in the alveolar wall. This would make MXTC a single breath-hold technique, which not only has the benefit of eliminating spatial-registration errors, but is also important for clinical application.

4.5.5 Conclusions

Multiple exchange time xenon polarization transfer contrast (MXTC) is an implementation of the xenon polarization transfer contrast (XTC) MRI technique in three dimensions and for multiple exchange times. Regional and dynamic encoding of the xenon exchange contrast enables the map-

ping of functional septal thickness in addition to the tissue-to-alveolar-volume ratio already derived from single exchange time XTC. Our results quantifying microstructure deformation of the healthy lung in response to gravity-induced tissue compression and ventilation volume demonstrate the sensitivity of the MXTC technique. Further, only structures participating in gas exchange are represented in the MXTC data. Therefore, MXTC-derived parameters describe a functional subset of microstructure. As a consequence, the MXTC image contrast is potentially very sensitive to pathological alterations of the lung parenchyma that affect gas exchange and is not masked by larger lung structures such as major blood vessels or airways.

This work demonstrates the first in vivo simultaneous mapping of lung microstructure parameters related to the tissue to alveolar-volume ratio and septal wall thickness in human subjects. Our preliminary results have shown that functional tissue volume mapping with MXTC-F exhibits excellent correlation with HXe ADC MRI and with lung-tissue attenuation assessed by CT in one COPD subject with emphysematous tissue destruction. Furthermore, we demonstrated that the new microstructure parameter MXTC-S, which is proportional to the functional septal wall thickness, was elevated in subjects with lung disease. We therefore propose that MXTC-S could become a novel biomarker to characterize parenchymal inflammation or thickening with clinical applications to non-invasively monitor disease progression or treatment response. By quantifying two functional lung parameters, MXTC provides a more comprehensive picture of lung microstructure than existing imaging techniques, and could become an important non-invasive and quantitative tool to characterize pulmonary disease phenotypes.

CHAPTER 5

CONCLUSIONS

There is a critical need for functional imaging modalities to diagnose and monitor pulmonary disease. CT is an imaging technique which presents excellent representation of structure. However, information about lung function can be obtained only indirectly, using empirically derived structure-function relationships [44]. In addition the significant radiation dose accompanying a high resolution CT scan prevents frequent use to monitor disease progression in longitudinal follow-up studies or general application in young patients. Lung function imaging is provided by lung scintigraphy which obtains ventilation and perfusion maps. However resolution in lung scintigraphy is very low and only 2D projection data is provided. MRI can provide functional information but MRI of the lung is challenging due to the low proton density and rapid signal dephasing due to susceptibility gradients caused by numerous tissue-air interfaces in the lung.

Hyperpolarized noble gases ^3He and ^{129}Xe are non-invasive contrast agents for lung MRI. Numerous acquisition modalities exist for imaging of lung structure and function. Especially the unique property of HXe to dissolve in lung tissues can be exploited to develop functional imaging methods related to gas-exchange efficiency and impairment in lung disease. Prior to this work, the regional description of lung function parameters was limited by restrictions in image acquisition time and the low SNR of HXe in the dissolved phase.

This thesis addressed challenges in image acquisition speed and SNR by introducing parallel imaging to HXe imaging. Parallel imaging in hyperpolarized gas applications allows faster image acquisition without loss in SNR. A 32-channel phased-array receive RF coil for the human chest was

developed tuned to the resonance frequency of HXe at 3T. Further an asymmetric birdcage transmit coil was integrated to address the need of a homogeneous excitation field to prevent bias in the image contrast by regionally varying spin excitation. First results of spin density imaging in healthy human subjects and subjects with lung disease demonstrated the significant improvement in image quality by achieving high resolution ventilation images with excellent SNR. Transmit field maps showed regional variation of less than 10% across the whole lung. Parallel imaging performance of the phased-array coil was demonstrated by achieving acceleration factors up to three in 2D acquisitions and up to six in 3D acquisitions while remaining aliasing artifacts were negligible.

The newly developed human chest coil enabled the implementation of the multiple exchange time xenon polarization transfer contrast (MXTC) method, which is based on XTC initially demonstrated by Ruppert et al [26] [27] [28] and first implemented in human subjects by Patz et al [23]. The original features of MXTC are the extension of the initial two dimensional projection implementation to three dimensions and to dynamic encoding. The dynamic encoding allowed for two parameters to be derived regionally which are related to gas-exchange functionality by characterizing the tissue-to-alveolar-volume ratio and the alveolar wall thickness.

Parameter mapping in human subjects and rabbits showed that MXTC is capable of an assessment of healthy lung physiology demonstrating posture and lung inflation dependence of lung microstructure. Further by comparing to literature values we found that MXTC estimation of relative tissue volume is lower than estimates derived from histology. This finding can be explained by the fact that MXTC-derived parameters reflect only those structures that are involved in gas exchange and thus represent a functional subset of lung structures. The pure functional contrast of MXTC makes it a modality with specific sensitivity to disease-initiated structural remodeling that affects the gas exchange capability of the lung.

Our results in subjects with lung disease showed that the MXTC-derived functional tissue density parameter exhibited excellent agreement with other imaging techniques which are sensitive to

tissue density (CT) or which reflect airspace size (HXe ADC). The newly developed dynamic parameter, which characterizes the alveolar wall, was elevated in subjects with lung disease, most likely indicating parenchymal inflammation. In light of these observations we believe that MXTC has potential as an important biomarker for the regional quantification of emphysematous tissue destruction in COPD (using the tissue density parameter) and of parenchymal inflammation or thickening (using the wall thickness parameter). By simultaneously quantifying two lung function parameters, MXTC provides a more comprehensive picture of lung microstructure than existing lung imaging techniques and could become an important non-invasive and quantitative tool to characterize pulmonary disease phenotypes.

In future work a phased-array RF coil double tuned to the resonances of HXe and protons will allow new acquisition strategies to address remaining challenges such as motion and image registration. By interleaving proton and HXe image encoding subject motion can be registered on proton images to correct HXe images.

In regard to the MXTC method in this implementation the dissolved phase of HXe was considered as a whole without distinction between blood and tissue compartment. However important physiological information can be obtained by selectively probing the two compartments. For example, Driehuys et al showed that the ratio of blood and tissue signal can be a sensitive probe of gas transfer impairment [18].

Animal studies with accompanying histology could be used to further validate results and especially to accurately determine the diffusion constant of HXe in respective dissolved-phase compartments to reduce the uncertainty in parameter estimation.

APPENDICES

APPENDIX A

DIFFUSION EQUATION OF HEAT CONDUCTION TYPE WITH DIRICHLET BOUNDARY CONDITIONS

The 1-D diffusion equation, describing diffusion of magnetization concentration into a slab of tissue

$$\frac{\partial C}{\partial t} = D \frac{\partial^2 C}{\partial x^2} \quad (\text{A.1})$$

The solution is obtained by separation of variables

$$C(x,t) = T(t)u(x) \quad (\text{A.2})$$

with

$$T(t) = e^{-\lambda t} \quad (\text{A.3a})$$

$$u(x) = a \cos \omega x + b \sin \omega x \quad (\text{A.3b})$$

$$\text{with } D = \frac{\lambda}{\omega^2} \quad (\text{A.3c})$$

Dirichlet boundary conditions are

$$C(0,t) = C(L,t) = 0 \quad (\text{A.4a})$$

$$C(x,0) = c \quad (\text{A.4b})$$

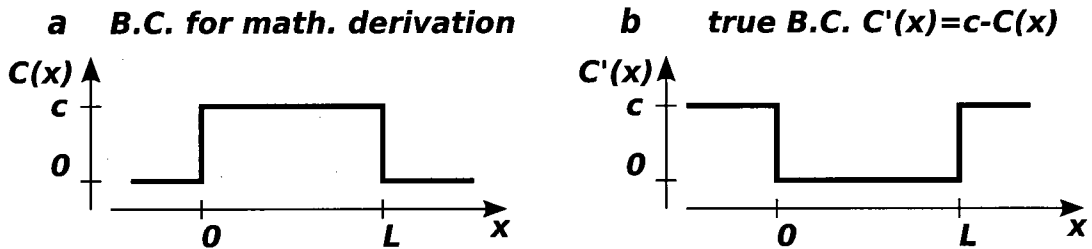


Figure A-1: Boundary conditions for mathematical derivation (a) and for xenon-129 initial magnetization (b)

Then the solution is given by $c - C(x,t)$, since for the case of ideal RF saturation initially all magnetization is in the gas phase and the magnetization within the slab is zero.

From the boundary conditions for $x = 0$ and $x = L$ we obtain

$$a = 0 \quad (\text{A.5a})$$

$$\omega = \frac{n\pi}{L} \quad (\text{A.5b})$$

The common solution is given by linear superposition

$$C(x,t) = \sum_{i=0}^{\infty} a_n \cdot e^{-D(\frac{n\pi}{L})^2 t} \cdot \sin\left(\frac{n\pi}{L}x\right) \quad (\text{A.6})$$

From the boundary condition for $t = 0$ we have

$$c = \sum_{i=0}^{\infty} a_n \cdot \sin\left(\frac{n\pi}{L}x\right) \quad (\text{A.7})$$

The coefficients a_n are obtained by using the orthogonality of the basis functions $\int \sin\left(\frac{n\pi}{L}x\right) \sin\left(\frac{m\pi}{L}x\right) = \delta_{mn}$ and normalization $\int_0^L (\sin\left(\frac{n\pi}{L}x\right))^2 = \frac{L}{2}$

$$a_n = \frac{2}{L} \int_0^L c \sin\left(\frac{n\pi}{L}x\right) dx = -\frac{2c}{n\pi} (\cos n\pi - 1) \quad (\text{A.8a})$$

$$\Rightarrow n = 2k + 1 \Rightarrow a_k = \frac{4c}{(2k + 1)\pi} \quad \text{with } k = 0, 1, \dots, \infty \quad (\text{A.8b})$$

giving for the concentration

$$C(x,t) = \sum_{k=0}^{\infty} \frac{4c}{(2k + 1)\pi} \cdot e^{-D(\frac{(2k+1)\pi}{L})^2 t} \cdot \sin\left(\frac{(2k+1)\pi}{L}x\right) \quad (\text{A.9})$$

To obtain the signal S which is proportional to the magnetization M , the magnetization concentration C' (Figure A-1) has to be integrated over the tissue thickness

$$S \propto M = cL - \int_0^L C(x,t) dx = cL - \sum_{k=0}^{\infty} \frac{4c}{(2k + 1)\pi} \cdot e^{-D(\frac{(2k+1)\pi}{L})^2 t} \cdot \frac{2L}{(2k + 1)\pi} \quad (\text{A.10})$$

We obtain the solution for the xenon-129 signal in the dissolved phase at exchange time t :

$$S_{diss}(t) \propto M_{diss}(t) = cL \left(1 - \sum_{k=0}^{\infty} \frac{8}{((2k + 1)\pi)^2} \cdot e^{-D(\frac{(2k+1)\pi}{L})^2 t} \right) \quad (\text{A.11})$$

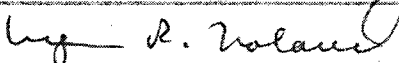
APPENDIX B

FREQUENTLY USED ABBREVIATIONS

TLC	Total Lung Capacity
RV	Residual Volume
VC	Vital Capacity
PFT	Pulmonary Function Test
COPD	Chronic Obstructive Pulmonary Disease
CT	Computed Tomography
S/V	Surface to Volume Ratio
MRI	Magnetic Resonance Imaging
NMR	Nuclear Magnetic Resonance
RF	Radio Frequency
B_1	transverse RF field
B_0	longitudinal external field
HHe	Hyperpolarized Helium-3
HXe	Hyperpolarized Xenon-129
XTC	Xenon Polarization Transfer Contrast
MXTC	Multiple Exchange Time Xenon Polarization Transfer Contrast
ADC	Apparent Diffusion Coefficient
DP	Dissolved Phase
GRAPPA	Generalized Autocalibrating Partially Parallel Acquisitions
SENSE	Sensitivity Encoding

APPENDIX C
IRB HUMAN PROTOCOL APPROVAL

**University of Virginia
Institutional Review Board for Health Sciences Research
Protection of Human Subjects Approval
Assurance Identification/Certification/Declaration
(Common Federal Rule)**

HSR # 13740		
Event: Approval Protocol Continuation - Full Committee	Type: Protocol	Sponsor(s): Sponsor Protocol #: Principal Investigator: Talissa Altes, MD
Title: Hyperpolarized Xenon-129 MR imaging of the Lung		
Assurance: Federal Wide Assurance (FWA)#: 00006183		
Certification of IRB Review: The IRB-HSR abides by 21CFR50, 21CFR56, 45CFR46, 45CFR160, 45CFR164, 32CFR219 and ICH guidelines. This activity has been reviewed and approved by the IRB in accordance with these regulations.		
Approval Date: 06/09/09 Protocol Expiration Date: 06/08/10 Approved to Enroll 110 subjects. HSR Protocol Version Date: 05/06/09 Sponsor Protocol Version Date: 06/24/08 Investigator Brochure Version Date: Investigator-Initiated Protocol Version Date: Pending IRB Protocol Version Date:	Comments: Modification expedited: Minimal Risk/Minor Changes - enrollment increased to 110.	
Current Status: Open to enrollment		
Consent Version Dates: Adult Consent Form -- 05/06/2009		
Committee Members (did not vote):		
<small>The official signing below certifies that the information provided above is correct and that, as required, future reviews will be performed and certification will be provided.</small>		
Name: Lynn R. Noland , RN PhD Title: Vice Chair, Institutional Review Board for Health Sciences Research Phone: 434-924-9634 Fax: 434-924-2932	Name and Address of Institution: Institutional Review Board for Health Sciences Research PO Box 800483 University of Virginia Charlottesville, VA 22908	
Signature: 	Date: 6/15/09	

© 2009 by the Rector and Visitors of the University of Virginia. All rights reserved.

BIBLIOGRAPHY

- [1] Rabe KF, Hurd S, Anzueto A, Barnes PJ, Buist SA, Calverley P, Fukuchi Y, Jenkins C, Rodriguez-Roisin R, van Weel C, Zielinski J and for Chronic Obstructive Lung Disease GI. Global strategy for the diagnosis, management, and prevention of chronic obstructive pulmonary disease: GOLD executive summary. *Am J Respir Crit Care Med* 176(6):532–555, 2007.
- [2] Croxton TL, GG W, S RM and JR H. Future research directions in chronic obstructive pulmonary disease. *Am J Respir Crit Care Med* 165:838–844, 2002.
- [3] Albert MS, Cates GD, Driehuys B, Happer W, Saam B, Springer CS and Wishnia A. Biological magnetic resonance imaging using laser-polarized ^{129}Xe . *Nature* 370(6486):199–201, 1994.
- [4] Kauczor HU, Hofmann D, Kreitner KF, Nilgens H, Surkau R, Heil W, Potthast A, Knopp MV, Otten EW and Thelen M. Normal and abnormal pulmonary ventilation: visualization at hyperpolarized He-3 MR imaging. *Radiology* 201(2):564–568, 1996.
- [5] Mugler JP, Driehuys B, Brookeman JR, Cates GD, Berr SS, Bryant RG, Daniel TM, de Lange EE, Downs JH, Erickson CJ, Happer W, Hinton DP, Kassel NF, Maier T, Phillips CD, Saam BT, Sauer KL and Wagshul ME. MR imaging and spectroscopy using hyperpolarized ^{129}Xe gas: preliminary human results. *Magn Reson Med* 37(6):809–815, 1997.
- [6] Altes TA, Powers PL, Knight-Scott J, Rakes G, Platts-Mills TA, de Lange EE, Alford BA, Mugler JP and Brookeman JR. Hyperpolarized ^3He MR lung ventilation imaging in asthmatics: preliminary findings. *J Magn Reson Imaging* 13(3):378–384, 2001.
- [7] van Beek EJR, Hill C, Woodhouse N, Fichele S, Fleming S, Howe B, Bott S, Wild JM and Taylor CJ. Assessment of lung disease in children with cystic fibrosis using hyperpolarized 3-helium MRI: comparison with shwachman score, chrispin-norman score and spirometry. *Eur Radiol* 17(4):1018–1024, 2007.
- [8] Salerno M, de Lange EE, Altes TA, Truwit JD, Brookeman JR and Mugler JP. Emphysema: hyperpolarized helium 3 diffusion MR imaging of the lungs compared with spirometric indexes—initial experience. *Radiology* 222(1):252–260, 2002.
- [9] van Beek EJR, Dahmen aM, Stavngaard T, Gast KK, Heussel CP, Krummenauer F, Schmiedeskamp J, Wild JM, Sjøgaard LV, Morbach aE, Schreiber LM and Kauczor HU. Hyperpolarised ^3He MRI versus hrct in copd and normal volunteers: Phil trial. *The European respiratory journal : official journal of the European Society for Clinical Respiratory Physiology* 34(6):1311–21, 2009.
- [10] Fain SB, Panth SR, Evans MD, Wentland AL, Holmes JH, Korosec FR, O'Brien MJ, Fontaine H and Grist TM. Early emphysematous changes in asymptomatic smokers: detection with ^3He MR imaging. *Radiology* 239(3):875–883, 2006.

- [11] Yablonskiy DA, Sukstanskii AL, Leawoods JC, Gierada DS, Bretthorst GL, Lefrak SS, Cooper JD and Conradi MS. Quantitative in vivo assessment of lung microstructure at the alveolar level with hyperpolarized ^3He diffusion MRI. *Proc Natl Acad Sci USA* 99(5):3111–3116, 2002.
- [12] Eberle B, Weiler N, Markstaller K, Kauczor H, Deninger A, Ebert M, Grossmann T, Heil W, Lauer LO, Roberts TP, Schreiber WG, Surkau R, Dick WF, Otten EW and Thelen M. Analysis of intrapulmonary $\alpha(2)$ concentration by MR imaging of inhaled hyperpolarized helium-3. *J Appl Physiol* 87(6):2043–2052, 1999.
- [13] Deninger AJ, Eberle B, Ebert M, Grossmann T, Heil W, Kauczor H, Lauer L, Markstaller K, Otten E, Schmiedeskamp J, Schreiber W, Surkau R, Thelen M and Weiler N. Quantification of regional intrapulmonary oxygen partial pressure evolution during apnea by ^3He MRI. *J Magn Reson* 141(2):207–216, 1999.
- [14] Goto T, Suwa K, Uezono S, Ichinose F, Uchiyama M and Morita S. The blood-gas partition coefficient of xenon may be lower than generally accepted. *Br J Anaesth* 80(2):255–256, 1998.
- [15] Miller KW, Reo NV, Uiterkamp AJS, Stengle DP, Stengle TR and Williamson KL. Xenon NMR: chemical shifts of a general anesthetic in common solvents, proteins, and membranes. *Proc Natl Acad Sci USA* 78(8):4946–4949, 1981.
- [16] Bifone a, Song YQ, Seydoux R, Taylor RE, Goodson BM, Pietrass T, Budinger TF, Navon G and Pines a. NMR of laser-polarized xenon in human blood. *Proc Natl Acad Sci USA* 93(23):12932–6, 1996.
- [17] Wagshul ME, Button TM, Li HF, Liang Z, Springer CS, Zhong K and Wishnia A. In vivo MR imaging and spectroscopy using hyperpolarized ^{129}Xe . *Magn Reson Med* 36(2):183–191, 1996.
- [18] Driehuys B, Cofer GP, Pollaro J, Mackel JB, Hedlund LW and Johnson GA. Imaging alveolar-capillary gas transfer using hyperpolarized ^{129}Xe MRI. *Proc Natl Acad Sci USA* 103(48):18278–18283, 2006.
- [19] Ruppert K, Brookeman JR, Hagspiel KD, Driehuys B and Mugler III JP. NMR of hyperpolarized ^{129}Xe in the canine chest: spectral dynamics during a breath-hold. *NMR in biomedicine* 13(4):220–8, 2000.
- [20] Butler JP, Mair RW, Hoffmann D, Hrovat MI, Rogers Ra, Topulos GP, Walsworth RL and Patz S. Measuring surface-area-to-volume ratios in soft porous materials using laser-polarized xenon interphase exchange nuclear magnetic resonance. *Journal of physics Condensed matter : an Institute of Physics journal* 14(13):L297–304, 2002.
- [21] Månsson S, Wolber J, Driehuys B, Wollmer P and Golman K. Characterization of diffusing capacity and perfusion of the rat lung in a lipopolysaccharide disease model using hyperpolarized ^{129}Xe . *Magn Reson Med* 50(6):1170–1179, 2003.
- [22] Abdeen N, Cross A, Cron G, White S, Rand T, Miller D and Santyr G. Measurement of xenon diffusing capacity in the rat lung by hyperpolarized ^{129}Xe MRI and dynamic spectroscopy in a single breath-hold. *Magn Reson Med* 264:255–264, 2006.

- [23] Patz S, Muradian I, Hrovat MI, Ruset IC, Topulos G, Covrig SD, Frederick E, Hatabu H, Hersman FW and Butler JP. Human pulmonary imaging and spectroscopy with hyperpolarized ^{129}Xe at 0.2 T. *Acad Radiol* 15(6):713–727, 2008.
- [24] Cleveland ZI, Cofer GP, Metz G, Beaver D, Nouis J, Kaushik S, Kraft M, Wolber J, Kelly KT, McAdams HP and Driehuys B. Hyperpolarized ^{129}Xe MR imaging of alveolar-capillary gas transfer in human volunteers. In: *Proceedings of the 18th Scientific Meeting of ISMRM, Stockholm, Sweden*, page p. 196, 2010.
- [25] Mugler III JP, Altes TA, Ruset IC, Dregely IM, Mata JF, Miller GW, Ketel S, Ketel Jf, Hersman FW and Ruppert K. Simultaneous imaging of ventilation distribution and gas exchange in the human lung using hyperpolarized Xe-129 MRI. In: *Proceedings of the 18th Scientific Meeting of ISMRM, Stockholm, Sweden*, page p. 197, 2010.
- [26] Ruppert K, Brookeman J, Hagspiel K and Mugler III J. Probing lung physiology with xenon polarization transfer contrast (XTC). *Magn Reson Med* 44(3):349357, 2000.
- [27] Ruppert K, Mata JF, Brookeman JR, Hagspiel KD and Mugler JP. Exploring lung function with hyperpolarized ^{129}Xe nuclear magnetic resonance. *Magn Reson Med* 51(4):676–687, 2004.
- [28] Ruppert K, Mata JF, Wang HTJ, Tobias WA, Cates GD, Brookeman JR, Hagspiel KD and Mugler JP. XTC MRI: sensitivity improvement through parameter optimization. *Magn Reson Med* 57(6):1099–1109, 2007.
- [29] Ruset IC, Ketel S and Hersman FW. Optical pumping system design for large production of hyperpolarized ^{129}Xe . *Phys Rev Lett* 96(5):053002, 2006.
- [30] Weibel ER. *Morphometry of the human lung*. Springer Verlag, 1963.
- [31] Mandelbrot B. *The Fractal Geometry of Nature*. W.H. Freeman, 1983.
- [32] Weibel ER and H E. *Quantitative Methods in Morphology*. Springer Verlag, Berlin-Heidelberg-New York, 1967.
- [33] Hess W. Das Prinzip des kleinsten Kraftverbrauches im Dienste haemodynamischer Forschung. *Archiv fuer Anatomie und Physiologie Physiologische Abteilung* 1914.
- [34] Murray C. The physiological principle of minimum work. I. the vascular system and the cost of blood. *Proc Natl Acad Sci USA* 12:207–214, 1926.
- [35] Mauroy B, Filoche M, Weibel ER and Sapoval B. An optimal bronchial tree may be dangerous. *Nature* 427(6975):633–6, 2004.
- [36] Weibel ER. What makes a good lung? *Swiss medical weekly : official journal of the Swiss Society of Infectious Diseases, the Swiss Society of Internal Medicine, the Swiss Society of Pneumology* 139(27-28):375–86, 2009.
- [37] Gehr P, Bachofen M and Weibel ER. The normal human lung: ultrastructure and morphometric estimation of diffusion capacity. *Respir Physiol* 32(2):121–140, 1978.
- [38] Weibel ER, Federspiel WJ, Fryder-Doffey F, Hsia CC, König M, Stalder-Navarro V and Vock R. Morphometric model for pulmonary diffusing capacity. i. membrane diffusing capacity. *Respiration physiology* 93(2):125–49, 1993.

- [39] West JB. *Respiratory Physiology: The Essentials*. Lippincott Williams & Wilkins; Seventh Edition, 2005.
- [40] Jeffery PK. Remodeling in asthma and chronic obstructive lung disease. *Am J Respir Crit Care Med* 164(10 Pt 2):S28–S38, 2001.
- [41] West J. *Pulmonary Pathophysiology: The Essentials*. Lippincott Williams & Wilkins; Seventh Edition, 2008.
- [42] Snider G, Kleinerman J, Thurlbeck W and Bengally Z. Definition of emphysema. report of the national heart, lung and blood institute, division of lung diseases. *Am Rev Respir Dis* 132:182–185, 1985.
- [43] Gevenois P, de Maertelaer V, P DV, J Z and JC Y. Comparison of computed density and macroscopic morphometry in pulmonary emphysema. *Am J Respir Crit Care Med* 152:653–7, 1995.
- [44] Coxson HO, Rogers RM, Whittall KP, D'yachkova Y, Paré PD, Sciruba FC and Hogg JC. A quantification of the lung surface area in emphysema using computed tomography. *Am J Respir Crit Care Med* 159(3):851–6, 1999.
- [45] Togao O, Tsuji R, Ohno Y, Dimitrov I and Takahashi M. Ultrashort echo time (ute) MRI of the lung: Assessment of tissue density in the lung parenchyma. *Magn Reson Med* 2010.
- [46] Fink C, Puderbach M, Bock M, Lodemann KP, Zuna I, Schmhl A, Delorme S and Kauczor HU. Regional lung perfusion: assessment with partially parallel three-dimensional MR imaging. *Radiology* 231(1):175–184, 2004.
- [47] Edelman RR, Hatabu H, Tadamura E, Li W and Prasad PV. Noninvasive assessment of regional ventilation in the human lung using oxygen-enhanced magnetic resonance imaging. *Nat Med* 2(11):1236–1239, 1996.
- [48] Bauman G, Puderbach M, Deimling M, Jellus V, Chefd'hotel C, Dinkel J, Hintze C, Kauczor HU and Schad LR. Non-contrast-enhanced perfusion and ventilation assessment of the human lung by means of fourier decomposition in proton MRI. *Magn Reson Med* 62(3):656–64, 2009.
- [49] Bloch F, Hansen W and Packard M. Nuclear induction. *Phys Rev* 69:127, 1946.
- [50] Purcell EM, Torrey H and Pound R. Resonance absorption by nuclear magnetic moments in a solid. *Phys Rev* 69:37, 1946.
- [51] Hoult DI and Richards RE. The signal-to-noise ratio of the nuclear magnetic resonance experiment. *J Magn Reson* 24:71–85, 1976.
- [52] Hoult DI. The principle of reciprocity in signal strength calculations - a mathematical guide. *Concepts In Magn Reson* 12:173–187, 2000.
- [53] Haacke EM, Brown RW, Thompson MR and Venkatesan R. *Magnetic Resonance Imaging: Physical Principles and Sequence Design*. John Wiley & Sons, Inc., 1999.
- [54] Stadler A, Jakob PM, Griswold M, Barth M and Bankier AA. T_1 mapping of the entire lung parenchyma: Influence of the respiratory phase in healthy individuals. *J Magn Reson Imaging* 21(6):759–764, 2005.

- [55] Bottomley PA, Hardy CJ, Argersinger RE and Allen-Moore G. A review of 1h nuclear magnetic resonance relaxation in pathology: are T_1 and T_2 diagnostic? *Med Phys* 14(1):1–37, 1987.
- [56] Pracht ED, Arnold JFT, Wang T and Jakob PM. Oxygen-enhanced proton imaging of the human lung using T_2 . *Magn Reson Med* 53(5):1193–1196, 2005.
- [57] Coxson HO, Mayo JR, Behzad H, Moore BJ, Verburt LM, Staples CA, Par PD and Hogg JC. Measurement of lung expansion with computed tomography and comparison with quantitative histology. *J Appl Physiol* 79(5):1525–1530, 1995.
- [58] Ebert M, Grossmann T, Heil W, Otten WE, Surkau R, Leduc M, Bachert P, Knopp MV, Schad LR and Thelen M. Nuclear magnetic resonance imaging with hyperpolarised helium-3. *Lancet* 347(9011):1297–1299, 1996.
- [59] Bachert P, Schad LR, Bock M, Knopp MV, Ebert M, Grossmann T, Heil W, Hofmann D, Surkau R and Otten EW. Nuclear magnetic resonance imaging of airways in humans with use of hyperpolarized ^3He . *Magn Reson Med* 36(2):192–196, 1996.
- [60] MacFall JR, Charles HC, Black RD, Middleton H, Swartz JC, Saam B, Driehuys B, Erickson C, Happer W, Cates GD, Johnson GA and Ravin CE. Human lung air spaces: potential for MR imaging with hyperpolarized He-3. *Radiology* 200(2):553–558, 1996.
- [61] Walker T and Happer W. Spin-exchange optical pumping of noble gas nuclei. *Rev Mod Phys* 69:629–642, 1997.
- [62] Altes TA, Mugler III JP, Dregely IM, Ketel S, Ruset IC, de Lange EE, Hersman FW and Ruppert K. Hyperpolarized xenon-129 ventilation MRI: Preliminary results in normal subjects and patients with lung disease. In: *Proceedings of the 18th Scientific Meeting of ISMRM, Stockholm, Sweden*, page p. 2529, 2010.
- [63] Thien F, Friese M, Cowin G, Maillet D, Wang D, Galloway G, Brereton I, Robinson PJ, Heil W and Thompson B. Feasibility of functional magnetic resonance lung imaging in australia with long distance transport of hyperpolarized helium from germany. *Respirology (Carlton, Vic)* 13(4):599–602, 2008.
- [64] Swanson SD, Rosen MS, Coulter KP, Welsh RC and Chupp TE. Distribution and dynamics of laser-polarized ^{129}Xe magnetization in vivo. *Magn Reson Med* 42(6):1137–45, 1999.
- [65] Ruppert K, Chang Y, Altes TA, Dregely IM, Ketel S, Ruset I, Mata JF, Hersman FW and Mugler III JP. Compartment-selective XTC MRI at 1.5 T and 3 T. In: *Proceedings of the 17th Scientific Meeting of ISMRM, Honolulu, Hawaii, USA* page p. 9, 2009.
- [66] Imai H, Kimura A, Ito T and Fujiwara H. Hyperpolarized ^{129}Xe dynamic study in mouse lung under spontaneous respiration: application to murine tumor b16bl6 melanoma. *Eur J Radiol* 73(1):196–205, 2010.
- [67] Harris R. Nuclear spin properties and notation. in: Grant dm, harris rk, editors. *Encyclopedia of nuclear magnetic resonance Chichester, UK: Wiley* pages 3301–4949, 1996.
- [68] Chen XJ, Miller HE, Chawla MS, Cofer GP, Driehuys B, Hedlund LW and Johnson GA. Spatially resolved measurements of hyperpolarized gas properties in the lung in vivo. part I: diffusion coefficient. *Magn Reson Med* 42(4):721–728, 1999.

- [69] Weathersby PK and Homer LD. Solubility of inert gases in biological fluids and tissues: a review. *Undersea Biomed Res* 7(4):277–296, 1980.
- [70] Seydoux R, Diehl P, RK M and J J. Chemical shifts in magnetic resonance of the ^3He nucleus in liquid solvents and comparison with other noble gases. *J Magn Reson A* 101:78–83, 1993.
- [71] Kauczor H, Surkau R and Roberts T. MRI using hyperpolarized noble gases. *Eur Radiol* 8(5):820–827, 1998.
- [72] Dabaghyan M, Dregely IM, Muradyan I, Hrovat MI, Hatabu H, Butler JP and Patz S. Oxygen partial pressure and uptake rate in the lung with hyperpolarized ^{129}Xe MRI: Preliminary results. In: *Proceedings of the 18th Scientific Meeting of ISMRM, Stockholm, Sweden*, page p. 987, 2010.
- [73] Kober F, Koenigsberg B, Belle V, Viallon M, Levieil JL, Delon A, Ziegler A and Dcorps M. NMR imaging of thermally polarized helium-3 gas. *J Magn Reson* 138(2):308–312, 1999.
- [74] Deppe MH, Parra-Robles J, Ajraoui S, Parnell SR, Clemence M, Schulte RF and Wild JM. Susceptibility effects in hyperpolarized ^3He lung MRI at 1.5 T and 3 T. *J Magn Reson Imaging* 30(2):418–423, 2009.
- [75] Mugler III JP, Dregely I, Altes TA, Ketel S, Ruset IC, Distelbrink JH, Chang Y, Mata JF, Hersman FW and Ruppert K. T_2^* for hyperpolarized Xe-129 in the healthy human lung at 1.5 T and 3 T. In: *Proceedings of the 17th Scientific Meeting of ISMRM, Honolulu, Hawaii, USA*, page p. 2207, 2009.
- [76] Guenther D, Eberle B, Hast J, Lill J, Markstaller K, Puderbach M, Schreiber WG, Hanisch G, Heussel CP, Surkau R, Grossmann T, Weiler N, Thelen M and Kauczor HU. ^3He MRI in healthy volunteers: preliminary correlation with smoking history and lung volumes. *NMR Biomed* 13(4):182–189, 2000.
- [77] Tzeng YS, Lutchen K and Albert M. The difference in ventilation heterogeneity between asthmatic and healthy subjects quantified using hyperpolarized ^3He MRI. *J Appl Physiol* 106(3):813–822, 2009.
- [78] Parraga G, McCormack DG, Etemad-Rezai R, Mathew L and Santyr GE. Hyperpolarized ^3He magnetic resonance imaging of ventilation defects in healthy elderly volunteers: initial findings at 3.0 tesla. *Academic radiology* 15(6):776–85, 2008.
- [79] Gast. Distribution of ventilation in lung transplant recipients evaluation by dynamic ^3He MRI with lung motion.pdf, 2003.
- [80] Holmes JH, Korosec FR, Du J, O'Halloran RL, Sorkness RL, Grist TM, Kuhlman JE and Fain SB. Imaging of lung ventilation and respiratory dynamics in a single ventilation cycle using hyperpolarized He-3 MRI. *J Magn Reson Imaging* 26(3):630–6, 2007.
- [81] Mugler III JP, Altes TA, Ruset IC, Ketel S, Distelbrink JH, Chang Y, Mata JF, Hersman FW, Ruppert K and Dregely IM. Hyperpolarized Xe-129 ventilation imaging using an optimized 3D steady-state free-precession pulse sequence. In: *Proceedings of the 17th Scientific Meeting of ISMRM, Honolulu, Hawaii, USA*, page p. 2210, 2009.

- [82] Salerno M, Altes TA, Brookeman JR, de Lange EE and Mugler JP. Rapid hyperpolarized ^3He diffusion MRI of healthy and emphysematous human lungs using an optimized interleaved-spiral pulse sequence. *J Magn Reson Imaging* 17(5):581–588, 2003.
- [83] Woods JC, Choong CK, Yablonskiy DA, Bentley J, Wong J, Pierce JA, Cooper JD, Macklem PT, Conradi MS and Hogg JC. Hyperpolarized ^3He diffusion MRI and histology in pulmonary emphysema. *Magn Reson Med* 56(6):1293–1300, 2006.
- [84] Parraga G, Ouriadov A, Evans A, McKay S, Lam WW, Fenster A, Etemad-Rezai R, McCormack D and Santyr G. Hyperpolarized ^3He ventilation defects and apparent diffusion coefficients in chronic obstructive pulmonary disease: preliminary results at 3.0 tesla. *Invest Radiol* 42(6):384–391, 2007.
- [85] Swift AJ, Wild JM, FICHELE S, Woodhouse N, Fleming S, Waterhouse J, Lawson RA, Paley MNJ and Beek EJR. Emphysematous changes and normal variation in smokers and copd patients using diffusion ^3He MRI. *Eur J Radiol* 54(3):352–358, 2005.
- [86] Salerno M, Brookeman JR, Lange EED, Knight-Scott J and Mugler III JP. Demonstration of an alveolar-size gradient in the healthy human lung: A study of the reproducibility of hyperpolarized ^3He diffusion MRI. In: *Proceedings of the 8th Scientific Meeting of ISMRM, Denver, Colorado, USA* page p. 2195, 2000.
- [87] FICHELE S, Woodhouse N, Swift AJ, Said Z, Paley MNJ, Kasuboski L, Mills GH, van Beek EJR and Wild JM. MRI of helium-3 gas in healthy lungs: posture related variations of alveolar size. *J Magn Reson Imaging* 20(2):331–335, 2004.
- [88] Evans A, McCormack D, Ouriadov A, Etemad-Rezai R, Santyr G and Parraga G. Anatomical distribution of ^3He apparent diffusion coefficients in severe chronic obstructive pulmonary disease. *J Magn Reson Imaging* 26(6):1537–47, 2007.
- [89] Sukstanskii AL and Yablonskiy DA. In vivo lung morphometry with hyperpolarized ^3He diffusion MRI: theoretical background. *J Magn Reson* 190(2):200–210, 2008.
- [90] Yablonskiy Da, Sukstanskii AL, Woods JC, Gierada DS, Quirk JD, Hogg JC, Cooper JD and Conradi MS. Quantification of lung microstructure with hyperpolarized ^3He diffusion MRI. *J Appl Physiol* 107(4):1258–65, 2009.
- [91] Carl M, Miller GW, Mugler JP, Rohrbach S, Tobias WA and Cates GD. Measurement of hyperpolarized gas diffusion at very short time scales. *J Magn Reson* 189(2):228–240, 2007.
- [92] Wang C, Miller GW, de Lange EE, Altes TA, Cates GD and Mugler JP. Time dependence of ^3He diffusion in the human lung: measurement in the long-time regime using stimulated echoes. *Magn Reson Med* 56(2):296–309, 2006.
- [93] Wang C, Altes Ta, Mugler JP, Miller GW, Ruppert K, Mata JF, Cates GD, Borish L and de Lange EE. Assessment of the lung microstructure in patients with asthma using hyperpolarized ^3He diffusion MRI at two time scales: comparison with healthy subjects and patients with copd. *J Magn Reson Imaging* 28(1):80–8, 2008.
- [94] O'Halloran RL, Holmes JH, Wu YC, Alexander A and Fain SB. Helium-3 MR q-space imaging with radial acquisition and iterative highly constrained back-projection. *Magn Reson Med* 63(1):41–50, 2010.

- [95] Wang C, Altes TA, Mugler III JP, de Lange EE, Ruppert K, Hersman FW, Dregely IM, Ruset IC, Ketel S and Verbanck S. Long-time-scale hyperpolarized ^3He and ^{129}Xe diffusion in human lungs: Experimental measurements and computer simulation. *In: Proceedings of the 18th Scientific Meeting of ISMRM, Stockholm, Sweden*, page p. 2541, 2010.
- [96] Wang C, Mugler III JP, de Lange EE, Ruppert K, Hersman FW, Dregely IM, Ruset IC, Ketel S and Altes TA. Measurement of the diffusion of hyperpolarized ^{129}Xe in human lungs over short and long time scales during one breath hold. *In: Proceedings of the 18th Scientific Meeting of ISMRM, Stockholm, Sweden*, page p. 2543, 2010.
- [97] Shapiro SD. Animal models for copd. *Chest* 117(5 Suppl 1):223S–227S, 2000.
- [98] Deninger AJ, Mnsson S, Petersson JS, Pettersson G, Magnusson P, Svensson J, Fridlund B, Hansson G, Erjefeldt I, Wollmer P and Golman K. Quantitative measurement of regional lung ventilation using ^3He MRI. *Magn Reson Med* 48(2):223–232, 2002.
- [99] Deninger AJ, Eberle B, Bermuth J, Escat B, Markstaller K, Schmiedeskamp J, Schreiber WG, Surkau R, Otten E and Kauczor HU. Assessment of a single-acquisition imaging sequence for oxygen-sensitive ^3He -MRI. *Magn Reson Med* 47(1):105–114, 2002.
- [100] Yu J, Rajaei S, Ishii M, Law M, Emami K, Woodburn JM, Kadlecsek S, Vahdat V and Rizi RR. Measurement of pulmonary partial pressure of oxygen and oxygen depletion rate with hyperpolarized helium-3 MRI: a preliminary reproducibility study on pig model. *Acad Radiol* 15(6):702–712, 2008.
- [101] Patz S, Hersman FW, Muradian I, Hrovat MI, Ruset IC, Ketel S, Jacobson F, Topulos GP, Hatabu H and Butler JP. Hyperpolarized ^{129}Xe MRI: a viable functional lung imaging modality? *Eur J Radiol* 64(3):335–344, 2007.
- [102] Miller GW, Mugler III JP, Altes TA, Dregely IM, Ruset IC, Ketel S, Ketel Jf, Hersman FW and Ruppert K. Motion-corrected pO₂ mapping in human lungs using hyperpolarized Xe-129 MRI. *In: Proceedings of the 18th Scientific Meeting of ISMRM, Stockholm, Sweden*, page p. 2558, 2010.
- [103] Chen XJ, Miller HE, Chawla MS, Cofer GP, Driehuys B, Hedlund LW, MacFall JR and Johnson GA. Spatially resolved measurements of hyperpolarized gas properties in the lung in vivo. part II: T₂^{*}. *Magn Reson Med* 42(4):729–737, 1999.
- [104] Deppe MH, Teh K, Parra-Robles J, Lee KJ and Wild JM. Slice profile effects in 2D slice-selective MRI of hyperpolarized nuclei. *J Magn Reson* 202(2):180–189, 2010.
- [105] Swanson SD, Rosen MS, Agranoff BW, Coulter KP, C R and Chupp E. Brain MRI with laser-polarized xenon. *Magnetic Resonance in Medicine* 38:695, 1997.
- [106] Muradian I, Patz S, Butler J, GP T, MI H, Covrig S, Ketel S, Ruset I and Hersman F. Hyperpolarized ^{129}Xe human pulmonary gas exchange with 3-point Dixon technique. *In: Proceedings of the 14th Annual Meeting of ISMRM, Seattle, WA, USA* page p. 862, 2006.
- [107] Kimura A, Wakayama T, Narazaki M, Kawata Y, Ueyama T and Fujiwara H. Improvement of T₁ determination of hyperpolarized ^{129}Xe in mouse brain under controlled-flow. *Magn Reson Med Sci* 3(4):199–205, 2004.

- [108] Kilian W, Seifert F and Rinneberg H. Dynamic NMR spectroscopy of hyperpolarized ^{129}Xe in human brain analyzed by an uptake model. *Magn Reson Med* 51(4):843–847, 2004.
- [109] Mugler JP, Altes TA, Ruset IC, Dregely IM, Mata JF, Miller GW, Ketel S, Ketel J, Hersman FW and Ruppert K. Simultaneous magnetic resonance imaging of ventilation distribution and gas uptake in the human lung using hyperpolarized xenon-129. *Proc Natl Acad Sci U S A* 2010.
- [110] Chang Y, Altes TA, Dregely I, Ketel S, Ruset IC, Mata JF, Hersman FW, Mugler JP and Ruppert K. Hyperpolarized ^{129}Xe MR of the sickle cell disease: preliminary findings. In: *Proceedings of the 17th Scientific Meeting of ISMRM, Honolulu, Hawaii, USA*, page p. 4385, 2009.
- [111] Roemer PB, Edelstein WA, Hayes CE, Souza SP and Mueller OM. The NMR phased array. *Magn Reson Med* 16(2):192–225, 1990.
- [112] Sodickson DK and Manning WJ. Simultaneous acquisition of spatial harmonics (SMASH): fast imaging with radiofrequency coil arrays. *Magn Reson Med* 38(4):591–603, 1997.
- [113] Jakob PM, Griswold MA, Edelman RR and Sodickson DK. Auto-SMASH: a self-calibrating technique for SMASH imaging. simultaneous acquisition of spatial harmonics. *MAGMA* 7(1):42–54, 1998.
- [114] Pruessmann KP, Weiger M, Scheidegger MB and Boesiger P. SENSE: sensitivity encoding for fast MRI. *Magn Reson Med* 42(5):952–962, 1999.
- [115] Griswold MA, Jakob PM, Nittka M, Goldfarb JW and Haase A. Partially parallel imaging with localized sensitivities (PILS). *Magn Reson Med* 44(4):602–609, 2000.
- [116] Griswold MA, Jakob PM, Heidemann RM, Nittka M, Jellus V, Wang J, Kiefer B and Haase A. Generalized autocalibrating partially parallel acquisitions (GRAPPA). *Magn Reson Med* 47(6):1202–1210, 2002.
- [117] Blaimer M, Breuer F, Mueller M, Heidemann RM, Griswold MA and Jakob PM. SMASH, SENSE, PILS, GRAPPA: how to choose the optimal method. *Top Magn Reson Imaging* 15(4):223–236, 2004.
- [118] Mugler III JP and Brookeman JR. Signal-to-noise considerations for parallel imaging with hyperpolarized gases. In: *Proceedings of the 13th Annual Meeting of ISMRM, Miami, Florida, USA*, page p. 485, 2005.
- [119] Lee RF, Johnson G, Grossman RI, Stoeckel B, Trampel R and McGuinness G. Advantages of parallel imaging in conjunction with hyperpolarized helium—a new approach to MRI of the lung. *Magn Reson Med* 55(5):1132–1141, 2006.
- [120] Lustig M, Donoho D and Pauly JM. Sparse MRI: The application of compressed sensing for rapid MR imaging. *Magn Reson Med* 58(6):1182–95, 2007.
- [121] Schmitt M, Potthast A, Sosnovik DE, Polimeni JR, Wiggins GC, Triantafyllou C and Wald LL. A 128-channel receive-only cardiac coil for highly accelerated cardiac MRI at 3 Tesla. *Magn Reson Med* 59(6):1431–1439, 2008.

- [122] Meise FM, Rivoire J, Terekhov M, Wiggins GC, Keil B, Karpuk S, Salhi Z, Wald LL and Schreiber LM. Design and evaluation of a 32-channel phased-array coil for lung imaging with hyperpolarized ^3He . *Magn Reson Med* 63(2):456–464, 2010.
- [123] Dregely IM, Wiggins GC, Ruset IC, Brackett J, Ketel S, Distelbrink J, Alagappan V, Mareyam A, Potthast A, Polimeni JR, Wald LL, Altes TA, Mugler JPI and Hersman FW. A 32 channel phased array lung coil for parallel imaging with hyperpolarized xenon ^{129}Xe at 3 T. In: *Proceedings of the 17th Scientific Meeting of ISMRM, Honolulu, Hawaii, USA*, page p. 4918, 2009.
- [124] Porea A, Teh K, M B, Berthel D, Weisser A, Hall I and Morris P. A dedicated coil configuration for Xe-129 imaging at 1.5 T. In: *Proceedings of the 18th Annual Meeting of ISMRM, Stockholm, Sweden*, page p. 4600, 2010.
- [125] Hayes CE, Edelstein WA, Schenck J, Mueller O and Eash M. An efficient, highly homogeneous radiofrequency coil for whole-body NMR imaging at 1.5 T. *J Magn Reson* 63:622–628, 1985.
- [126] De Zanche N, Chhina N, Teh K, Randell C, Pruessmann KP and Wild JM. Asymmetric quadrature split birdcage coil for hyperpolarized ^3He lung MRI at 1.5 T. *Magn Reson Med* 60(2):431–8, 2008.
- [127] Mispelter J, Lupu M and Briguët A. *NMR Probeheads for Biophysical and Biomedical Experiments*. Imperial College Press, 2006.
- [128] Leifer MC. Theory of the quadrature elliptic birdcage coil. *Magn Reson Med* 38(5):726–732, 1997.
- [129] Wiggins GC, Polimeni JR, Potthast A, Schmitt M, Alagappan V and Wald LL. 96-channel receive-only head coil for 3 Tesla: design optimization and evaluation. *Magn Reson Med* 62(3):754–762, 2009.
- [130] Polimeni JR and Wald LL. Documentation for icemghcoilarrayreconutil software 2007.
- [131] Meyer CH. Private communication .
- [132] Hersman FW, Ruset IC, Ketel S, Muradian I, Covrig SD, Distelbrink J, Porter W, Watt D, Ketel J, Brackett J, Hope A and Patz S. Large production system for hyperpolarized ^{129}Xe for human lung imaging studies. *Acad Radiol* 15(6):683–692, 2008.
- [133] Happer W, Miron E, Schaefer S, Schreiber D, van Wijngaarden WA and Zeng X. Polarization of the nuclear spins of noble-gas atoms by spin exchange with optically pumped alkali-metal atoms. *Phys Rev A* 29(6):3092–3110, 1984.
- [134] Cleveland ZI, Cofer GP, Metz G, Beaver D, Nouls J, Kaushik SS, Kraft M, Wolber J, Kelly KT, McAdams HP and Driehuys B. Hyperpolarized ^{129}Xe MR imaging of alveolar gas uptake in humans. *PLoS ONE* 5(8):e12192, 2010.
- [135] Dregely IM, Ruppert K, Mata JF, Altes TA, Ketel Jf, Ruset IC, Ketel S, Miller GW, Mugler III JP and Hersman FW. Lung microstructure changes in a rabbit after elastase instillation as detected with multiple exchange time XTC (MXTTC). In: *Proceedings of the 18th Scientific Meeting of ISMRM, Stockholm, Sweden*, page p. 2554, 2010.

- [136] Dregely IM, Ruset IC, Ketel Jf, Ketel S, Mata JF, Altes TA, Miller GW, Mugler III JP, Hersman FW and Ruppert K. The structural response of the compliant lung to different ventilation volumes assessed by multiple exchange time xenon transfer contrast (MXTC). *In: Proceedings of the 18th Scientific Meeting of ISMRM, Stockholm, Sweden*, page p. 2555, 2010.
- [137] Dregely I, Ruppert K, Altes TA, Ruset IC, Mugler JP and Hersman WF. Lung function imaging with hyperpolarized xenon MRI in asthmatics. *Am J Respir Crit Care Med* 181:1265, 2010.
- [138] Dregely I, Mugler JPI, Ruset IC, Altes TA, Mata JF, Miller GW, Ketel J, Ketel S, Distelbrink J, Hersman FW and Ruppert K. Hyperpolarized xenon-129 gas-exchange imaging of lung microstructure: First case studies in subjects with obstructive lung disease. *submitted to J Magn Reson Imaging* xx:xx, 2010.
- [139] Dregely I, CRuset I, Mata JF, Ketel J, Distelbrink J, Altes TA, III JPM, Hersman FW and Ruppert K. Hyperpolarized xenon-129 gas exchange imaging of lung microstructure: Preliminary results in healthy volunteers and rabbits. *submitted to Magn Reson Med* xx:xx, 2010.
- [140] Hrovat M, Muradian I, Frederick E, Butler J, Hatabu H and Patz S. Theoretical model for XTC (xenon transfer contrast) experiments with hyperpolarized ^{129}Xe . *In: Proceedings of the 18th Scientific Meeting of ISMRM, Stockholm, Sweden*, page p. 2556, 2010.
- [141] O'Halloran RL, Holmes JH, Altes TA, Salerno M and Fain SB. The effects of SNR on ADC measurements in diffusion-weighted hyperpolarized He-3 MRI. *J Magn Reson* 185(1):42–49, 2007.
- [142] Stocks J and Quanjer PH. Reference values for residual volume, functional residual capacity and total lung capacity. *ats workshop on lung volume measurements. official statement of the european respiratory society. Eur Respir J* 8(3):492–506, 1995.
- [143] West B and Matthews L. Stresses, strains, in the lung and surface pressures caused by its weight. *J Appl Physiol* 32(3), 1972.
- [144] Brudin LH, Rhodes CG, Valind SO, Wollmer P and Hughes JM. Regional lung density and blood volume in nonsmoking and smoking subjects measured by pet. *J Appl Physiol* 63(4):1324–1334, 1987.
- [145] Hopkins SR, Henderson AC, Levin DL, Yamada K, Arai T, Buxton RB and Prisk GK. Vertical gradients in regional lung density and perfusion in the supine human lung: the slinky effect. *J Appl Physiol* 103(1):240–248, 2007.
- [146] Petersson J, Rohdin M, Snchez-Crespo A, Nyren S, Jacobsson H, Larsson SA, Lindahl SGE, Linnarsson D, Neradilek B, Polissar NL, Glenny RW and Mure M. Posture primarily affects lung tissue distribution with minor effect on blood flow and ventilation. *Respir Physiol Neurobiol* 156(3):293–303, 2007.
- [147] Millar AB and Denison DM. Vertical gradients of lung density in healthy supine men. *Thorax* 44(6):485–490, 1989.
- [148] Almquist HM, Palmer J, Jonson B and Wollmer P. Pulmonary perfusion and density gradients in healthy volunteers. *J Nucl Med* 38(6):962–966, 1997.

- [149] Petersson J, Snchez-Crespo A, Larsson SA and Mure M. Physiological imaging of the lung: single-photon-emission computed tomography (SPECT). *J Appl Physiol* 102(1):468–476, 2007.
- [150] Davidson JT, Wasserman K and Lillington GA. Lung compliance of the rabbit and posturally induced changes in functional residual capacity. *Anesthesiology* 27(6):817–822, 1966.
- [151] Bachofen H, Schürch S, Urbinelli M and Weibel ER. Relations among alveolar surface tension, surface area, volume, and recoil pressure. *J Appl Physiol* 62(5):1878–87, 1987.
- [152] Weibel ER. *The Lung: Scientific Foundations*, chapter Design and Morphometry of the Pulmonary Gas Exchanger, pages 1147–1157. Raven Publishers, Philadelphia, 1997.
- [153] Knudsen L, Weibel ER, Gundersen HJG, Weinstein FV and Ochs M. Assessment of air space size characteristics by intercept (chord) measurement: an accurate and efficient stereological approach. *J Appl Physiol* 108(2):412–421, 2010.
- [154] Mercer RR, Russell ML and Crapo JD. Alveolar septal structure in different species. *J Appl Physiol* 77(3):1060–6, 1994.
- [155] Vlahovic G, Russell ML, Mercer RR and Crapo JD. Cellular and connective tissue changes in alveolar septal walls in emphysema. *Am J Respir Crit Care Med* 160(6):2086–2092, 1999.
- [156] Ruppert K, Mata JF, Dregely IM, Altes TA, Miller GW, Ketel S, Ketel J, Ruset I, Hersman FW and Mugler JPI. Hyperpolarized xenon-129 dissolved-phase signal dependence on the echo time. In: *Proceedings of the 18th Scientific Meeting of ISMRM, Stockholm, Sweden*, page p. 2552, 2010.
- [157] Ruppert K, Mata JF, Dregely IM, Altes TA, Miller GW, Ketel S, Ketel J, Ruset I, Hersman FW and Mugler JPI. Hyperpolarized xenon-129 dissolved-phase signal dependence on flip angle and tr. In: *Proceedings of the 18th Scientific Meeting of ISMRM, Stockholm, Sweden*, page p. 2554, 2010.
- [158] Periaswamy S and Farid H. Elastic registration in the presence of intensity variations. *IEEE Trans Med Imaging* 22(7):865–874, 2003.